



Integration of DInSAR and GPS for Co-seismic Modelling and Assessment of Potential Seismic Hazard

Author:

Kuang, Jianming

Publication Date:

2019

DOI:

<https://doi.org/10.26190/unsworks/21008>

License:

<https://creativecommons.org/licenses/by-nc-nd/3.0/au/>

Link to license to see what you are allowed to do with this resource.

Downloaded from <http://hdl.handle.net/1959.4/61373> in <https://unsworks.unsw.edu.au> on 2024-04-29

Integration of DInSAR and GPS for Co-seismic Modelling and Assessment of Potential Seismic Hazard

By

Jianming Kuang

A thesis submitted to The University of New South Wales in fulfilment of
the requirements for the degree of Master by Research



**Geoscience and Earth Observing Systems Group (GEOS)
School of Civil and Environmental Engineering
Faculty of Engineering
The University of New South Wales
Sydney, NSW 2052, Australia**

January 2019

Thesis/Dissertation Sheet

Surname/Family Name	: KUANG
Given Name/s	: JIANMING
Abbreviation for degree as give in the University calendar	: ME
Faculty	: Faculty of Engineering
School	: School of Civil and Environmental Engineering
Thesis Title	: Modelling and Assessment of Potential Seismic Hazard

Abstract 350 words maximum: (PLEASE TYPE)

Earthquakes often cause the collapse of buildings and other structures over a large area, which severely threaten life and properties on the ground. GPS/GNSS can provide accurate measurements of surface deformation in three directions but only with point-based spatial coverage. Interferometric Synthetic Aperture Radar (InSAR), as a space-born imaging technique, can map ground deformation along the radar line-of-sight (LOS) direction over a large area with denser observations at centimetre level accuracy. However, it is limited by the insensitivity of measurements in the north-south direction due to the near-polar orbits of SAR satellites. Therefore, the integration of GPS and Differential InSAR (DInSAR) allows us to obtain more information of the co-seismic deformation to further optimize the co-seismic earthquake source modelling. Moreover, the estimation of Coulomb stress changes based on the earthquake source model is an essential hint of potential seismic hazard. This dissertation focuses on co-seismic modelling from the combination of DInSAR and GPS measurements, and the assessment of potential seismic hazard.

Geodetic data from DInSAR and GPS measurements are used to invert source parameters and slip distribution of an earthquake based on an elastic finite rectangle source fault. In this dissertation, three most recent large earthquakes were studied. First, the best-fit source models for the 2015 Mw 7.8 Nepal Earthquake and the following Mw 7.2 aftershock were inverted based on DInSAR and GPS data. The estimation of Coulomb stress change demonstrates that the Mw 7.2 event occurred on the high stress-loaded areas of the source fault. Second, based on DInSAR and GPS data, a normal single fault with a small left-lateral component was retrieved for the 2016 Amatrice Earthquake (Central Italy). Third, for the 2017 Mw 7.3 Kermanshah Earthquake (Iran-Iraq border) the optimised source model shows a blind reverse fault with a relatively large right-lateral component. The high spatial resolution images from SuperView-1 satellite reveal that most linear surface features are gravitational deformation. Also, the Coulomb stress change on the neighbouring active faults suggests the risk of future earthquakes. This research reveals the better performance of the new generation of SAR satellites and demonstrates the seismic implication from co-seismic modelling.

Declaration relating to disposition of project thesis/dissertation

I hereby grant to the University of New South Wales or its agents the right to archive and to make available my thesis or dissertation in whole or in part in the University libraries in all forms of media, now or here after known, subject to the provisions of the Copyright Act 1968. I retain all property rights, such as patent rights. I also retain the right to use in future works (such as articles or books) all or part of this thesis or dissertation.

I also authorise University Microfilms to use the 350 word abstract of my thesis in Dissertation Abstracts International (this is applicable to doctoral theses only).

The University recognises that there may be exceptional circumstances requiring restrictions on copying or conditions on use. Requests for restriction for a period of up to 2 years must be made in writing. Requests for a longer period of restriction may be considered in exceptional circumstances and require the approval of the Dean of Graduate Research.

FOR OFFICE USE ONLY Date of completion of requirements for Award:

ORIGINALITY STATEMENT

'I hereby declare that this submission is my own work and to the best of my knowledge it contains no materials previously published or written by another person, or substantial proportions of material which have been accepted for the award of any other degree or diploma at UNSW or any other educational institution, except where due acknowledgement is made in the thesis. Any contribution made to the research by others, with whom I have worked at UNSW or elsewhere, is explicitly acknowledged in the thesis. I also declare that the intellectual content of this thesis is the product of my own work, except to the extent that assistance from others in the project's design and conception or in style, presentation and linguistic expression is acknowledged.'

INCLUSION OF PUBLICATIONS STATEMENT

UNSW is supportive of candidates publishing their research results during their candidature as detailed in the UNSW Thesis Examination Procedure.

Publications can be used in their thesis in lieu of a Chapter if:

- The student contributed greater than 50% of the content in the publication and is the “primary author”, ie. the student was responsible primarily for the planning, execution and preparation of the work for publication
- The student has approval to include the publication in their thesis in lieu of a Chapter from their supervisor and Postgraduate Coordinator.
- The publication is not subject to any obligations or contractual agreements with a third party that would constrain its inclusion in the thesis

Please indicate whether this thesis contains published material or not.

This thesis contains no publications, either published or submitted for publication (if this box is checked, you may delete all the material on page 2)

Some of the work described in this thesis has been published and it has been documented in the relevant Chapters with acknowledgement (if this box is checked, you may delete all the material on page 2)

This thesis has publications (either published or submitted for publication) incorporated into it in lieu of a chapter and the details are presented below

CANDIDATE'S DECLARATION

I declare that:

- I have complied with the Thesis Examination Procedure
- where I have used a publication in lieu of a Chapter, the listed publication(s) below meet(s) the requirements to be included in the thesis.

Name	Signature	Date (dd/mm/yy)
Jianming Kuang		09/08/2018

COPYRIGHT STATEMENT

'I hereby grant the University of New South Wales or its agents the right to archive and to make available my thesis or dissertation in whole or part in the University libraries in all forms of media, now or here after known, subject to the provisions of the Copyright Act 1968. I retain all proprietary rights, such as patent rights. I also retain the right to use in future works (such as articles or books) all or part of this thesis or dissertation.

I also authorise University Microfilms to use the 350 word abstract of my thesis in Dissertation Abstract International (this is applicable to doctoral theses only).

I have either used no substantial portions of copyright material in my thesis or I have obtained permission to use copyright material; where permission has not been granted I have applied/will apply for a partial restriction of the digital copy of my thesis or dissertation.'

AUTHENTICITY STATEMENT

'I certify that the Library deposit digital copy is a direct equivalent of the final officially approved version of my thesis. No emendation of content has occurred and if there are any minor variations in formatting, they are the result of the conversion to digital format.'

Abstract

Earthquakes often cause the collapse of buildings and other structures over a large area, which severely threaten life and properties on the ground. Aftershock sequences or further triggered seismic events on other faults could continuously bring damage or threat to the vicinity of the epicentre area. GPS/GNSS can provide accurate measurements of surface deformation in three directions but only with point-based spatial coverage. Interferometric Synthetic Aperture Radar (InSAR), as a space-born imaging technique, can map ground deformation along the radar line-of-sight (LOS) direction over a large area with denser observations at centimetre level accuracy. With the recent development of new SAR satellite systems, more SAR acquisitions with higher spatial resolution and larger ground coverage can be obtained within a shorter period. However, InSAR is also limited by the insensitivity of measurements in the north-south direction due to the near-polar orbits of SAR satellites. Therefore, the integration of GPS and Differential Interferometric Synthetic Aperture Radar (DInSAR) allows us to obtain more information of the co-seismic deformation caused by earthquakes and to further optimize the co-seismic earthquake source modelling. In addition, large earthquakes always perturb the stress conditions of the surrounding fault systems, and the estimation of stress changes based on the source model is an essential hint of potential seismic hazard. This dissertation focuses on co-seismic modelling from the combination of DInSAR and GPS measurements, and the assessment of potential seismic hazard.

Geodetic data from DInSAR and GPS measurements are used to invert source parameters and slip distribution of an earthquake based on the finite rectangle source fault in a homogeneous half-space. Furthermore, Coulomb stress change on the source fault and neighbouring active faults are estimated to evaluate the risk of seismic hazards. In this dissertation, three most recent large earthquakes were studied. First, the best-fit source models for the 2015 M_w 7.8 Nepal Earthquake and the following M_w 7.2 aftershock were inverted based on DInSAR and GPS data, revealing two NW-SE striking faults with low dips. The estimation of Coulomb stress change demonstrates that the M_w 7.2 event occurred on the high stress-loaded areas of the source fault for the main shock. Second, a normal single fault with a small left-lateral component was determined by co-seismic DInSAR and GPS measurements for the 2016 M_w 6.2 Amatrice (Central Italy) Earthquake. The stress changes induced by this event on the fault planes of the following

two major shocks reveal that the triggering relationship between the Amatrice Earthquake and the following two events. Third, for the 2017 Mw 7.3 Kermanshah (Iran-Iraq border) Earthquake the optimised source model shows a blind reverse fault with a relatively large right-lateral component. The high spatial resolution images from SuperView-1 satellite reveal that most linear surface features mapped by DInSAR measurements are gravitational deformation. Also, the Coulomb stress change on the neighbouring active faults agrees with the occurrence of major aftershocks and suggests the risk of future earthquakes. This research reveals the better performance of the new generation of SAR satellites and demonstrates the seismic implication from co-seismic modelling.

Acknowledgements

This research was conducted in the Geoscience and Earth Observing Systems Group (GEOS), School of Civil and Environmental Engineering at the University of the New South Wales (UNSW), Sydney, New South Wales, Australia from September 2016 to August 2018. Many people helped and supported me in various ways during the journey of my research. I would like to thank everybody who supported me.

First and foremost, I would like to thank supervisor, Associate Professor Linlin Ge for his supervising and supporting my Master research. I learned and benefited a lot from his advice. I would also express my sincere thanks to my co-supervisor Professor Graciela Isabel Metternicht for her careful reading and valuable suggestions for my publications.

I would like to express my gratitude to our current and former GEOS group members, including Liam Liyuan Li, Tim Youtian Liu and Dr Xiaojing Li for their help and support. Particularly, I would like to thank Professor Alex Hay-Man Ng, a mentor and good friend of mine, for sharing his great understanding in the field of radar interferometry. He was really kind and patient to discuss the research with me and always gave help and support when I needed advice. My undergraduate supervisor Professor Hua Wang at Guangdong University of Technology guided me to the field of radar interferometry, and I am really grateful that he gave me this opportunity to further study as a Master student. I would also acknowledge the support of Dr Yincai Zhou, Dr Bruce Harvey, Patricia McLaughlin and Patrick Vuong. With this opportunity, I would like to thank the China Scholarship Council (CSC) for providing the two-year financial support for my Master study.

The Earth Remote Sensing Data Analysis Centre is acknowledged for providing the ALOS-2 PALSAR data. JAXA retain the ownership of the ALOS-2 PALSAR original data. The European Space Agency is acknowledged for providing data from the Sentinel-1A/B missions.

Finally, I would like to express my sincerest gratitude to my parents and family for their positive encouragement, emotional support and selfless love. Without their help and support, this thesis would not have been possible. Thanks to all the people who love me and whom I love.

List of Publications

Several journal and conference papers have been accepted for publishing, published or submitted during the journey of research study. The publication list is shown as follows:

Journal Paper:

Kuang, J., Ge, L., Metternicht, G. and Ng, A.H.-M., Wang, H., Zare, M., Kamranzad, F., 2018. Coseismic deformation and source model of the 12 November 2017 M_w 7.3 Kermanshah Earthquake (Iran-Iraq border) investigated through DInSAR measurements. *International Journal of Remote Sensing*. (Accepted on 17 July 2018)

Conference Papers:

Kuang, J., Ge, L., Metternicht, G. and Ng, A.H.-M., 2018, July. SOURCE MODEL OF THE 12 NOVEMBER 2017 M_w 7.3 KERMANSHAH EARTHQUAKE (IRAN-IRAQ BORDER) INFERRED FROM ALOS-2 SCANSAR AND SENTINEL-1 DATA. In *Geoscience and Remote Sensing Symposium (IGARSS), 2018 IEEE International* (in press). IEEE.

Kuang, J., Ge, L., Metternicht, G. and Ng, A.H.-M. (2017). FINITE FAULT MODEL OF THE 24 AUGUST 2016 AMATRICE EARTHQUAKE (CENTRAL ITALY) INFERRED FROM DINSAR AND GPS CO-SEISMIC DEFORMATION. In *2015 Australian Space Research Conference (ASRC 2017)*, 11-24.

Table of Contents

Abstract	i
Acknowledgements	iii
List of Publications	iv
Table of Contents	v
List of Abbreviations	ix
List of Figures	xi
List of Tables	xviii
Chapter 1 Introduction	1
1.1 Background	1
1.2 Research Aim and Objective	2
1.3 State of the Art in Seismic Hazard Monitoring.....	3
1.3.1 Inter-seismic monitoring	3
1.3.2 Co-seismic mapping and secondary co-seismic hazards	4
1.3.3 Post-seismic deformation	5
1.3.4 Geodetic Technique: GPS and InSAR	6
1.3.5 Coulomb Stress Change	10
1.4 Contribution.....	11
1.5 Thesis Outline.....	11
Chapter 2 DInSAR Technique for Mapping Co-seismic Displacement Field	13
2.1 Introduction	13
2.1.1 Synthetic Aperture Radar System	14
2.1.2 The Principle of DInSAR Technique	17
2.2 The procedures of two-pass DInSAR processing.....	20
2.2.1 Co-registration and Interferogram Generation.....	21
2.2.2 Filtering and Coherence Generation	23

2.2.3	Phase Unwrapping	24
2.2.4	Refinement and Re-flattening	25
2.2.5	Phase to Displacement and Geocoding	26
2.3	The 2.5D Displacement Field Analysis.....	27
2.4	Limitations of DInSAR Technique	29
2.5	Concluding Remarks	31
Chapter 3	Geodetic Modelling from Co-seismic Deformation.....	32
3.1	Geodetic Modelling Strategy.....	32
3.1.1	Source Fault Geometry Definition	32
3.1.2	Forward Modelling	34
3.1.3	InSAR Data Downsampling.....	35
3.1.4	Non-Linear Inversion	37
3.1.5	Linear Inversion	38
3.1.6	Weight Strategy.....	40
3.1.7	Modelled 3D Displacement Field	42
3.2	Coulomb Stress Change	43
3.3	Concluding Remarks	45
Chapter 4	Co-seismic Deformation and Source Model of the 25 April 2015 Mw 7.8 Nepal Earthquake and the 12 May 2015 Mw 7.2 aftershock.....	46
4.1	Introduction	46
4.2	Geodetic Data	48
4.2.1	SAR Data	48
4.2.2	DInSAR Measurements	49
4.2.3	GPS Data.....	53
4.3	Modelling	54
4.4	Result.....	56
4.4.1	Modelling Result for the 25 April 2015 Mw 7.8 main shock.....	56

4.4.2	Modelling Result for the 12 May 2015 Mw 7.2 aftershock.....	60
4.5	Discussion	64
4.5.1	Coulomb Stress Change Analysis for the Mw 7.8 main shock	64
4.5.2	Triggering relationship between main shock and aftershock.....	66
4.6	Conclusion.....	68
Chapter 5 Finite Fault Model of the 24 August 2016 Amatrice Earthquake		
(Central Italy) Inferred from DInSAR and GPS Co-seismic Deformation		
69		
5.1	Introduction	69
5.2	Geodetic Data	74
5.2.1	SAR Data	74
5.2.2	DInSAR measurements.....	75
5.2.3	GPS Data.....	78
5.3	Modelling	79
5.4	Result.....	81
5.5	Discussion	84
5.5.1	Coulomb Stress Change Analysis	84
5.5.2	Triggering Relationship with the October 26 and 30 Event	86
5.6	Conclusion.....	87
Chapter 6 Co-seismic deformation and source model of the 12 November 2017		
Mw 7.3 Kermanshah Earthquake (Iran-Iraq border) investigated through DInSAR		
measurements		
89		
6.1	Introduction	89
6.1.1	The 12 November 2017 Kermanshah Earthquake	89
6.1.2	Tectonic background.....	90
6.2	Data availability and DInSAR measurements.....	93
6.2.1	Data availability	93
6.2.2	DInSAR Measurements	94
6.3	Modelling	97

6.4	Result.....	99
6.4.1	Separate inversion results using ALOS-2 and Sentinel-1A/B ascending and descending data individually.....	99
6.4.2	Joint inversion results using both ALOS-2 and Sentinel-1A/B data	102
6.5	Discussion	105
6.5.1	Linear surface ruptures of the 2017 Kermanshah Earthquake	105
6.5.2	Triggering relationships with neighbouring active faults	109
6.6	Conclusion.....	113
Chapter 7	Conclusions and Future Work.....	115
7.1	Conclusions	116
7.2	Recommendations for Future Work	117
Reference.....		119

List of Abbreviations

ALOS	Advanced Land Observing Satellite
ASAR	Advanced Synthetic Aperture Radar
ASI	Italian Space Agency
BHRC	Building & Housing Research Centre
CGPS	Continuous Global Positioning System
COSMO-SkyMed	COntellation of small Satellites for the Mediterranean basin Observation, aka SkyMed
CSA	Canadian Space Agency
DEM	Digital Elevation Model
DInSAR	Differential Interferometric Synthetic Aperture Radar
DLR	Deutsches Zentrum für Luft- und Raumfahrt (German Aerospace Centre)
ESA	European Space Agency
ENVISAT	Environmental SATellite
FBD	Fine beam dual-polarisation
FBS	Fine beam single-polarisation
GCMT	Global Centroid Moment Tensor
GPS	Global Positioning System
IIEES	International Institute of Earthquake Engineering and Seismology
INGV	Institute of Geophysics and Volcanology
InSAR	Interferometric Synthetic Aperture Radar
IRSC	Iranian Seismological Centre
ISMN	Iran Strong Motion Network
JAXA	Japan Aerospace Exploration Agency

JERS	Japanese Earth Resources Satellite
Lat	Latitude
Lon	Longitude
LOS	line-of-sight
MCF	Maximum Cost Flow
NASA	National Aeronautics and Space Administration
NERC	National Earthquake Information Centre
NSC	National Seismological Centre
PALSAR	Phased Array type L-band Synthetic Aperture Radar
RADAR	RADio Detection And Ranging
RADARSAT	Radar Satellite
RMSE	Root Mean Square Error
RSC	Regional Seismological Centre
SAR	Synthetic Aperture Radar
SLC	Single Look Complex
SNR	Signal-to-Noise Ratio
SRTM	Shuttle Radar Topography Mission
TerraSAR-X	German Radar Earth Observation Satellite
USGS	United States Geological Survey
2.5D	2.5-Dimensional
3D	Three-Dimensional

List of Figures

Figure 1.1 Seismic Cycle including four seismic stages, inter-seismic stage (red line), pre-seismic stage (yellow line), co-seismic stage (green line) and post-seismic stage (blue line) 3

Figure 2.1 SAR viewing geometry 17

Figure 2.2 Two-pass DInSAR imaging geometry..... 18

Figure 2.3 Two-pass DInSAR processing workflow 20

Figure 2.4 Multi-look interferogram from ALOS-2 StripMap data overlaid on the Master intensity image with original pixel size 22

Figure 2.5 (a) Differential interferogram, (b) filtered interferogram and (c) filtered interferogram with the linear trend removed 23

Figure 2.6 The coherence map corresponding to the interferogram in Figure 2.5..... 24

Figure 2.7 Decomposition of the LOS displacement vector from DInSAR measurement. SH represents the satellite heading direction, SL represents the satellite looking direction projected on the ground, α is the azimuth of satellite heading vector (positive clockwise from the North), θ is the incidence angle at the reflection point, D_{LOS} is the LOS displacement vector, D_U , D_E and D_N are vertical, eastward and northward displacement, respectively. 28

Figure 3.1 The geometry of source fault with key parameters. (a) Source fault with the hanging wall and foot wall. (b) The rectangle fault plane with source parameters in the Cartesian coordinate system. The red star indicates the centre of the fault plane. 33

Figure 3.2 Forward modelling of surface displacement based on the Okada model. (a) a finite rectangle source fault overlapping with the modelled vertical displacement in 3D view. (b) The modelled vertical displacement in 3D view. 35

Figure 3.3 Comparison between different downsampling strategies. (a) Quadtree downsampling result, and (b) Uniform downsampling result with various density of grid for DInSAR displacement map. 36

Figure 3.4 (a) co-seismic wrapped interferogram from Sentinel-1A/B image pairs, the dash rectangle represents the selected area for the sampling of semi-varigram; (b) results of experimental semi-varigram (red squares) and the fitting exponential function (blue line) with nugget..... 42

Figure 3.5 Modelled 3D displacement components in west-east, north-south and vertical directions, respectively.....43

Figure 4.1 Geographical setting of the 25 April 2015 M_w 7.8 Nepal Earthquake and the 12 May 2015 M_w 7.2 Aftershock superimposed on the elevation map derived from 3-arc SRTM data (Farr et al., 2007). Red and orange stars show the epicentres of main shock and M_w 7.2 aftershock, respectively from USGS. Green dots are relocated aftershocks ($4.0 < M_w < 7.0$) within the first 45 days (Adhikari et al., 2015). White stars represent the large historical earthquakes ($M_w \geq 7.0$). Blue and yellow boxes show the spatial coverages of ALOS-2 and Sentinel-1A images used in this study. Black triangles are GPS stations. Red lines are active faults in this region (Styron et al., 2010).47

Figure 4.2 Co-seismic displacement maps of the 25 April M_w 7.8 Nepal Earthquake from (a)-(b) ALOS-2 and Sentinel-1A descending data and the 12 May M_w 7.2 aftershock from (c)-(d) ALOS-2 descending and Sentinel-1A ascending data. Red lines are active faults around this region. Red star and black star are the epicentres of main shock (M_w 7.8) and aftershock (M_w 7.2) from the USGS, respectively.51

Figure 4.3 Downsampled points from four co-seismic displacement maps used in this study. (a)-(b) ALOS-2 and Sentinel-1A descending displacement maps for main shock (M_w 7.8); (c)-(d) ALOS-2 descending and Sentinel-1A ascending displacement maps for aftershock (M_w 7.2). Red lines are active faults around this region. Red star in (a)-(b) is main shock and white star in (c)-(d) is aftershock. Red and blue colours represent decrease and increase in the LOS range, respectively.52

Figure 4.4 Co-seismic GPS measurements of the 25 April Nepal Earthquake. Black triangles represent the locations of GPS stations with horizontal (blue arrows) and vertical (red arrows) measurements. Red star is the epicentre of main shock. Red lines are active faults.....53

Figure 4.5 Trade-off curve between the misfit of measurement and the solution roughness for the slip distribution of (a) the main shock and (b) the major aftershock. Each dot on the curves represents one individual experiment with specific value of damping factor. The red dot in (a) and green dot in (b) are the optimal damping factor with 0.3 and 0.35, respectively.55

Figure 4.6 Slip distribution and aftershock distribution of the 25 April 2015 M_w 7.8 main shock, 2D view of surface projection (a) and the corresponding 3D view (b). The white star in (a) is main shock, corresponding to the black sphere in (b). Blue square represents the city of Kathmandu. Black dashed line in (a) is fault trace intersected with the surface.

Black dots in (a) are aftershocks, corresponding to the blue dots in (b). Red lines are active faults..... 58

Figure 4.7 DInSAR misfit analysis for the 25 April 2015 M_w 7.8 main shock. Observed, modelled and residual data are ALOS-2 ScanSAR descending (a-c) and Sentinel-1A descending (d-f), respectively. Red star is main shock (M_w 7.8) and black star is aftershock (M_w 7.2). Red lines are active faults. 59

Figure 4.8 GPS (a) horizontal observed data (blue arrow) and modelled data (violet arrow), as well as (b) vertical observed data (red arrow) and modelled data (yellow arrow). The red star is main shock and black triangles are locations of GPS stations. Red lines are active faults. 60

Figure 4.9 Slip distribution of 12 May 2015 M_w 7.2 aftershock, 2D view of surface projection of fault plane (a) and the corresponding 3D view (b). White star in (a) is the epicentre of aftershock (M_w 7.2), corresponding to the black sphere in (b). Black dashed line in (a) is fault trace intersected with the surface. Black dots in (a) are aftershocks, corresponding to the blue dots in (b). Red lines are active faults. 61

Figure 4.10 DInSAR misfit analysis for the 12 May 2015 M_w 7.2 aftershock. Observed, modelled and residual data are ALOS-2 ScanSAR descending (a-c) and Sentinel-1A ascending (d-f), respectively. Red star is epicentre of main shock (M_w 7.8) and black star is the epicentre of aftershock (M_w 7.2) from USGS. Red lines are active faults. 63

Figure 4.11 Coulomb stress change on the source fault of the 25 April 2015 M_w 7.8 main shock. (a) 2D view of stress change on the fault plane with aftershock distribution (violet dots), main shock (red star) and white star (M_w 7.2 aftershock). Red lines are active faults. (b) 3D view corresponding to (a). Green circles show the locations of aftershocks ($6.0 \leq M_w < 7.0$). 65

Figure 4.12 Coulomb stress change on the source fault of the M_w 7.8 main shock and the stress transfer on the M_w 7.2 aftershock. (a) 2D view, red star and white star represent the epicentres of main shock and major aftershock (M_w 7.2), respectively. Blue stars are historical earthquakes. Violet square represents the city of Kathmandu. Black dots are aftershock distribution. Red lines are active faults. (b) 3D view corresponding to (a)... 67

Figure 5.1 Geographical setting with main shock (white star), aftershocks (yellow circles), active faults (red lines) from INGV, GPS stations (green triangles) and spatial coverage of SAR images (blue rectangles for ALOS-2 images and yellow rectangles for Sentinel-1A/B images). The blue star represents the significant M_w 5.3 aftershock. The red stars represent the October 26 and October 30 main shocks. The yellow scaled circles present

the locations of aftershocks ($M_w > 2.0$) from 24/08/2016 to 15/09/2016 collected from Institute of Geophysics and Volcanology (INGV) National Earthquake Centre [<http://cnt.rm.ingv.it/tdmt>]. 71

Figure 5.2 ALOS-2 and Sentinel-1A/B co-seismic deformation maps. (a) ALOS-2 ascending (Track 197); (b) ALOS-2 descending (Track 92); (c) Sentinel-1A/B ascending (Track 117); (d) Sentinel-1A/B descending (Track 22). Black squares represent the major cities. The white star is main shock and red lines are active faults..... 76

Figure 5.3 Co-seismic displacement in (a) east-west and (b) vertical directions retrieved from Sentinel-1A/B ascending and descending LOS displacement maps. The white star shows the epicentre from the USGS. (c) Profile plot along A-A' section across the areas of maximum deformation in the vertical displacement (b). 77

Figure 5.4 Downsampled measurement points from four co-seismic deformation maps used in this study. (a) ALOS-2 ascending (Track 197); (b) ALOS-2 descending (Track 92); (c) Sentinel-1A/B ascending (Track 117); (d) Sentinel-1A/B descending (Track 22). White star is main shock. 78

Figure 5.5 GPS horizontal (blue arrows) and vertical (red arrows) co-seismic measurements. Black squares denote the location of each GPS station. The station named GUB2 is highlighted with violet squares and label. The white star represents main shock. 79

Figure 5.6 Trade-off curve between the misfit of measurement and the solution roughness for the slip distribution. Each dot on the curves represents one individual experiment with specific value of damping factor. The red dot is the optimal damping factor with 0.18.80

Figure 5.7 Slip distribution for the Amatrice Earthquake. (a) 2D map view of slip distribution with main shock (white star), aftershocks (blue dots), active faults (red lines) and estimated fault trace (black line). (b) 3D view of slip distribution with aftershock distribution and main shock (black sphere). 82

Figure 5.8 DInSAR fitting deformation for the 2016 24 August, Amatrice Earthquake. Observed, modelled, and residual data from ALOS-2 ascending (a-c), ALOS-2 descending (d-f), Sentinel-1A/B ascending (g-i), Sentinel-1A/B descending (j-l). The white star is main shock and black lines in (a)-(l) are active faults from INGV. 83

Figure 5.9 GPS horizontal (a) observed (blue) and model (green) data, as well as GPS vertical (b) observed (red) and model (yellow) data. The white star is main shock. 84

Figure 5.10 Stress change on (a) the source plane and (b) the corresponding 3D view. The white star is main shock, black dots are aftershocks and red lines are active faults from INGV. The red stars are October 26 M_w 5.9 and October 30 M_w 6.6 main shocks..... 85

Figure 5.11 Coulomb stress change on (a) the fault plane of the 26 October 2016 event (Xu et al., 2017) induced by the Amatrice Earthquake, (b) the fault plane of the 30 October 2016 event jointly induced by the 26 October 2016 and the Amatrice Earthquake. The red lines are active faults from INGV. The white, green and red stars represent the epicenter of the Amatrice Earthquake, the 26 October event and the 30 October event, respectively. 87

Figure 6.1 Tectonic setting of the 2017 M_w 7.3 Kermanshah Earthquake. Red star is the main shock and violet circle is the foreshock. Yellow circles are aftershocks with $2.5 < M_w < 5.0$ collected from the Iranian Seismological Centre (IRSC). Green circles are major events with $M_w > 5.0$ after the main shock. Red lines are active faults from the International Institute of Earthquake Engineering and Seismology (IIEES) (Hessami et al., 2003). Green and blue boxes represent the spatial coverage of ALOS-2 and Sentinel-1A/B SAR image pairs, respectively. Black stars represent the major historical earthquakes ($M_w > 6.0$) before 1976 from the USGS. Red focal mechanism plots denote the historical earthquakes ($M_w > 6.0$) between 1976 and 2014 from the GCMT..... 92

Figure 6.2 DInSAR measurements (LOS) of the 2017 M_w 7.3 Kermanshah Earthquake. (a)-(b) ALOS-2 ascending and descending displacement maps; (c)-(e) Sentinel-1A/B ascending and descending displacement maps. Red and blue colours represent decrease and increase in the LOS range, respectively. The white star is main shock, and black lines are active faults in western Iran. 95

Figure 6.3 Down-sampled points from five co-seismic displacement maps used in this study. (a)-(b) ALOS-2 ascending (Track 180) and descending (Track 71) displacement maps; (c)-(e) Sentinel-1A/B ascending (Track 72) and descending (Track 79 and 6) displacement maps. Red and blue colours represent decrease and increase in the LOS range, respectively..... 96

Figure 6.4 Trade-off curve between the misfit of measurement and the solution roughness for the slip distribution. Each black dot on the curve represents one individual experiment with specific value of damping factor. The red dot is the optimal damping factor with 0.36 we chose in this study. 98

Figure 6.5 Slip distribution inverted by using (a) ALOS-2 ascending DInSAR measurements (Track 180), (b) ALOS-2 descending DInSAR measurements (Track 71),

(c) ALOS-2 ascending and descending DInSAR measurements (Track 180 and 71), (d) Sentinel-1A/B ascending DInSAR measurements (Track 72), (e) Sentinel-1A/B descending DInSAR measurements (Track 79 and 6), (f) Sentinel-1A/B ascending and descending DInSAR measurements (Track 72, 79 and 6). The black star shows the epicentre from USGS and the black lines are corresponding fault traces intersected with the surface. 100

Figure 6.6 Fault slip distribution and aftershock distribution of the 2017 M_w 7.3 Kermanshah Earthquake, 2D view of surface projection (a) and 3D view (b). The black star in (a) is main shock, corresponding to the black sphere in (b). Black line is fault trace intersected with the surface. Blue dots in (a-b) are aftershocks, and red lines in (a) are active faults. 104

Figure 6.7 Misfit analysis for the 2017 M_w 7.3 Kermanshah Earthquake. Observed, modelled and residual data from ALOS-2 ScanSAR ascending (a-c) (Track 180) and descending (d-f) (Track 71), Sentinel-1A/B ascending (g-i) (Track 72), descending (j-l) (Track 79) and descending of 12days (m-o) (Track 6). White star is main shock, and black lines are active faults in western Iran. 105

Figure 6.8 Linear surface ruptures (black lines) identified in (a) ALOS-2 ascending interferogram (Track 180), (b) ALOS-2 descending interferogram (Track 71), (c) Sentinel-1A/B ascending interferogram (Track 72) and (d) Sentinel-1A/B descending interferogram (Track 6). The white star shows the epicentre from USGS and the black triangles are major cities nearby. The white boxes are the footprints of SuperView-1 images. The violet rectangle is the coverage of Figure 9(g-i). 107

Figure 6.9 Triggered landslides and surface ruptures near the city of Sarpol Zahab (a-c), Darbandikhan (d-f) and Sar Cheqa (g-i). See Figure 6.8 for the location of (g-i). The black lines are mapped linear surface ruptures from DInSAR measurements, and the black triangles are major cities or villages. The red arrows show the surface cracks and the red polygons indicate the triggered landslides. 108

Figure 6.10 (a) Coulomb stress change on the source fault plane of the Kermanshah Earthquake and the neighbouring active faults investigated in this study. White stars are major historical earthquakes in this region. The small dots with different colours are aftershocks occurred within 150 days after main shock, same as the black dots in (b-d). Enlarged maps for (b) source plane; (c) MFF-1, MFF-2, HZF; (d) MFF-3, MFF-4, MFF-5 and ZFF. (e) The 3D view for source fault and active fault planes. The red star in (a-d)

shows the main shock, corresponding to the black sphere in (e). Green circles in (a-e) show the location of major aftershocks ($\geq M_w 5.0$). Red lines are active faults..... 111

List of Tables

Table 1.1 Previous and current SAR satellite missions with their basic information.....	8
Table 2.1 Outline of radar satellite missions with their key parameters.....	15
Table 4.1 Interferometric pairs used for the 2015 Nepal Earthquake Sequence.....	49
Table 4.2 Fault parameters of the 25 April 2015 Mw 7.8 Nepal Earthquake from seismology and geodetic inversion	57
Table 4.3 Fault parameters of the 12 May 2015 aftershock from seismology and geodetic inversion.....	62
Table 5.1 Source parameters of the 24 August 2016 Amatrice Earthquake	72
Table 5.2 The processed interferometric pairs for the 2016 Amatrice Earthquake	74
Table 6.1 SAR image pairs used for the 2017 Kermanshah Earthquake	93
Table 6.2 Source parameters of uniform slip model inverted from different data.....	101
Table 6.3 Fault parameters of Kermanshah Earthquake from seismology and geodetic inversion.....	103

Chapter 1 Introduction

1.1 Background

When the long-term accumulated stress exceeds the strength of underground rocks and breaks them, a large amount of energy is suddenly released, leading to the generation of seismic waves which would shake the ground in a short time. That is called earthquake. Earthquake has been the most deadly natural disaster in the last 30 years in the world, resulting in over 850,000 deaths and 18 million injuries (44.3% of total death roll and 27.7% of total injuries due to natural disasters from 1987 to 2017) (EM-DAT (2018)). The total economic damage due to earthquakes in this period is over \$700 billion. Except for aftershock sequences following the main shock, a series of secondary disasters (e.g. tsunamis, landslides and avalanche lakes) could be triggered by earthquakes. Even a small earthquake, if occurring at a shallow depth and near the populated areas, could pose serious threat to properties, human lives and our societies. Therefore, investigating and understanding the nature of earthquakes is not only a research field, but also of critical importance to the safety and development of human beings and society.

The pattern of earthquake mechanism is the key to understanding the nature of earthquake. In other words, the earthquake mechanism is characterised with source parameters (e.g. fault orientation, size and depth) and slip distribution on the faults, resulting in different patterns of co-seismic surface deformation. Thus, these source parameters and slip distribution on the faults are valuable information for evaluation of earthquakes and the possible seismic activities in the future. A theoretical geophysical earthquake model can be used to describe these source parameters, which is also called earthquake source model. Using the earthquake source model, the modelled surface deformation related to different source parameters can be generated. Conversely, if the real co-seismic deformation is obtained, it is possible to invert the corresponding source parameters for the earthquake source model which can best reproduce the real surface deformation. A finite rectangle fault model in an elastic, homogeneous half-space (Okada, 1985) is the most used earthquake source model in geodetic modelling. This finite rectangle model provides a unique opportunity to extract important information of earthquake source from the observed co-seismic deformation. Therefore, measuring and mapping the co-seismic deformations of earthquakes is essential for the geodetic modelling. Global Position

System (GPS) can provide accurate measurements of surface displacement in three directions but only with point-based spatial coverage. Interferometric Synthetic Aperture Radar (InSAR), as a space-borne technique, has demonstrated its effectiveness for monitoring surface deformation. InSAR can map surface movement along the radar line-of-sight (LOS) direction with large spatial coverage and dense observations at centimetre-level accuracy. However, the main limitation is that InSAR is not sensitive to the measurement along the north-south direction due to the near-polar orbits of SAR satellites. Moreover, the stress change estimation based on the result of earthquake source modelling, the neighbouring active faults and the characteristic time of aftershocks generally is not exploited to deeper analysis for seismic assessment. In this work, these issues are further investigated.

1.2 Research Aim and Objective

This research has three main objectives: First, to assess the integration of GPS and DInSAR for mapping co-seismic deformation; Second, to determine the source models and slip distributions of major earthquakes from geodetic modelling with InSAR and GPS co-seismic measurements; Third, to further investigate the triggering relationship between the source models of the main shock and the neighbouring active faults, and assess the risk of potential seismic hazards based on the Coulomb stress change analysis.

The approach for mapping co-seismic deformations caused by earthquakes relies on SAR images from the new generation SAR satellites, ALOS-2 and Sentinel-1A/B. The mapping performance of ALOS-2 ScanSAR and Sentinel-1A/B TOPS SAR data is investigated in the case study of large earthquakes.

In order to explore how well the source models of earthquakes can be inverted from geodetic data, and to understand how the source faults interact with the neighbouring active faults, three most recent major earthquakes are explored in this dissertation using geodetic data to determine the corresponding optimized source models and slip distributions. Three most recent earthquakes are: the 25 April 2015 M_w 7.8 Nepal Earthquake and its M_w 7.2 aftershock, the 24 August 2016 M_w 6.2 Amatrice (Central Italy) Earthquake and the 12 November 2017 M_w 7.3 Kermanshah (Iran-Iraq border) Earthquake.

The next section summarises the state of the art in remote sensing of seismic hazard monitoring, including current and past satellite sensors applied to this end.

1.3 State of the Art in Seismic Hazard Monitoring

The seismic cycle refers to repetition periods of earthquakes. Generally, seismic cycle can be divided into four periods, consisting of inter-seismic, pre-seismic, co-seismic and post-seismic stages (Shearer, 2009). The overall strain change of seismic cycle is shown in Figure 1.1. It is also noted that earthquakes are not regular repeating events but with relative distinct stages.

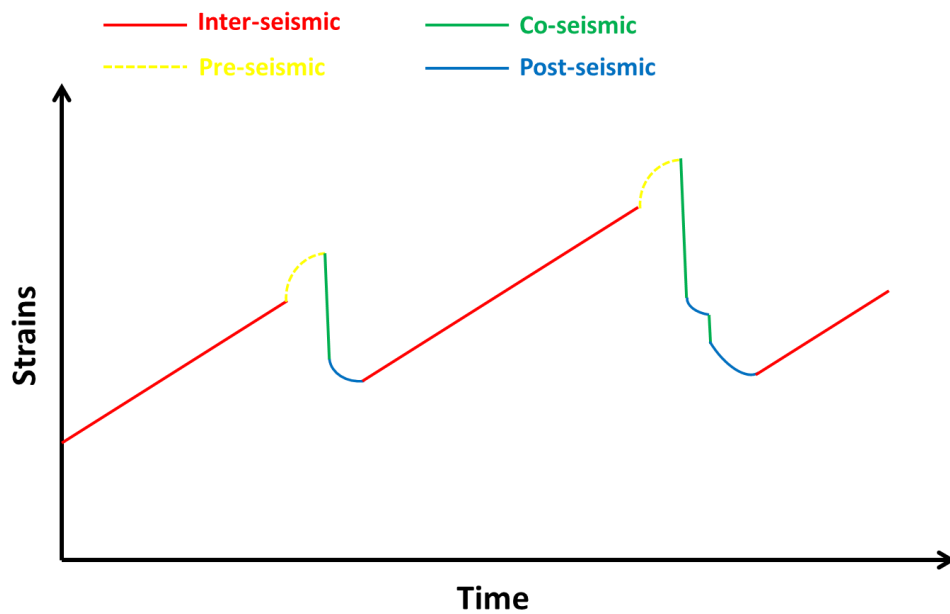


Figure 1.1 Seismic Cycle including four seismic stages, inter-seismic stage (red line), pre-seismic stage (yellow line), co-seismic stage (green line) and post-seismic stage (blue line)

1.3.1 Inter-seismic monitoring

As for the inter-seismic stage, it is clearly shown that the elastic strains accumulate steadily (usually a constant rate) over a long period of time. At this stage, the faults are creeping between two plates and partially locked in several segments at different depths, resulting long-term aseismic slip accumulation. Observations from GPS and InSAR data evidenced the corresponding surface creep occurring on the major fault systems all around the world such as San Andreas Fault (SAF) in North American (Fialko, 2006, Tong et al., 2013, Jolivet et al., 2015), North Anatolian Fault in Turkey (Kaneko et al., 2013, Bilham et al., 2016), Longitudinal Valley Fault in Taiwan (Chen et al., 2008, Thomas et al., 2014), Haiyuan Fault in China (Cavalié et al., 2008, Jolivet et al., 2012). Some large earthquakes can be produced by the long-term fault creep (Harris, 2017),

which could influence the stress change over this area. Pre-seismic stage generally refers to the foreshocks occurred before the main shock (larger earthquake). Several large previous earthquakes were preceded by a series of foreshocks, including 2014 Iquique (Chile) M_w 8.1 Earthquake (Ruiz et al., 2014) and 2016 Kumamoto Earthquake (Asano and Iwata, 2016).

1.3.2 Co-seismic mapping and secondary co-seismic hazards

In the co-seismic stage, the accumulated strains decrease suddenly after a short period of pre-seismic stage. When the long-term accumulated strains exceed the strength of rocks or the friction of faults, the earthquakes occur along with sudden fault failure, resulting in the fault slip on the fault plane. Even though this process is extremely fast, some early warning systems which depend on detecting the first round of seismic wave (P-waves) could provide prior warning but with only a limited advance time. A recent example is that the Mexican Seismic Alert System (SASMEX) gave about two minutes of warning for the 7 September 2017 M_w 8.2 event, which earned the precious time for the local residents to react (Suárez et al., 2018). Earthquakes generally occur on the rupture zone with length and width both ranging from several kilometres to hundreds of kilometres. For example, 2009 M_w 6.3 L'Aquila Earthquake ruptured on a 20km×14km fault with some of slip up to the surface (Atzori et al., 2009), 2008 M_w 7.9 Wenchuan Earthquake with a 300km×30km underground rupture (Tong et al., 2010) and 2015 M_w 7.8 Nepal Earthquake for a 180km×100km zone (Feng et al., 2017). The large rupture zone with fault slip can generate the surface deformation in large spatial extent which cannot be fully observed by conventional methods. InSAR technique, especially two-pass Differential Interferometric SAR (DInSAR), can efficiently capture the co-seismic deformation with large spatial coverage (up to hundreds of kilometre) by using two SAR images, one before (pre-seismic) and another after (post-seismic) an earthquake. In addition, secondary co-seismic hazards such as landslides, surface cracks and rockfalls typically could be triggered by the shaking of main shock. From the co-seismic DInSAR wrapped or unwrapped interferograms, the scales and locations of these gravitational deformations just can be approximated owing to the insufficient spatial resolution. Some of localized deformations or linear surface features due to landslides or surface cracks at a large scale may be misinterpreted as surface ruptures due to co-seismic fault slip. To explore these secondary co-seismic hazards, the combination of DInSAR and high spatial resolution optical satellite images can be adopted. So far, several landslides caused by

previous earthquakes were studied with radar and optical data. The distribution of landslides induced by the 2008 Wenchuan Earthquake was mapped by a series of high spatial resolution optical images (Gorum et al., 2011). Radar (ERS, ENVISAT and RADARSAT) and optical (ALOS and GeoEye-1) images are used to reveal the landslides triggered by 2009 L'Aquila Earthquake (Casagli et al., 2016). The combination and comparison between DInSAR results and high spatial resolution optical images provide a chance to further explore these secondary co-seismic hazards. Most importantly, it helps us analyse and interpret these gravitational deformations or linear surface features within the epicentre area. In this thesis, high spatial resolution optical images (0.5m) from the SuperView-1 satellite were used to explore the linear features of the M_w 7.3 Kermanshah Earthquake (Iran-Iraq border) in combination with the DInSAR results.

1.3.3 Post-seismic deformation

A series of aftershocks generally occur after the main shock within several weeks, months or years. Even though the magnitude of aftershocks is smaller than that of the main shock, a number of aftershocks occurred around the epicentre area (typically within a distance equal to 1-2 times the length of fault rupture) could threat the area for a long time. For example, over 80,000 aftershocks were recorded within 3 years following the 2009 M_w 6.3 L'Aquila Earthquake (Albano et al., 2015). Aftershocks could collapse the buildings or other structures which already suffered a large damage from the main shock. Also, some of the landslides or rockfalls could be reactivated by the aftershock sequence. Such a long-period aftershock sequence contributes to the accumulated post-seismic deformation. Many post-seismic surface deformations were observed by geodetic measurements for the previous large earthquakes, such as the 1992 M_w Landers Earthquake (Massonnet et al., 1994, Shen et al., 1994), the 1997 M_w 7.6 Manyi (Tibet) Earthquake (Ryder et al., 2007), the 2004 Parkfield Earthquake (Barbot et al., 2009) and 2009 L'Aquila Earthquake (Albano et al., 2015). Since the post-seismic SAR image could probably be acquired within several days or even weeks after the main shock, the co-seismic deformation mapped by InSAR technique actually contains a fraction of post-seismic deformation, which could involve some of afterslip into the source model. Most importantly, aftershock distribution can be used to constrain and verify the fault geometry of earthquake source model. Also, the stress changes induced by the main shock are highly correlated with aftershock distribution.

1.3.4 Geodetic Technique: GPS and InSAR

The vibrations generated by earthquakes were recorded by using instruments called seismometers since the 1880s, which allow seismologists to determine the magnitudes and locations of earthquakes with the derived seismograms (Aki and Richards, 1980). Seismometer, as a conventional seismological tool, can just detect lateral and vertical variations in velocity based on several stations installed on the ground so that there is no direct information about the damage caused by surface movement. Traditional geodetic instruments such as total station survey and levelling can be applied to directly measure the surface deformation after earthquakes, but this method is labour-intensive and time-consuming, and can just be applied in limited scale. Since the late 1980s, the Global Positioning System (GPS) was widely used for measuring crustal movement (Arnadóttir and Segall, 1994, Murray et al., 1996, Hudnut et al., 1996, Bilich et al., 2008, Shi et al., 2010, Inuma et al., 2011) owing to its ability to continuously measure three-dimensional deformation at a high frequency with the precision of up to a few millimetres (Segall and Davis, 1997). Even though GPS is a spatial technology which depends on continuously receiving signals from a number of satellites in the space, only the measurements of the ground-based stations can be obtained. In other word, the sparse distribution of GPS stations or even no stations installed around the epicentre areas results in less constrains or no data for earthquake monitoring. That situation is more common in developing countries or politically unrest regions (e.g. Iran and Iraq) owing to expensive instruments and operating cost.

However, Interferometric Synthetic Aperture Radar (InSAR), as a modern space-born technique, has proved its advantages of earthquake monitoring since the first successful application (Massonnet et al., 1993). InSAR can remotely map the surface deformation caused by earthquakes with sub-centimetre accuracy, high spatial resolution and large spatial coverage under all-day and all-weather operating conditions. The launch of a series of SAR satellites since 1991 has gradually improved this technique for earthquake monitoring (Table 1.1). The past SAR satellites generally operated with a revisit time of over one month, making it difficult to timely acquire the data over the disaster areas and potentially exacerbating the temporal decorrelation (Zebker and Villasenor, 1992). The spatial resolution of these SAR satellites is also relatively low. However, the current new generation SAR satellites have been improved with a shorter revisit time ranging from one day (e.g. CSK under the constellation) to about two weeks. Especially for the ALOS-

2 (L-band) and Sentinel-1A/B (C-band) satellites launched in 2014 and 2016, respectively, the former can acquire SAR images with shorter repeat circle and higher spatial resolution compared to its first generation satellite ALOS-1, the latter is characterised with the novel Terrain Observation by Progressive Scans (TOPS) SAR mode. TOPS SAR data can cover a total swath width of 250km at about 5m by 20m resolution in the range and azimuth directions, respectively (Torres et al., 2012, De Zan and Guarnieri, 2006). With available SAR data from multiple sensors, InSAR technique has been widely applied in mapping surface deformation. In particular, many previous earthquake applications also demonstrated that InSAR technique is a powerful tool for earthquake monitoring (Massonnet et al., 1993, Wright et al., 2003, Atzori et al., 2009, Beavan et al., 2012, Feng et al., 2017, Cheloni et al., 2017). However, InSAR can only provide the surface changes along the radar line-of-sight (LOS) direction. It is not sensitive to the deformation along the north-south direction due to the near-polar orbits of SAR satellites (Wright et al., 2004b). In addition, several limitations such as atmospheric delay, phase unwrapping error and decorrelation in spatial and temporal domain may bring some problems in InSAR applications to earthquake studies.

InSAR technique and GPS are complementary so that the combination of them can provide a better constraint for the source model. With InSAR measurements, it guarantees the co-seismic deformation along the LOS direction with large spatial coverage (hundreds of kilometre) and high spatial resolution (at metre level). Multiple sensors with different imaging geometries (e.g. looking angles) and wavelengths (X-, C- and L-band) also contribute to the diversity of independent datasets. With GPS data, accurate point-wise three dimensional deformations based on several ground stations can be obtained. The integration of InSAR and GPS measurements can improve our understanding of the pattern of co-seismic deformation and the results of geodetic modelling. In this study, I utilize InSAR technique and GPS measurement to map the co-seismic deformations of three most recent earthquake events, and the source model and slip distribution on the faults of each event are inverted with the geodetic modelling.

Table 1.1 Previous and current SAR satellite missions with their basic information

Satellite	Agency	Operation	Wavelength	Revisit Time (days)	Resolution (m)	Imaging Mode (Spatial Coverage)
ERS-1/2	ESA	1991-2000/ 1995-2011	C	35	~25	StripMap (100km)
JERS-1	JAXA	1992-1998	L	44	~18	StripMap (75km)
Radarsat-1	CSA	1995-2013	C	24	~11	Spotlight (45km)
					~25	StripMap (100km)
ENVISAT	ESA	2002-2012	C	35	~100	ScanSAR (300km)
					~30	StripMap (100km)
ALOS-1	JAXA	2006-2011	L	46	~150	ScanSAR (400km)
					~7-88	StripMap (40-70km)
					~100	ScanSAR (350km)

						~10	Spotlight (50km)
Radarsat-2	CSA	2007-Present	C	24		~25	StripMap (100km)
						~50	ScanSAR (300km)
TerraSAR-X (TSX)	DLR	2007-Present	X	11		~1	Spotlight (10km)
						~3	StripMap (30km)
						~16	ScanSAR (100km)
COSMO- SkyMed-1/4	ASI	2007-Present	X	1-15		~≤1	Spotlight (10km)
						~3-15	StripMap (40km)
						~100	ScanSAR (200km)
ALOS-2	JAXA	2014-Present	L	14		~1	Spotlight (25km)
						~3/6/10	StripMap(50-70km)
						~100	ScanSAR(350km)
Sentinel-1A/B	ESA	2014-Present/ 2016-Present	C	6/12		~4	StripMap (80km)
						~20	IW* (250km)

* IW is the Interferometric Wide Swath Mode, three sub-swaths are imaged in the Terrain Observation by Progressive Scans (TOPS) SAR mode.

1.3.5 Coulomb Stress Change

Since the aftershock sequence, alternatively post-seismic deformation brings serious threat to the epicentre area after the main shock, it is essential to assess the distribution of post-seismic earthquake activities in the region. The Coulomb stress changes analysis provides us an opportunity to explain the spatial distribution of the following aftershocks, or even to give a timely emergency response of areas where the potential aftershocks may occur. In addition, the Coulomb stress changes induced by large earthquakes can have a significant impact not only on their source faults, but also the surrounding active faults in the region. The stress released during a major earthquake could perturb the status of internal stress of the neighbouring active faults, inhibiting or bringing them closer to failure. Therefore, the triggering relationship between the source faults and the active faults in the vicinity of them can be evaluated based on the Coulomb stress changes. In other words, the risk of potential seismic hazards on the neighbouring active faults can also be assessed. Based on an elastic dislocation theory (Okada, 1985, Okada, 1992), the source geometry and slip distribution of the major earthquakes can be determined by geodetic modelling with InSAR and GPS data. With modelled internal displacements (distributed slips) on the causative fault planes, the Coulomb stress changes on the fault planes themselves and the neighbouring active fault planes can be calculated based on Coulomb Failure Function (Harris, 1998) which is written as:

$$\Delta CFF = \Delta\tau + \mu \cdot (\Delta\sigma_n - \beta \cdot T / 3) \quad (1.1)$$

Where $\Delta\tau$ is the shear stress change, μ is the friction coefficient, $\Delta\sigma_n$ is the normal stress change, β is the Skempton's coefficient and T is the stress tensor trace. Many previous studies indicated that the Coulomb stress change analysis is a useful tool to demonstrate the spatial distribution of aftershocks (King et al., 1994, Stein et al., 1997). Furthermore, the Coulomb stress change analysis has been successfully applied to assess the potential of seismic hazards on the neighbouring active faults around the previous major earthquakes. The calculation of Coulomb stress changes for the 26 December 2004 M_w 9.1-9.3 Sumatra–Andaman Earthquake in Indonesia found the stress increase on the Nias-Simeulue section of the Suda megathrust (McCloskey et al., 2005). Then the 2005 M_w 8.6 Nias–Simeulue earthquake occurred on that section after three months (Pollitz et al., 2006). Li et al. (2013) investigated the Coulomb stress changes induced by the 2008 M_w 7.9 Wenchuan Earthquake for the regional faults around this area, indicating the

stress increase of 0.05-0.25MPa on the Huya Fault, the Minjiang Fault and the Tazang Fault. The 2017 M_s 7.0 Jiuzhaigou Earthquake struck the northwestward extension of the Huya Fault, and Shan et al. (2017) and Zhao et al. (2018) also demonstrated that the 2017 Jiuzhaigou Earthquake was probably triggered by the 2008 Wenchuan Earthquake. Therefore, the Coulomb stress change analysis of the major earthquakes plays an important role in the assessment of potential seismic hazards on the source faults and the neighbouring active faults in the surrounding region. Based on the inverted distributed slips on the faults, the Coulomb stress change can be estimated to evaluate the potential seismic hazards, which is an important aspect of this thesis.

1.4 Contribution

This dissertation investigates the integration of DInSAR and GPS for mapping co-seismic deformation and geodetic modelling, and assesses the potential seismic hazards based on Coulomb stress change. Specific key contributions are:

- The performance of ALOS-2 (L-band) and Sentinel-1A/B (C-band) satellites for co-seismic monitoring of major Earthquakes (the 2015 M_w 7.8 Nepal earthquake, the 24 August 2016 M_w 6.2 Amatrice Earthquake and the 2017 M_w 7.3 Kermanshah Earthquake) is investigated.
- The linear surface features over the epicentre area of the 2017 Kermanshah Earthquake were preliminarily explored by a combination of DInSAR measurements and high spatial resolution optical images to verify whether they were fault ruptures or secondary co-seismic hazards.
- The Coulomb stress change analysis has been applied to investigate the relationship between the stress variation and aftershock distribution, the triggering relationship between the source fault and neighbouring active faults, and to assess the risk of potential earthquake activities over the epicentre area for three major events above.

1.5 Thesis Outline

There are a total of seven chapters in this dissertation. The current chapter briefly introduces the background of the study and objectives.

Chapter 2 provides a concise review of SAR systems, the basic principle of InSAR technique and DInSAR technique for mapping co-seismic deformation. The detailed SAR

data processing flow of DInSAR technique is presented. The limitation of DInSAR technique is also discussed in Chapter 2.

Chapter 3 provides a brief introduction of co-seismic geodetic modelling strategy. A process flow of geodetic modelling consisting of non-linear and linear inversion is presented along. Coulomb stress change analysis is also presented in Chapter 3.

Chapter 4 presents the source models and slip distributions of 25 April 2015 M_w 7.8 Nepal Earthquake and the 12 May 2015 M_w 7.2 aftershock inverted from DInSAR and GPS measurements. ALOS-2 ScanSAR and Sentinel-1A TOPS SAR data are used to map the co-seismic deformation of both events. The triggering relationship between the main shock and this significant aftershock is evaluated.

Chapters 5 and 6 are written based on manuscripts that have been published, accepted or submitted for publication by scientific journals or conferences during the period of candidature.

Chapter 5 investigates the co-seismic deformation and source model of the 24 August 2016 M_w 6.2 Amatrice (Central Italy) Earthquake using DInSAR and GPS measurements. Both L-band (ALOS-2) and C-band (Sentinel-1A/B) data are used to explore the co-seismic deformation pattern of the main shock. The interaction between this event and the following two major shocks is preliminarily investigated based on the Coulomb stress change analysis. The results presented in this chapter are published in the *2017 Australian Space Research Conference (ASRC)*.

Chapter 6 explores the source model of the 12 November 2017 M_w 7.3 Kermanshah (Iran-Iraq border) Earthquake using five tracks of SAR data consisting of ALOS-2 ScanSAR and Sentinel-1A/B TOPS SAR images. The linear surface ruptures are further investigated by the combination of DInSAR measurements and high spatial resolution images from SuperView-1 satellites. The triggering relationship and the risk of potential seismic hazards on the regional active faults are evaluated based on the Coulomb stress change analysis. This chapter is based on materials published in the *2018 IEEE International Geoscience and Remote Sensing Symposium (IGARSS)*, and accepted for publication in the *International Journal of Remote Sensing* on 17 July 2018.

Chapter 7 summarizes the major results of the case studies presented in Chapters 4 to 6, and it includes recommendations for future work.

Chapter 2 DInSAR Technique for Mapping Co-seismic Displacement Field

Differential Interferometric Synthetic Aperture Radar (DInSAR) technique plays an important role in mapping crustal deformation since its first successful application in 1993. In this chapter, brief review of InSAR technique for earthquake monitoring is presented in section 2.1, followed by the overall workflow and processing steps of DInSAR in section 2.2. Then 2.5 dimensional (2.5D) deformation analysis derived from DInSAR measurement is described in section 2.3. In addition, limitations of DInSAR technique is also discussed in section 2.4.

2.1 Introduction

In 1993, DInSAR technique was firstly introduced to investigate ground deformation caused by the 1992 Landers Earthquake, which suggested that this technique can provide much denser spatial coverage than field surveying, and higher accuracy than other space imaging techniques (Massonnet et al., 1993). Since this successful application with DInSAR technique, geologists and geophysicists realized the potential of this technique for earthquake study. More and more earthquake studies and applications were carried out with DInSAR technique for measuring co-seismic deformation (Massonnet and Feigl, 1995b, Massonnet et al., 1996, Wright et al., 2003, Fielding et al., 2005, Ge et al., 2008, Atzori et al., 2009, Atzori et al., 2012), post-seismic deformation (Fialko, 2004, Ryder et al., 2007, Barbot et al., 2009), and inter-seismic deformation (Biggs et al., 2007, Wang et al., 2009, Garthwaite et al., 2013).

The advantage of DInSAR technique for mapping crustal movement is large spatial coverage and the high accuracy of up to centimetre or millimetre (Massonnet and Feigl, 1998). Compared with field surveying (e.g. levelling, total station and GPS), DInSAR can provide repeat measurements under all-weather condition with all-day operation. DInSAR technique has been gradually matured through the launch of a series of SAR satellites. For example, (Massonnet et al., 1993) firstly used the SAR data from ERS-1 (C-band) to capture the surface movement caused by the 1992 Landers Earthquake (California). The 2003 Bam (Iran) Earthquake was investigated by Envisat ASAR (C-band) data (Funning et al., 2005). Shen et al. (2009) measured the co-seismic deformation caused by the 2008 Wenchuan Earthquake (China) using ALOS PALSAR (L-band) data.

Atzori et al. (2009) studied the 2009 L'Aquila Earthquake (Central Italy) with the Envisat (C-band) and COSMO-SkyMed (X-band) DInSAR measurements. The 2015 Mw 7.8 Gorkha (Nepal) Earthquake was studied by jointly using the SAR data from ALOS-2 (L-band), Sentinel-1A (C-band) and Radarsat-2 (C-band) satellites (Feng et al., 2017). However, L-band SAR data is expected to generate high quality interferogram for mapping co-seismic deformation in areas covered by dense vegetation owing to its longer wavelength than X- and C-band. In the case of large earthquakes, phase saturation (phase fringes in the interferogram are saturated owing to the large deformation within a small spatial coverage) is likely to occur with shorter wavelength data (e.g. C-band) mapping, which could result in the underestimation of co-seismic deformation. In contrast, L-band data is more sensitive to ionospheric perturbations that would probably introduce more ionospheric noise into the interferograms (Mouginot et al., 2012, Rignot and Mouginot, 2012). In this research, SAR data from the new generation SAR satellites ALOS-2 (L-Band) and Sentinel-1A/B (C-band) are jointly used for mapping co-seismic deformation caused by earthquakes owing to their short revisit time and high spatial resolution. The combined use of two bands can serve as an independent verification to each other.

2.1.1 Synthetic Aperture Radar System

The first civilian Synthetic Aperture Radar (SAR) satellite is the NASA SEASAT satellite which was launched on 27 June 1978 for ocean study. A series of spaceborne SAR missions were launched during 1990's, with ERS-1 satellite from the European Space Agency (ESA) launched in 1991, followed by JERS-1 from the Japan Aerospace Exploration Agency (JAXA) in 1992, Radarsat-1 from the Canadian Space Agency (CSA) and ERS-2 from ESA in 1995. Since 2000, more spaceborne SAR satellites were launched around the world (Table 2.1), including Envisat-1 from ESA in 2002 and ALOS-2 from JAXA in 2006. Now there are four SAR systems still in orbit to image the earth, including Radarsat-2 from CSA since 2007, COSMO-SkyMed system consisting of four satellites from the Italian Space Agency (ASI) since 2007, TerraSAR-X operated by the German Aerospace Centre (DLR) since 2007, ALOS-2 from JAXA since 2014, Sentinel-1A/B from ESA since 2014. These new generation SAR satellites image the earth with a revisit time ranging from only one day to nearly half month. Throughout this dissertation, SAR images from ALOS-2 and Sentinel-1A/B satellites are the major data for the research of the most recent earthquake events.

Table 2.1 Outline of radar satellite missions with their key parameters

Satellite	Frequency Band (Polarization)	Operation	Revisit Time (day)	Spatial Coverage (km)	Resolution (m)	Incidence Angle (°)	Organization , Country
Seasat	L (HH)	1978	17	100km	~25	22	NASA/JPL, USA
ERS-1/2	C (VV)	1991-2000/ 1995-2011	35	StripMap (100km)	~25	20-26	ESA, Europe
JERS-1	L (HH)	1992-1998	44	StripMap (75km)	~18	32-38	NASDA, Japan
Radarsat-1	C (HH)	1995-2013	24	Spotlight (45km)	~11	20-49	CSA, Canada
				StripMap (100km)	~25		
ENVISAT	C (Dual)	2002-2012	35	ScanSAR (300km)	~100	15-45	ESA, Europe
				StripMap (100km)	~30		
ALOS-1	L (Quad)	2006-2011	46	ScanSAR (400km)	~150	8-60	JAXA, Japan
				StripMap (40-70km)	~7-88		
				ScanSAR (350km)	~100		

TerraSAR-X	X (Quad)	2007-present	11	Spotlight (10km)	~1	15-60	DLR/Astrium, Germany
				StripMap (30km)	~3		
				ScanSAR (100km)	~16		
Radarsat-2	C (Quad)	2007-present	24	Spotlight (50km)	~10	30-50	CSA, Canada
				StripMap (100km)	~25		
				ScanSAR (300km)	~50		
COSMO-SkyMed-1/4	X (Dual)	2007...2010-present	1-15	Spotlight (10km)	~≤1	20-60	ASI/MiD, Italy
				StripMap (40km)	~3-15		
				ScanSAR (200km)	~100		
ALOS-2	L (Quad)	2014-present	14	Spotlight (25km)	~1	8-70	JAXA, Japan
				StripMap (50-70km)	~3/6/10/		
				ScanSAR (350km)	~100		
Sentinel-1A/B	C (Dual)	2014...2016-present	6, 12	250/TOPS	~20/TOPS	29-46	ESA, Europe

SAR system is characterised with its side-looking geometry, as shown in Figure 2.1. The radar sensor moves along the flight path (azimuth direction) and views the objects on the ground along the cross-track direction (range direction). Radar antenna transmits short radar pulses at a known rate (pulse repetition frequency) and receives the returned echoes of these pulses scattered by the objects on the surface (Hanssen, 2001). It is noted that the SAR antenna actually measures the range distance along the line-of-sight (LOS) direction between itself and the target object on the ground, which is also called the slant range measurement.

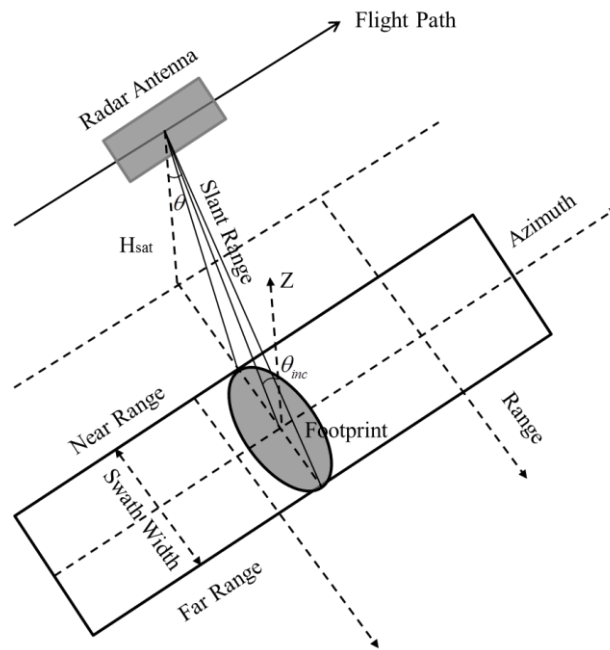


Figure 2.1 SAR viewing geometry

2.1.2 The Principle of DInSAR Technique

There are three ways to conduct DInSAR processing, including two-pass, three-pass and four-pass methods (Massonnet et al., 1993, Zebker et al., 1994, Hanssen, 2001). However, three-pass and four-pass approaches are less suitable for mapping surface deformation since more topographic error and atmospheric disturbance from other images could be included into the final products. Thus, two-pass DInSAR technique is used for measuring co-seismic deformation in this study. In two-pass DInSAR processing, two SAR images are required for interferogram generation, one is used as the 'Master image' and another one as the 'Slave image'. Both SAR images used for two-pass DInSAR processing are captured by the same radar antenna with the same imaging area and same viewing geometry at different times. However, two images are typically acquired at slightly

different positions, which contribute to the formation of baseline B between two images taken at different times, as shown in Figure 2.2. The Master and Slave are two different positions of SAR sensor along the same flight path when it captures these two images at different times. B_{\perp} is the perpendicular baseline, defining the effective distance between two acquisitions. α is the angle between baseline B and the horizontal plane. θ and θ_0 are the look angle to the imaged target and the reference surface, respectively. θ_{inc} is the incidence angle. And $\Delta\theta$ is the difference between θ and θ_0 . R and $R + \Delta r$ are the range distance between the same imaged object p on the ground and two different acquisitions in the Master and Slave positions, respectively. H_{sat} and H are the height of SAR satellite and the imaged object p , respectively.

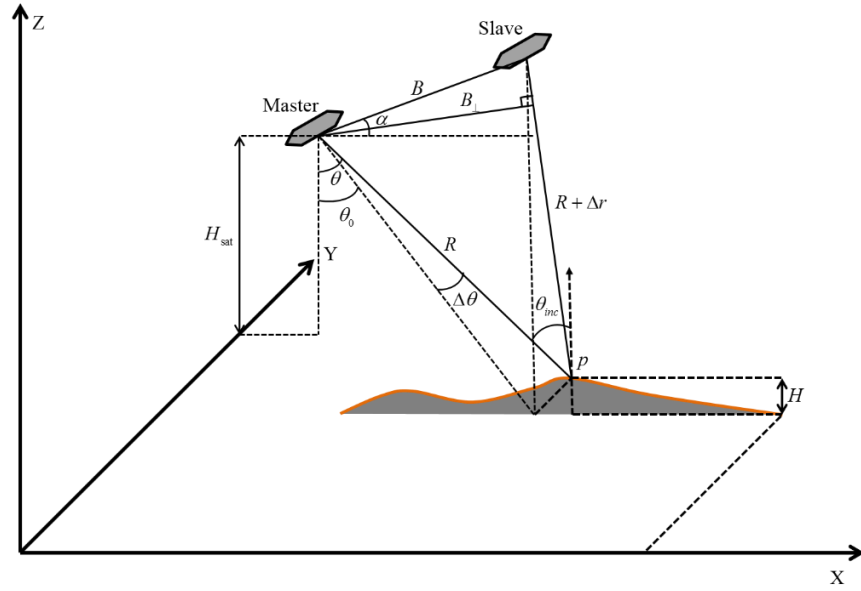


Figure 2.2 Two-pass DInSAR imaging geometry

The observed phase value ϕ_{master} and ϕ_{slave} of the two SAR images for a resolution cell can be expressed as (Bamler and Hartl, 1998, Hanssen, 2001):

$$\begin{aligned}\phi_{master} &= -\frac{4\pi}{\lambda} R + \phi_{scat, master} \\ \phi_{slave} &= -\frac{4\pi}{\lambda} (R + \Delta r) + \phi_{scat, slave}\end{aligned}\tag{2.1}$$

Where R and $R + \Delta r$ are the range distance from the imaged resolution cell to the radar antenna in the Master and Slave positions, respectively. λ is the wavelength of radar

sensor. $\phi_{\text{scat, master}}$ and $\phi_{\text{scat, slave}}$ are the backscattering phase in the master and slave images, respectively. When ignoring the phase delay due to atmosphere and assuming the backscattering phase in two images are totally the same. The interferometric phase between these two images can be written as:

$$\phi = \phi_{\text{master}} - \phi_{\text{slave}} = -\frac{4\pi}{\lambda}(R - (R + \Delta r)) = \frac{4\pi}{\lambda} \Delta r \quad (2.2)$$

When assuming $R \gg B$, Equation (2.2) can be written as:

$$\phi \approx -\frac{4\pi}{\lambda} B \sin(\theta - \alpha) \quad (2.3)$$

The flat earth phase due to earth ellipsoid can be written when assuming the topography is absent on the reference surface (Hanssen, 2001):

$$\phi_{\text{flat}} = -\frac{4\pi}{\lambda} B \sin(\theta_0 - \alpha) \quad (2.4)$$

Where ϕ_{flat} is the flat earth phase. By removing this phase from ϕ in Equation (2.3), the flattened interferometric phase can be written as:

$$\phi_{\text{flattened}} = \phi - \phi_{\text{flat}} \approx -\frac{4\pi}{\lambda} B \cos(\theta_0 - \alpha) \Delta\theta \quad (2.5)$$

The flattened interferometric phase $\phi_{\text{flattened}}$ includes the phase due to topographic variation referring to a reference surface and the surface deformation between two SAR images along the LOS dissection. When assuming there is no deformation occurred between the acquisition time of the Master and Slave images, the relationship between $\Delta\theta$ and the height of target H can be written as (Hanssen, 2001):

$$\Delta\theta \approx \frac{H}{R \sin(\theta_0)} \quad (2.6)$$

From Equation (2.5) and (2.6), the height of target on the ground can be estimated from the flattened interferometric phase.

The interferometric phase obtained from the equations above is just based on the physical and geometrical relationships between these two acquisitions (Hanssen, 2001). In the case of real data processing, the real interferometric phase can be decomposed into several

phases due to other factors including the topography surface, atmospheric delay, orbital error and noise. Therefore, the real interferometric phase can be rewritten as:

$$\phi = \phi_{\text{Topo}} + \phi_{\text{Defo}} + \phi_{\text{Orbit}} + \phi_{\text{Atmos}} + \phi_{\text{Noise}} \quad (2.7)$$

Where ϕ_{Topo} is the topographic phase, ϕ_{Defo} is the surface deformation between two images, ϕ_{Orbit} is the phase due to orbital error, ϕ_{Atmos} is the phase contributed from atmospheric disturbances, ϕ_{Noise} is the phase due to noise.

2.2 The procedures of two-pass DInSAR processing

The overall workflow of two-pass DInSAR processing used in this study is shown in Figure 2.3. The section 2.2.1-2.2.5 present and discuss each processing step in detail.

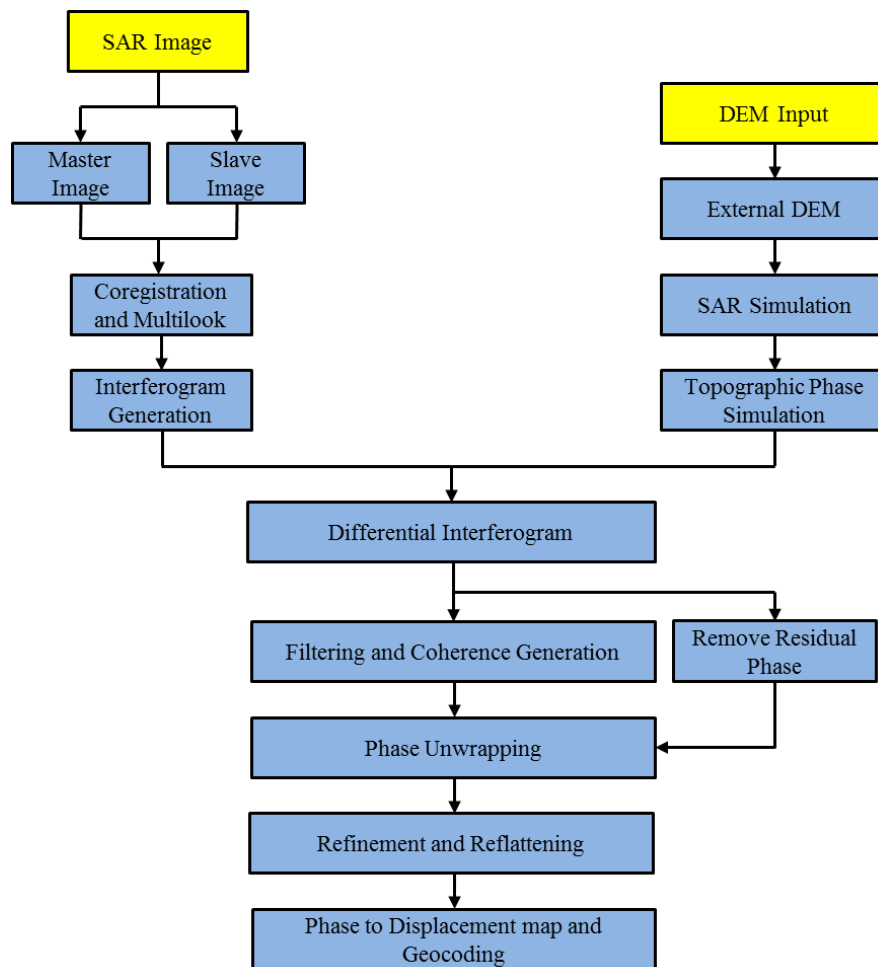


Figure 2.3 Two-pass DInSAR processing workflow

2.2.1 Co-registration and Interferogram Generation

Two SAR acquisitions consisting of pre- and post-seismic images are collected for mapping co-seismic deformation caused by an earthquake. The pre-seismic image is set as the Master image, and the post-seismic image as the Slave image. Before generating the interferogram, the Slave image is co-registered and resampled to the same grid referring to the Master image. The accuracy of co-registration between two images should be up to sub-pixel level. In this study, Sentinel-1A/B Terrain Observation by Progressive Scans (TOPS) SAR data is used for each event and the co-registration for this type of wide swath-width images is more demanding. Co-registration with an accuracy of about 1/1000th of one pixel in the azimuth direction is required due to the Doppler centroid frequency variations caused by azimuth beam sweeping (González et al., 2015). The complex interferogram can be generated by pixel by pixel complex conjugated multiplication between the Master and Slave images. After removing the flat earth phase (Equation (2.5)), this raw complex interferogram is composed of several components, as shown in Equation (2.7). However, the interferometric phase in this raw interferogram is wrapped in the interval $[-\pi, \pi]$, which is known as the relative interferometric phase. Thus, Equation (2.7) can be rewritten as (Hanssen, 2001):

$$\phi^W = W\{\phi_{\text{Topo}} + \phi_{\text{Defo}} + \phi_{\text{Orbit}} + \phi_{\text{Atmos}} + \phi_{\text{Noise}}\} \quad (2.8)$$

Where ϕ^W is the observed wrapped interferometric phase, $W\{\}$ denotes the wrapping operator.

From Equation (2.5) and (2.6), the topographic phase can be expressed as (Hanssen, 2001, Zebker et al., 1994):

$$\phi_{\text{Topo}} = -\frac{4\pi}{\lambda} \frac{B_{\perp}}{R \sin(\theta_0)} H \quad (2.9)$$

Using an external DEM, the topographic phase can be estimated and removed from the observed interferometric phase. The DEM is oversampled and then projected into the SAR imaging coordinate of the Master image to generate the simulated image. After co-registration between the simulated image and the Master image, the elevation of each pixel in the Master image can be retrieved from the DEM.

When assuming all the other phase components are removed and the topographic phase is subtracted from the interferometric phase, the phase due to surface deformation ϕ_{Defo} can be written as (Hanssen, 2001, Ferreti et al., 2007):

$$\phi_{\text{Defo}} = -\frac{4\pi}{\lambda} \Delta r \quad (2.10)$$

Where λ is the wavelength of radar antenna, Δr is the deformation occurred between the two acquisitions along the LOS direction.

A multi-look processing can be carried out to reduce the noise by averaging adjacent pixels in the flattened interferogram with the topographic phase removed. Basically this processing sacrifices the original high geometric resolution to the phase accuracy (Rodriguez and Martin, 1992). In the processing of ALOS-2 StripMap SAR single look complex (SLC) data with pixel spacing of 6.59m in the range direction and 3.11m in the azimuth direction, a multi-look ratio of 3 by 8 is adopted for obtaining a roughly square pixel cell on the ground, as shown in Figure 2.4.

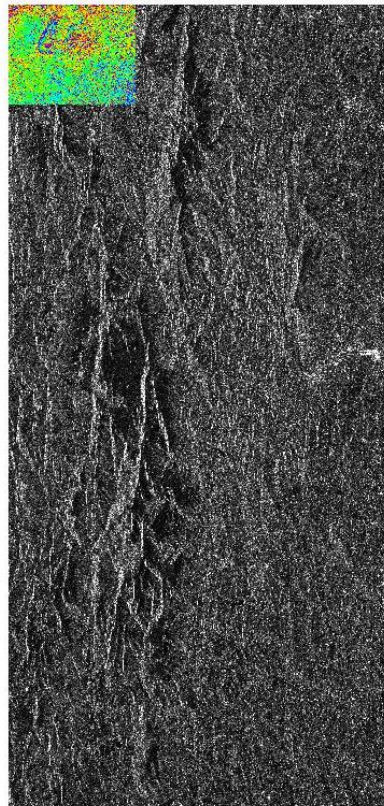


Figure 2.4 Multi-look interferogram from ALOS-2 StripMap data overlaid on the Master intensity image with original pixel size

2.2.2 Filtering and Coherence Generation

To further improve the Signal-to-Noise Ratio (SNR) of the differential interferogram generated above, an adaptive filter known as the Goldstein filter (Goldstein and Werner, 1998) is applied in this study. The Goldstein interferogram window size can be set to control the strength of filtering with the value of power of 2 ranging from 32 (light) to 512 (strong). Also, the filter strength also depends on the value of the Goldstein maximum/minimum Alpha parameters. The higher this parameter is, the stronger is the filter smoothing. Figure 2.5(a) and (b) show the example of the interferograms before and after the filtering.

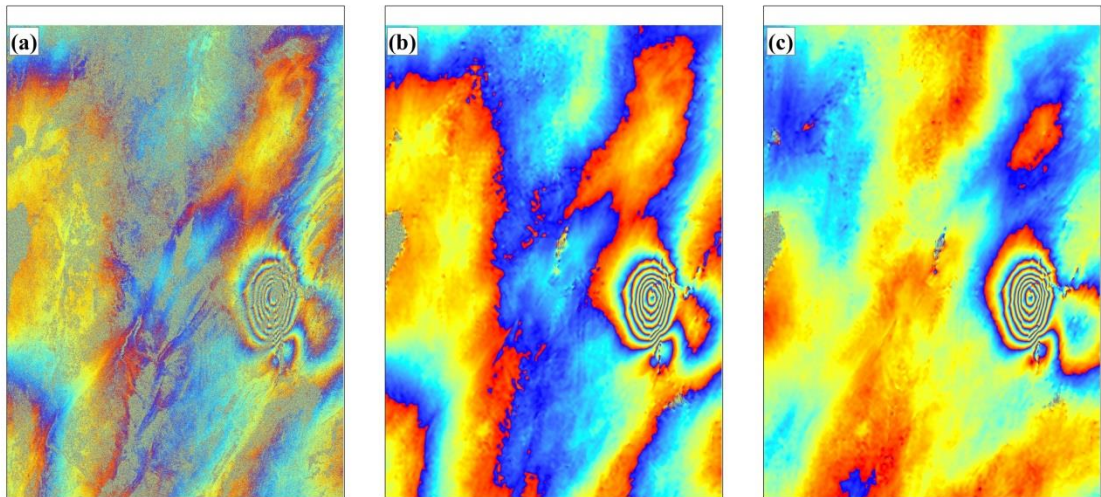


Figure 2.5 (a) Differential interferogram, (b) filtered interferogram and (c) filtered interferogram with the linear trend removed

As shown in Figure 2.5(b), a linear trend is observed all around the interferogram owing to orbital error. A linear function, consisting of slant range coordinate (range, azimuth) and error phase was estimated afterwards, with phase observations on the non-deforming areas to remove the residual phase and orbital error. The parameters of azimuth window size, range window size and polynomial degree are adjusted for achieving the optimal correction. After removing the residual phase and orbital error phase, the result is shown as Figure 2.5(c). This processing aims to simplify the following phase unwrapping step.

A coherence map is also generated by estimating the cross-correlation coefficient between two SAR images. The value of coherence is an important measurement of the phase quality in the interferogram with a range from 0 (totally noisy) to 1 (completely

correlated). The estimation of coherence γ can be written as (Patri and Rocca, 1992, Gatelli et al., 1994, Rocca et al., 1994):

$$\gamma = \frac{E[u_1(x)u_2(x)^*]}{\sqrt{E[|u_1(x)|^2]E[|u_2(x)|^2]}} \quad (2.11)$$

Where $E[\cdot]$ is the expectation value, $u_1(x)$ and $u_2(x)$ represent the complex value from the Master and Slave images, respectively. $*$ is the complex conjugate. As an example, a coherence map corresponding to the interferogram in Figure 2.5 is shown in Figure 2.6. The brighter is the data point, the higher is the value of coherence.



Figure 2.6 The coherence map corresponding to the interferogram in Figure 2.5

2.2.3 Phase Unwrapping

As shown in Equation (2.8), the interferometric phase we measured in the interferogram above is wrapped as the relative phase, modulo of 2π radians. In order to obtain the absolute phases, an important processing step called phase unwrapping should be conducted. The aim of phase unwrapping is to resolve the problem of phase ambiguity

and finally obtain the absolute phase for each pixel, as shown in Equation (2.12) (Ferreti et al., 2007):

$$\psi = \phi + 2\pi \cdot n \quad (2.12)$$

Where ψ is the unambiguous phase, and n is the integer ambiguity number. If no prior information about ϕ is available, the absolute phase cannot be retrieved easily. Even though the forward problem of wrapping the absolute phase to the interval $[-\pi, \pi)$ is straightforward, the inverse problem is extremely difficult owing to its inherent non-uniqueness and non-linearity (Ghiglia and Pritt, 1998, Hanssen, 2001). Also, other phase components due to topographic residual, atmospheric delay and noise make this problem much more complex.

Without any additional information and assumption, it is not possible to solve this problem. Therefore, two general assumptions are usually applied to resolve this inverse problem (Hanssen, 2001):

1. The phase gradients of the wrapped phase is the same as that of the unwrapped phase
2. The true phase difference of adjacent pixels should not exceed π (half of one cycle)

There are various algorithms based on these two assumptions above for resolving this problem, including branch-cut method (Goldstein et al., 1988), least-squares method (Ghiglia and Romero, 1996, Pritt, 1996), minimal cost flow (MCF) method (Costantini, 1998, Flynn, 1997) and SNAPHU (Chen and Zebker, 2000). In this study, the minimal cost flow method is the basic algorithm used for phase unwrapping because this method can provide a reasonable and robust result under the condition of low coherence and fast phase gradients caused by earthquakes. The areas with low coherence can be masked out by setting a proper coherence threshold. In addition, if the areas with low coherence are distributed all around the area of interest, the unwrapping decomposition level can be adjusted for reducing phase unwrapping error since the interferogram is first unwrapped in a lower resolution and then retrieved the original resolution.

2.2.4 Refinement and Re-flattening

After phase unwrapping, the absolute phase obtained is relative to one of the pixel cell in the unwrapped interferogram. If this reference pixel cell is located near the deformation

zone or on the residual phase, a phase offset or ramp would be added into the whole interferogram. Therefore, the processing of refinement and re-flattening is important to refine the orbital error, estimate the phase offset and remove possible phase ramp before transforming the phase to true displacement and geocoding the final product.

There are two general refinement methods used in this study, including orbital refinement and polynomial refinement. Both methods require the selection of Ground Control Points (GCP). Orbital refinement is used for correcting the orbital error by estimating the orbital correction parameters with at least 7 GCP points selected. The second method, polynomial refinement, is adopted to remove the residual phase or phase ramp without considering the orbital information. The parameter of residual phase polynomial degree ranging from 1 to 3 (integer) can be applied to this method. The polynomial function can be written as:

$$\phi_{\text{poly}} = k_1 + k_2x + k_3x^2 \quad (2.13)$$

In case of the removal of a phase offset, the polynomial degree should be set as 1. In this study, the polynomial refinement method with Ground Control Points (GCP) is the major refinement method since most of orbital error or linear trend is removed with a linear function, as discussed in section 2.2.2.

There are several criterions for the selection of GCP points' locations:

1. GCP points should not be located in the areas with residual topographic phase.
2. GCP points should not be located near the deformation fringes.
3. GCP points should not be located around the areas with unwrapping error
4. GCP points should be not located in the areas with low coherence
5. GCP points should be selected to cover the whole frame of interferogram if orbital error is observed

2.2.5 Phase to Displacement and Geocoding

Phase to displacement conversion is the processing that relates the unwrapped phase to deformation based on the Equation (2.10). Each 2π radian change of unwrapped phase is corresponding to half of wavelength of displacement along the LOS direction. However, each pixel cell with the information of deformation still remains in the azimuth-range coordinate system after phase to displacement conversion. The final step is geocoding which refers to a coordinate transformation. Generally, the final result is geocoded to a

Geographic Coordinate System such as WGS84 with a uniform grid. At the same time, two geocoded maps containing the LOS azimuth and incidence angle, respectively, are generated together. These two maps are essential for the following 2.5D displacement analysis and geodetic inversion for earthquakes. Most importantly, final products projected into the Universal Transverse Mercator (UTM) projection system for the convenience of geodetic inversion based on an elastic dislocation model (Okada, 1985).

2.3 The 2.5D Displacement Field Analysis

The final displacement Δr obtained from two-pass DInSAR processing is measured along the LOS direction. As Figure 2.7 shown, the DInSAR LOS displacement vector Δr is a composite of eastward, northward and vertical displacement components, which can be written as (Fialko et al., 2001, Ng et al., 2011, Ng et al., 2012):

$$\begin{bmatrix} \cos \theta & -\sin \theta \cos \alpha & \sin \theta \sin \alpha \end{bmatrix} \begin{bmatrix} D_U \\ D_E \\ D_N \end{bmatrix} = \Delta r \quad (2.14)$$

Where α is the azimuth of the radar satellite heading vector (positive clockwise from the North), θ is the radar incidence angle at the reflection point, D_U , D_E and D_N are the displacement vectors along the vertical, eastward and northward directions, respectively.

With the configuration of the current SAR satellites (near-polar orbit), the DInSAR measurement is not sensitive to the displacement components along the north-south direction (Ng et al., 2012). And it is much more difficult to retrieve the north-south displacement component from the DInSAR measurement owing to the small angle between the heading directions of the ascending and descending orbits (Ng et al., 2012, Wright et al., 2004b). However, when assuming the displacement in the north direction is negligible, the vertical and east-west displacement components can be estimated through weighted least squares fitting (Ng et al., 2011). The Equation (2.14) can be rewritten as:

$$\begin{bmatrix} \cos \theta & -\sin \theta \cos \alpha \end{bmatrix} \begin{bmatrix} D_U \\ D_E \end{bmatrix} = \Delta r \quad (2.15)$$

The vertical and east-west displacement components can be estimated as:

$$D_{U,E} = (B_{U,E}^T P B_{U,E})^{-1} S_{U,E}^T P r \quad (2.16)$$

Where $D_{U,E}$ is unresolved vector of displacement components $\begin{bmatrix} D_U \\ D_E \end{bmatrix}$, $B_{U,E}$ is the matrix of coefficient vectors relative to these two displacement components, P is the weighting matrix generated from the precision of each DInSAR measurements.

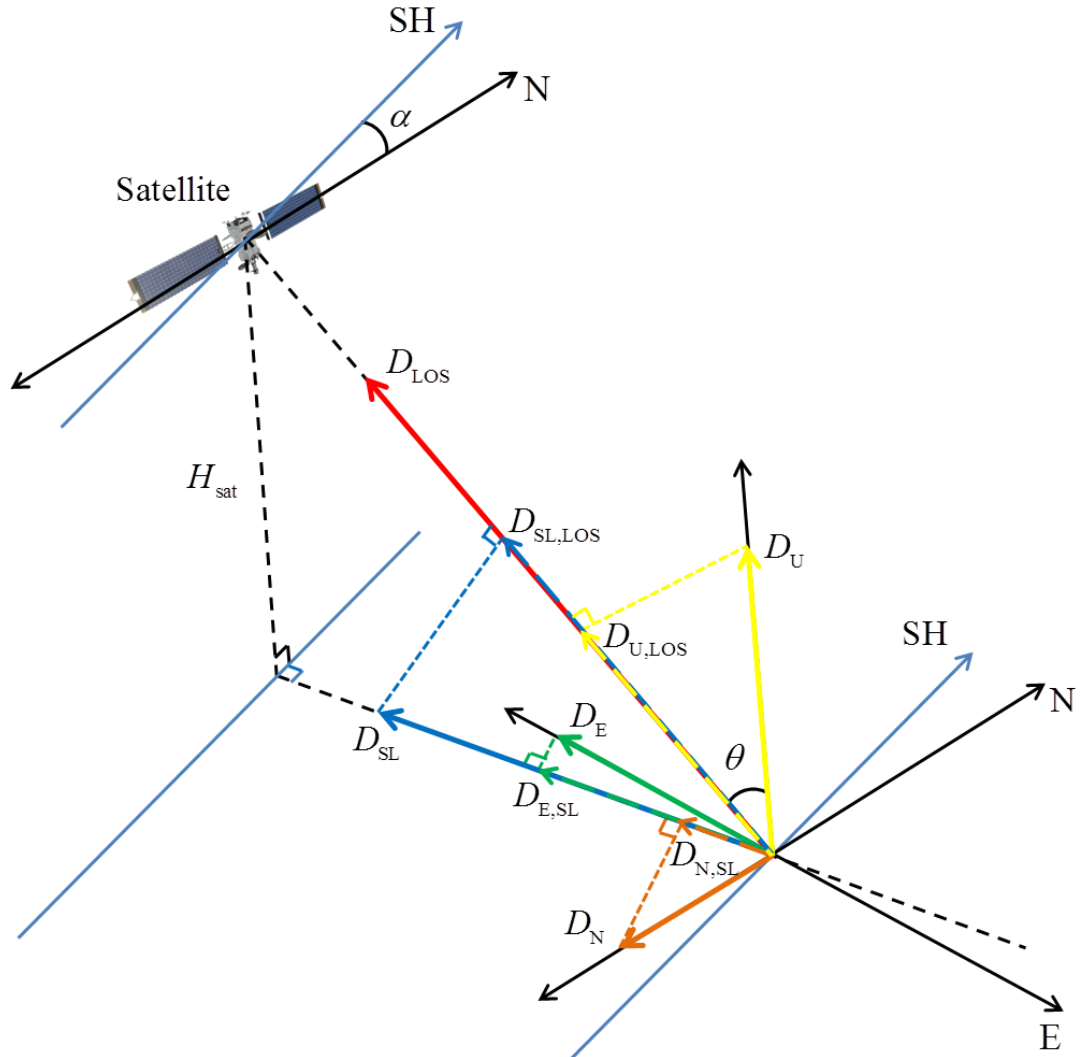


Figure 2.7 Decomposition of the LOS displacement vector from DInSAR measurement.

SH represents the satellite heading direction, SL represents the satellite looking direction projected on the ground, α is the azimuth of satellite heading vector (positive clockwise from the North), θ is the incidence angle at the reflection point, D_{LOS} is the LOS displacement vector, D_U , D_E and D_N are vertical, eastward and northward displacement, respectively.

In the case of the strike-slip fault of earthquake basically striking along the north-south direction, the displacement component along the north direction should not be ignored since the north-south displacement component is comparable with the displacement along the other two directions.

2.4 Limitations of DInSAR Technique

DInSAR technique plays an important role in monitoring surface deformation on the Earth. However, the problem of decorrelation in spatial and temporal domain brought more challenges to the data processing and applications. Also, error sources such as atmospheric disturbances and orbital inaccuracies make it more difficult to obtain the accurate surface deformation and the subsequent result interpretation. These limitations of DInSAR techniques are discussed as followed.

Spatial decorrelation, also called geometric or baseline decorrelation, is introduced by the difference in the viewing angles of two SAR images, which would degrade the quality of interferogram. The larger is the perpendicular baseline (B_{\perp} , as shown in Figure 2.2) between two acquisitions, the more significant is the difference of the viewing angles. That makes the coherent sum of the scatterers in a resolution pixel more different, leading to these two measurements being not exactly the same (Zebker and Villasenor, 1992). Therefore, if the perpendicular baseline is large, the spatial decorrelation is more significant as well. The spatial decorrelation can be expressed as (Hanssen, 2001, Bamler and Hartl, 1998, Zebker and Villasenor, 1992):

$$|\gamma_{\text{spatial}}| = \begin{cases} 1 - \frac{B_{\perp}}{B_{\perp,\text{critical}}}, & |B_{\perp}| \leq B_{\perp,\text{critical}} \\ 0, & |B_{\perp}| > B_{\perp,\text{critical}} \end{cases} \quad (2.17)$$

Where $|\gamma_{\text{spatial}}|$ is the estimation of correlation owing to spatial decorrelation, $B_{\perp,\text{critical}}$ is the critical baseline which causes the backscatter from each pixel cell to be totally uncorrelated (Gatelli et al., 1994, Zebker et al., 1994):

$$|B_{\perp, \text{critical}}| = \left| \frac{\lambda R \tan(\theta_{\text{inc}} - \zeta)}{2\rho} \right| \quad (2.18)$$

Where λ is the wavelength of the radar sensor, ζ is the topographic slope, and ρ is the slant range between radar antenna and the target point on the ground. Equation (2.18) also indicates that the longer is the wavelength, the larger is the critical baseline. That means the spatial correlation is better with longer wavelength.

Temporal decorrelation refers to the variation of the backscatter characteristics of distribution of scatterers within the resolution cell or the electrical characteristics, spanning the time period between two image acquisitions. The temporal decorrelation usually occurs over the areas of dense vegetation or snow-covered mountains where the scatterer characteristics changes over time (e.g. the vegetation growth of crop and forest, or snow coverage over the mountains and ground). Generally, SAR images acquired by shorter wavelength (C-band or X-band) are more sensitive to small changes in the scattering characteristics than those acquired by longer wavelength (L-band) (Rosen et al., 2000). Thus, using L-band SAR data can achieve a lower level of temporal decorrelation especially when investigating an areas with dense vegetation over a relatively longer time period. However, SAR image pair with shorter temporal baseline is preferred in two-pass DInSAR processing to decrease the temporal decorrelation.

Atmospheric disturbances are the phases due to the delay of radar signal when it travels through the atmosphere. The variation of water vapour, temperature and pressure in atmosphere between two acquisitions contributes different error phases to the DInSAR measurements and makes it difficult to interpretation for final results (Goldstein, 1995, Massonnet and Feigl, 1995a). However, the phase variation due to atmosphere is spatially correlated and relative to the topography. Also, the atmospheric phase variation is generally temporally correlated within a short period. Since the time separation for two acquisitions used for two-pass DInSAR is typically up to several days or weeks, the atmospheric phase is generally temporally uncorrelated in the final results. Two types of atmospheric phase variation can be identified based on its physical origin (Hanssen, 2001):

1. Turbulent mixing which is caused by the turbulent processes in the atmosphere.
2. The variation in the vertical stratification which is highly correlated with the topography.

2.5 Concluding Remarks

In this chapter we reviewed the DInSAR techniques. Two-pass DInSAR technique, as a space-borne remote sensing technique, can provide measurements of co-seismic deformation caused by earthquakes with the accuracy of centimetre to millimetre and the spatial coverage of hundred kilometres. Each major processing step of two-pass DInSAR technique is presented. Many previous case studies have proved that DInSAR technique is an effective and important tool for earthquake monitoring. The combination of ascending and descending DInSAR measurements can be applied to retrieve the east-west and vertical displacement vectors in the case of negligible north-south displacement component caused by earthquake. Noise from spatial and temporal decorrelation and atmospheric delay are the major factors that significantly affect the quality and accuracy of DInSAR measurements. The interferogram generated from L-band SAR data can achieve a higher level of coherence than C-band over the areas of dense vegetation.

With the new generation of SAR satellites, especially ALOS-2 and Sentinel-1A/B, more SAR image pairs with shorter temporal baseline and higher resolution can be obtained for mapping co-seismic deformation. That would make it more feasible to generate high quality DInSAR interferogram and provide valuable information about earthquake activities in near real-time. Chapter 3 will discuss and present how to use co-seismic deformation measured by InSAR and GPS to invert the earthquake source model from geodetic modelling.

Chapter 3 Geodetic Modelling from Co-seismic Deformation

Direct observations of earthquake sources are limited so that geodetic modelling is an essential tool to understand the source fault underground. Geodetic modelling of earthquake source parameters and slip distribution from geodetic data is described in this chapter. The procedure of geodetic inversion, non-linear and linear inversion is presented in Section 3.1, including forward modelling, data downsampling and weighting and modelled 3D co-seismic deformation field. The basics of the Coulomb stress change estimation are introduced in Section 3.2.

3.1 Geodetic Modelling Strategy

After obtaining the geodetic data for earthquake, the fault parameters and slip distribution of the causative fault can be determined by geodetic inversion based on a finite rectangle fault model in an elastic, homogeneous half-space (Okada, 1985, Okada, 1992). Geodetic inversion generally consisted of two steps: a non-linear inversion was adopted to constrain all the fault parameters with a uniform slip on a rectangular fault. Then, the slip distribution on the fault plane with extended length and width is inverted by a linear inversion. A forward modelling is applied to retrieve the simulated surface deformation based on the inverted fault geometry and slip distribution.

3.1.1 Source Fault Geometry Definition

To describe the geometry of the source fault, several fault parameters generally are applied, as shown in Figure 3.1 (Okada, 1985). Source fault is a finite rectangle plane located between the hanging wall and foot wall (Figure 3.1(a)). The black arrows between the hanging wall and foot wall show the dilation (opening) which is generally assumed to be zero in the earthquake source modelling. The red arrow BB' shows the relative displacement between the hanging wall and foot wall, representing the slip vector. When locating this rectangle fault plane in the Cartesian Coordinate System (CCS), nine fault parameters are used to describe the fault geometry and uniform slip (Figure 3.1(b)), namely length, width, depth, strike ϕ , dip φ , rake δ , strike-slip (S_s), dip-slip (S_d), the north and east coordinates of the centre of the plane. The fault trace is the intersected line of fault plane and the surface.

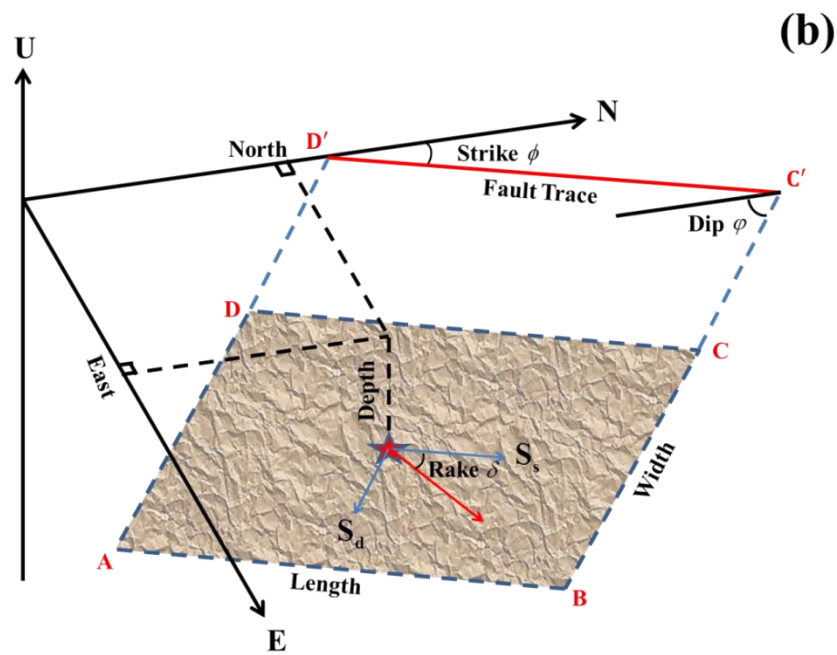
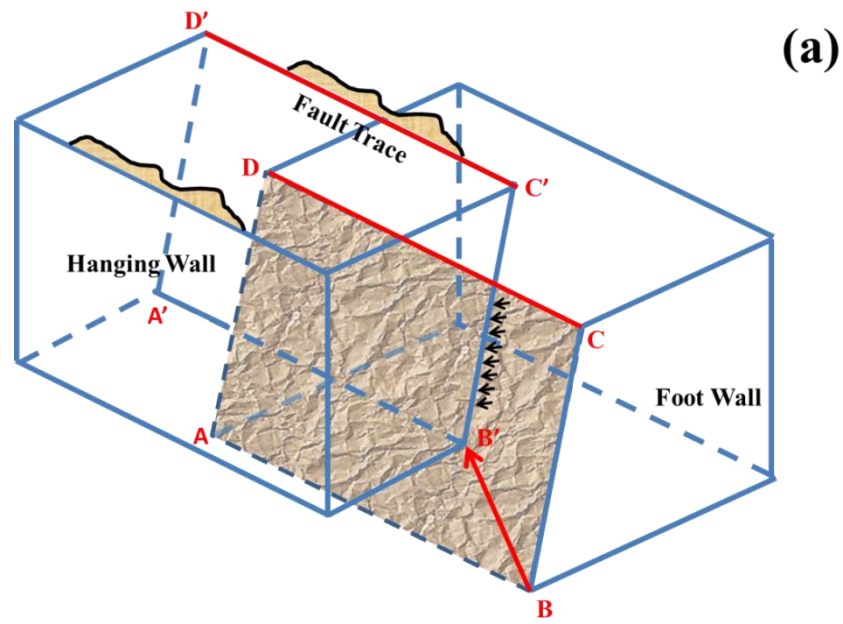


Figure 3.1 The geometry of source fault with key parameters. (a) Source fault with the hanging wall and foot wall. (b) The rectangle fault plane with source parameters in the Cartesian coordinate system. The red star indicates the centre of the fault plane.

The fault orientation is defined by the strike ϕ which is the angle calculated clockwise from the North to the fault trace on the surface, ranging from 0° to 360° . The dip ϕ is the angle calculated from the horizontal plane to the fault plane, ranging from 0° to 90° . The relationship between strike and dip follows the right-hand rule. The rake δ is the

angle between slip vector and the strike direction with a range of $[-180^\circ, 180^\circ]$. Different focal mechanisms can be described by these three angles (strike, dip and rake) (Aki and Richards, 1980). A rake of 0° represents that the hanging wall is moving to the right relative to the foot wall, which is the type of left-lateral motion; on the contrary, a rake of $\pm 180^\circ$ indicates the hanging wall is moving to the left relative to the foot wall, suggesting a type of right-lateral motion. When the rake is positive, the hanging wall is moving up relative to the foot wall, indicating a type of thrust fault ($\text{dip} < 45^\circ$) or reverse fault ($\text{dip} > 45^\circ$). If the rake is negative, the hanging wall is moving down relative to the foot wall, suggesting a type of normal fault (Shearer, 2009).

After defining the source model with nine fault parameters, the relationship between geodetic data (DInSAR and GPS measurements) and the source parameters can be expressed as:

$$d_{\text{observed}}(x, y) = \text{func}(m) + \nu \quad (3.1)$$

Where d_{observed} is the geodetic data from DInSAR and GPS measurements in a given location (x, y) on the ground. func is the function which connect all the source parameters ($m = m_1, m_2, m_3, \dots, m_n$) with the geodetic measurements. ν is the observation error from the geodetic data which generally exists in the real data (Aster et al., 2011, Tarantola, 2005). It is noted that seven parameters of the fault geometry (length, width, strike, dip, rake, north and east coordinates) are non-linearly related in a finite rectangle fault source (Okada, 1985), while the other two (strike-slip and dip-slip) related to the slip vector are linearly correlated. Therefore, inversion of these source parameters based on the geodetic data is a complex inverse problem.

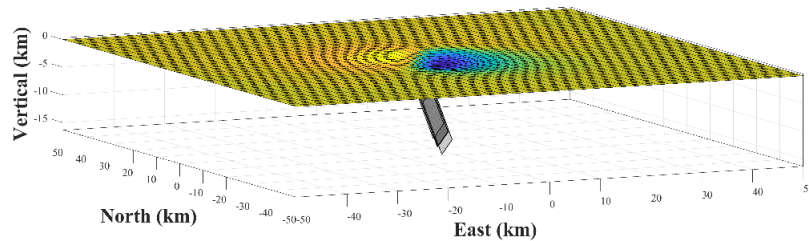
3.1.2 Forward Modelling

Using the source parameters to retrieve the surface displacement field is a forward problem. A typically used geophysical model is a finite rectangular source in an elastic, homogeneous half-space which was firstly introduced by (Steketee, 1958) and further improved by (Okada, 1985), also known as the Okada model. Source parameters generally can be describe as length, width, strike, dip, rake, strike-slip, dip-slip, East and North coordinates of the centre of fault plane, as shown in Figure 3.1(b). The forward problem can be simply expressed as:

$$d_{\text{model}}(x, y) = \text{func}(m) \quad (3.2)$$

Where d_{model} is the modelled surface displacement in a given point (x, y) . m represents the source parameters ($m = m_1, m_2, m_3, \dots, m_n$). The surface deformation can be modelled based on the fault geometry on the Cartesian coordinate system and the uniform slip vector. An example of a finite rectangle source fault and the corresponding modelled displacement in the vertical direction is shown as Figure 3.2, suggesting the modelled displacement contributed from a 20km×10km fault with striking 30°NE and dipping 70°SE. Then the modelled displacements are projected into the LOS direction.

(a)



(b)

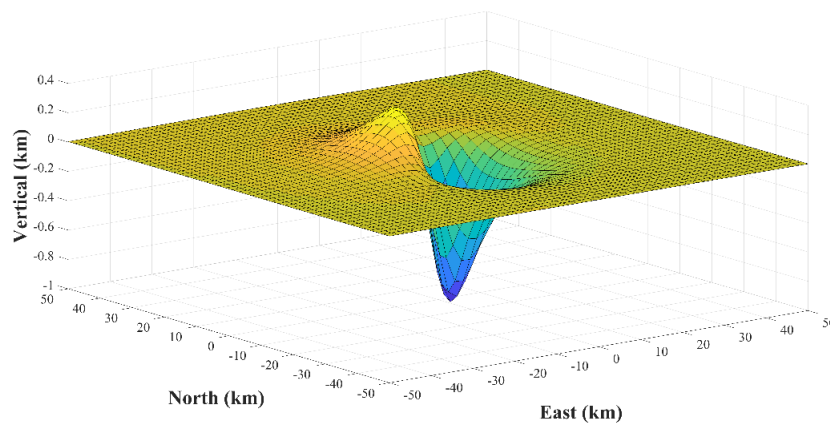


Figure 3.2 Forward modelling of surface displacement based on the Okada model. (a) a finite rectangle source fault overlapping with the modelled vertical displacement in 3D view. (b) The modelled vertical displacement in 3D view.

3.1.3 InSAR Data Downsampling

Compared to the point-based GPS measurements, DInSAR displacement map can provide millions of observations with a spacing of a few metres owing to its large spatial

coverage. Since the DInSAR measurements show a high degree of spatial correlation, it is not necessary to use all the data points in the modelling. To improve the computational efficiency, an extremely large amount of observations from DInSAR measurements need to be removed before the geodetic inversion. There are two downsampling methods which are generally used for reduce the number of data points, Quadtree decomposition (Jónsson et al., 2002, Simons et al., 2002, Wang et al., 2007) and uniform grid sampling (Pritchard et al., 2002, Atzori et al., 2009). The Quadtree decomposition method is generally based on the deformation gradient to determine the downsampling level. High sampling frequency tends to be assigned near the areas of larger deformation. However, the possible error signal (e.g. atmospheric delay or topographic residual) from DInSAR data could result in oversampling over the areas where is far away from the deforming area. As for the uniform grid sampling method, a regular mesh is adopted to subsampling the DInSAR deformation map with a coarse grid lower than the original spatial resolution. Generally, rather than using the same mesh over the whole map, a manually adjusted regular mesh of higher density around the deforming area is adopted (Atzori et al., 2009). As shown in Figure 3.3, the Sentinel-1A/B DInSAR displacement map is downsampled with both methods. In this research, we basically use the uniform downsampling with various density of grid to reduce the data point of DInSAR measurements.

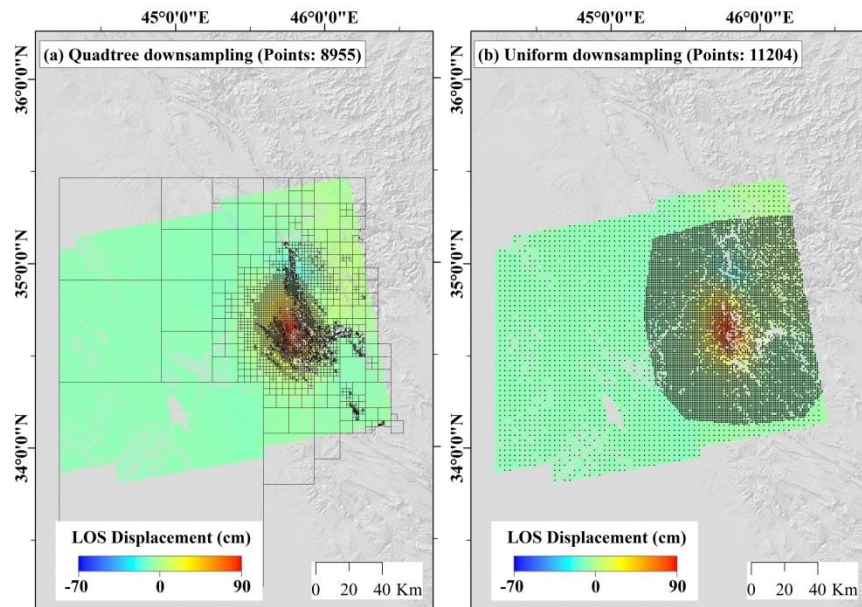


Figure 3.3 Comparison between different downsampling strategies. (a) Quadtree downsampling result, and (b) Uniform downsampling result with various density of grid for DInSAR displacement map.

3.1.4 Non-Linear Inversion

After obtaining the geodetic data, the source parameters of source fault can be inverted based on a uniform slip model. The source parameters include 8 geometric parameters (length, width, depth, strike, dip, rake, East and North) and only one parameter of slip vector. Therefore, under the assumption that geodetic data is non-linearly related to the source parameters, a non-linear inversion basically aims to determine the fault geometry. Optimized source parameters can be found when the square of the residual between the geodetic data d_{observed} (Equation (3.1)) and the modelled data d_{model} (Equation (3.2)) reaches the global minimum (Atzori and Salvi, 2014). In other words, with the best-fit source parameters on Equation (3.2), the modelled data best reproduces the geodetic data. A cost function can be expressed as a weight mean of residuals for the determination of global minimum, as shown in Equation (3.3):

$$CF = \sqrt{\frac{1}{N} \sum_i \frac{(d_{i,\text{observed}} - d_{i,\text{model}})^2}{\sigma_i}} \quad (3.3)$$

Where $d_{i,\text{observed}}$ and $d_{i,\text{model}}$ are observed and modelled data corresponding to i^{th} data point, respectively; σ_i is standard deviation for the N points.

A series of forward modelling (Equation (3.2)) is iteratively processed with the adjusting value of the source parameters to finally obtain the best-fit source parameters. There are several optimization algorithms used for the non-linear inversion. A down-hill simplex method incorporating the Monte-Carlo approach was adopted by (Wright et al., 1999) to estimate the best-fit model. A simulated annealing algorithm which do not require the priori information was applied to the non-linear inversion (Delouis et al., 2002). In this research, a mixed algorithm of Gauss-Newton iteration and gradient descent as the Levenberg-Marquardt (LM) least-squares approach (Marquardt, 1963) is adopted to solve this non-linear problem. This process is carried out with multiple random restarts (Atzori et al., 2009, Atzori and Antonioli, 2011), and initial parameters from the Global Centroid Moment Tensor Catalog (GCMT) solution (Dziewonski et al., 1981, Ekström et al., 2012) was carried out to search for a global minimum in the optimization process. It should be noted that in some cases several source parameters (e.g. strike or dip) could be deduced or fixed by the priori or additional information from surface rupture, aftershock distribution or seismic body-wave (Elliott et al., 2012, Feng et al., 2017).

3.1.5 Linear Inversion

After determining the fault geometry from the non-linear inversion, a linear inversion is adopted to invert the slip distribution on the fault plane. Fixing the fault geometry and extending the length and width of the fault plane to fully cover the epicentre area, all the parameters are linearly related to the surface deformation, as occurred with the slip vector along the strike and dip directions (Atzori and Salvi, 2014). Then the fault plane is subdivided into small patches along the strike and dip. The expression of linear inversion can be rewritten from Equation (3.1), as shown in Equation (3.4):

$$d_{\text{observed}} = GS + v \quad (3.4)$$

Where G is the Green's function matrix which relates the slip vector S to the surface deformation, S is the slip vector consisting of strike-slip (S_s) and dip-slip (S_d) as shown in Figure 3.1(b). Thus, the expression of slip vector can be written as Equation (3.5):

$$S = \begin{bmatrix} S_s \\ S_d \end{bmatrix} \quad (3.5)$$

The Green's function matrix also can be written as the form of two equal size matrices (G_s and G_d) corresponding to the directions of the strike slip and the dip slip:

$$G = \begin{bmatrix} G_s & 0 \\ 0 & G_d \end{bmatrix} \quad (3.6)$$

If there are n observation points from geodetic data and the fault plane is subdivided into N patches totally. With the Combination of Equation (3.4)-(3.6), the expression of linear inversion can be rewritten as Equation (3.7):

$$\begin{bmatrix} d_{\text{observed}}^1 \\ \vdots \\ d_{\text{observed}}^n \end{bmatrix} = \begin{bmatrix} \begin{matrix} X_1 \\ \vdots \\ X_N \end{matrix} \begin{matrix} G_s & \cdots & G_s & G_d & \cdots & G_d \\ \begin{matrix} P_1 \\ \vdots \\ P_N \end{matrix} & \ddots & \begin{matrix} P_N \\ \vdots \\ P_1 \end{matrix} & \vdots & \ddots & \vdots \end{matrix} \begin{bmatrix} S_s^1 \\ \vdots \\ S_s^N \\ S_d^1 \\ \vdots \\ S_d^N \end{bmatrix} \quad (3.7)$$

Where $G_{P_N}^{x_n}$ is the Green's function corresponding to the strike slip on the N^{th} patch, which is relative to the n^{th} observation point; $G_{P_N}^{x_n}$ is the Green's function corresponding to the dip slip on the N^{th} patch, which is relative to the n^{th} observation point; S_s^N and S_d^N are the strike slip and the dip slip on the N^{th} patch, respectively; d_{observed}^n is the n^{th} observation point from geodetic data.

In the case of medium spatial resolution of the slip distribution, the number of observation points is generally more than the number of unknown slip vectors on the corresponding fault patch. Therefore, this linear problem is generally over-determined, and the least square sense on geodetic data can be applied to invert the modelled slip vector S_{model} as written in Equation (3.8) (Atzori and Salvi, 2014):

$$S_{\text{model}} = G^{-g} d_{\text{observed}} \quad (3.8)$$

Where G^{-g} is the generalised inverse of G (Menke, 2018), and can be written as the form including the Green's function in Equation (3.9) (Lohman, 2004, Atzori and Salvi, 2014):

$$G^{-g} = [G^T G]^{-1} G^T \quad (3.9)$$

However, the slip vector solved from the Equations (3.8) and (3.9) are generally unrealistic owing to the weak control ability of geodetic data on the fault parameters. To avoid extremely high values or slip oscillations in the result, a two-dimensional two-order Laplacian operator ∇^2 can be adopted to constrain the slip vector in two directions (Harris and Segall, 1987, Jonsson, 2002). Combining the Equations (3.4)-(3.6), the final equation can be written as Equation (3.10):

$$\begin{bmatrix} d_{\text{observed}} \\ 0 \\ 0 \end{bmatrix} = \begin{bmatrix} G_s & G_d \\ \varepsilon \nabla^2 & 0 \\ 0 & \varepsilon \nabla^2 \end{bmatrix} \begin{bmatrix} S_s \\ S_d \end{bmatrix} \quad (3.10)$$

Where the Green's function here is the original Green' function in Equation (3.6) extended with a Laplacian operator ∇^2 , also called the smoothed Green's function. A

Laplacian operator ∇^2 is also weighted by an empirical coefficient ε to assist the selection of a smooth distributed slip model (Wright et al., 2003). By substituting Equation (3.10) with Equations (3.8) and (3.9), the modelled slip vectors on each patch can be obtained. The empirical coefficient ε , also called damping factor, is determined based on the trade-off curve between the misfit of measurement and the solution roughness of slip distribution (Jónsson et al., 2002, Wright et al., 2004a). The solution roughness can be estimated as the mean, absolute Laplacian of the slip distribution (Jónsson et al., 2002), as written in Equation (3.11):

$$\rho = \frac{\sum_i |p_i|}{2N} \quad (3.11)$$

Where $p = \nabla^2 S$ and N represents the total number of the small patches on the fault plane. Different values of damping factor would generate different optimal solutions. High values resulted in a large misfit; low values would lead to small misfit, but with large oscillation in slip distribution. An optimal damping factor can be chose from the trade-off curve between the misfit of measurement and the solution roughness of slip distribution, which can achieve low misfit and small roughness at the same time.

3.1.6 Weight Strategy

As Equation (3.1) and (3.4) shown, data error generally exists in each type of dataset, which can significantly influence the data quality. Therefore, weighting based on data quality (InSAR and GPS) is typically considered in the inversion. Generally, variance and covariance is the important quantitative measurements of data quality or error which help to assign different weights for various datasets. Regarding to GPS dataset, it is weighted by the standard deviations of measurements in three directions (East/North/Vertical) under an assumption that there is no spatial correlation between GPS stations. However, as for InSAR data, smoothly changing atmospheric phase delay shows the characteristic of spatially correlation, while the phase decorrelation and unwrapping error is spatially uncorrelated (Sudhaus and Sigurjón, 2009, Sudhaus, 2010, Hanssen, 2001). Thus, the data variance and covariance are estimated using experimental semi-variograms and covariograms, respectively, under an assumption that the data error is quasi-stationary and isotropic (Chilès and Delfiner, 1999, Sudhaus and Sigurjón, 2009). After removing the linear trend from the interferogram, the experimental semi-variogram is generated by

sampling many data points separated with different distance h in different directions, which can be expressed as:

$$\hat{\gamma}(h) = \frac{1}{2N} \sum_{i=1}^N [z(r_i) - z(s_i)]^2 \quad (3.12)$$

Where N is the number of data pairs at locations r_i and s_i separated by the lag distance h . Obviously, the values of semi-variogram depend on the lag distance h . Also, the experimental covariogram can be expressed in a similar form:

$$\hat{C}(h) = \frac{1}{2N} \sum_{i=1}^N z(r_i) \cdot z(s_i) \quad (3.13)$$

Then a positive-definite exponential function is used to fit the experimental covariogram in order to retrieve a continuous covariance (Chilès and Delfiner, 1999, Sudhaus and Sigurjón, 2009). After that, the variance-covariance matrix of the completed dataset can be built by using the variance of each data point for the diagonal value and covariance for the corresponding point pair. Therefore, the weighting matrix W is generated based on the variance-covariance matrix Σ can be generated as:

$$W = \Sigma^{-1} \quad (3.14)$$

Another solution is that the variance-covariance matrix for InSAR data error is built by assuming that the errors can be modelled using an exponential function with nugget, fitted to isotropic experimental semi-variogram (Webster and Oliver, 2007). The expression of the experimental semi-variogram here is the same as Equation (3.12). Three parameters (Sill, Range and Nugget) are used to describe the best-fitting exponential function with nugget. The experimental semi-variogram is estimated over an area of the interferogram where there is no deformation signal. At the same time, the linear trend in the interferogram is also removed. An example of the experimental semi-variogram and the estimated exponential function with nugget is shown in Figure 3.4. The range, nugget and sill are estimated with 10309.83m, $3.7534 \times 10^{-7} \text{m}^2$, and $1.7917 \times 10^{-5} \text{m}^2$.

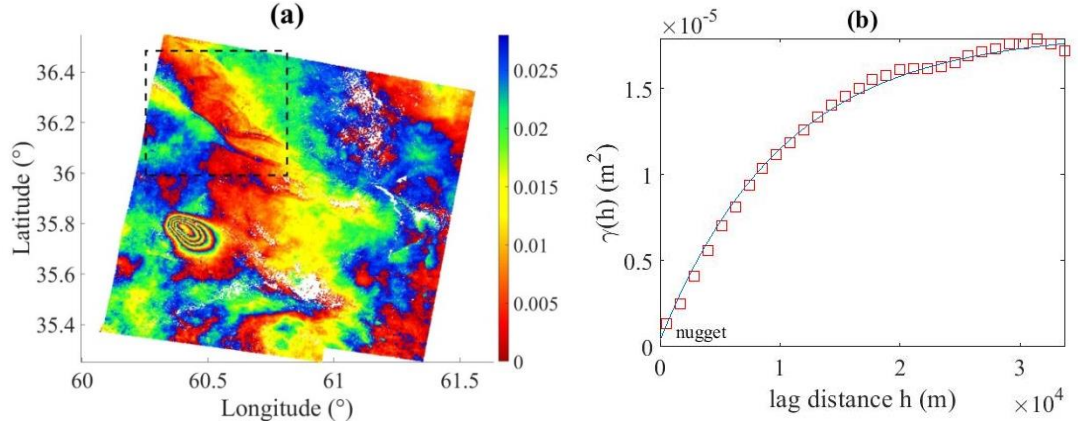


Figure 3.4 (a) co-seismic wrapped interferogram from Sentinel-1A/B image pairs, the dash rectangle represents the selected area for the sampling of semi-varigram; (b) results of experimental semi-varigram (red squares) and the fitting exponential function (blue line) with nugget.

After obtaining the data weighting matrix, the final expression of Equation (3.10) can be rewritten as:

$$\begin{bmatrix} Wd_{\text{observed}} \\ 0 \\ 0 \\ 0 \end{bmatrix} = \begin{bmatrix} WG_s & 0 \\ 0 & WG_d \\ \varepsilon \nabla^2 & 0 \\ 0 & \varepsilon \nabla^2 \end{bmatrix} \begin{bmatrix} S_s \\ S_d \end{bmatrix} \quad (3.15)$$

Where w is the weight matrix generated from the variance-covariance matrix. The general weighted Least Squares Estimation of Equation (3.15) can be written as:

$$S = (G^T W G)^{-1} G^T W d_{\text{observed}} \quad (3.16)$$

To increase the reliability of the source model, a non-negative least square algorithm is adopted to positively invert this system (Atzori and Salvi, 2014).

3.1.7 Modelled 3D Displacement Field

As we discussed in the section 2.3 of Chapter 2, DInSAR data can only provide the measurements of co-seismic deformation along the line-of-sight (LOS) direction. It is very difficult to retrieve the complete 3D displacement field with DInSAR ascending and descending measurements due to near-polar orbits of SAR satellites (Wright et al., 2004b). However, modelled 3D Displacement field caused by the inverted source model can be generated after the forward modelling as discussed in section 3.2.2. The modelled

displacement components along three directions (East/North/Up) are combined and projected into the radar LOS direction, which can be written as:

$$\begin{bmatrix} \cos \theta & -\sin \theta \cos \alpha & \sin \theta \sin \alpha \end{bmatrix} \begin{bmatrix} d_{U, \text{model}} \\ d_{E, \text{model}} \\ d_{N, \text{model}} \end{bmatrix} = d_{\text{LOS, model}} \quad (3.17)$$

Where α is the azimuth of the radar satellite heading vector (positive clockwise from the North), θ is the radar incidence angle at the reflection point, $d_{U, \text{model}}$, $d_{E, \text{model}}$ and $d_{N, \text{model}}$ are the modelled displacement along the vertical, east and north directions, respectively. $d_{\text{LOS, model}}$ is the modelled LOS displacement projected from three modelled displacement components. An example of 3D modelled displacement components is shown as Figure 3.5.

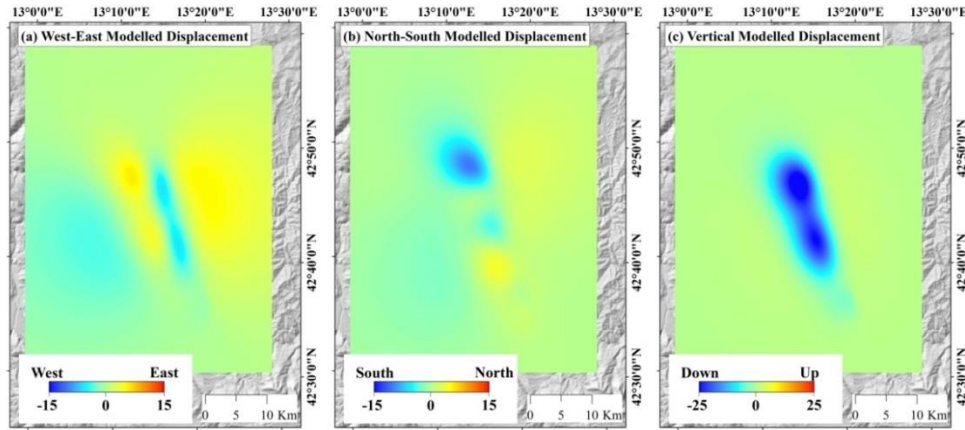


Figure 3.5 Modelled 3D displacement components in west-east, north-south and vertical directions, respectively

3.2 Coulomb Stress Change

When the long-term accumulated stress exceeds the internal strength of a fault, an earthquake occurs and then releases a large amount of stress. The absolute stress values of the specific fault are unknown owing to unknown stress loading rate and extremely long time spanning. However, the Coulomb stress change can be calculated from the information of the causative faults or the existing active faults. In other word, the Coulomb stress change is independent of the absolute stress over an area but mainly depends on the fault geometry, slip direction and the coefficient of friction (Harris, 1998,

King et al., 1994). Based on the Coulomb Failure Function, the stress change on a given fault plane with specific slip vector can be calculated with the expression (Harris, 1998):

$$\Delta CFF = \Delta\tau + \mu \cdot (\Delta\sigma_n + \Delta p) \quad (3.18)$$

Where ΔCFF represents the changes of the Coulomb Failure Function; $\Delta\tau$ is the shear stress change in the direction of slip (receiver fault); μ is the friction coefficient, $\Delta\sigma_n$ is the normal stress change (positive for unclamping); Δp is the pore pressure change. The isotropic poroelastic model assumes the pore pressure changes mainly depend on the volumetric stress change (Hainzl et al., 2010) which can be written as:

$$\Delta p = -\beta \left(\frac{\Delta\sigma_{kk}}{3} \right) \quad (3.19)$$

Where β is the Skempton's coefficient (Skempton, 1954) and $\Delta\sigma_{kk}$ is the stress tensor trace. Substituting stress tensor trace with \mathcal{T} and combining Equation (3.19), Equation (3.18) can be rewritten as:

$$\Delta CFF = \Delta\tau + \mu \cdot \left(\Delta\sigma_n - \beta \frac{\mathcal{T}}{3} \right) \quad (3.20)$$

This form of the Coulomb Failure Function is more general and feasible for different tectonic setting (Beeler et al., 2000). Positive Coulomb stress change ($\Delta CFF > 0$), representing that the Coulomb stress of a specific segment of the fault or area is increasing, tends to promote or even trigger earthquake activities over this area. On the contrary, negative Coulomb stress change ($\Delta CFF < 0$), indicating the Coulomb stress is decreasing, is likely to prevent or inhibit its failure. The Coulomb stress change is also highly correlated to aftershock distributions. Most of aftershocks following the main shock are located around the area of stress increase, and only a much smaller number of aftershocks occur over the area of stress decrease. In addition, future earthquake activities could be promoted when the Coulomb stress increases by as small as 0.01MPa (0.1 bar) (King et al., 1994, Stein, 1999, Ziv and Rubin, 2000).

Using the distributed slip model inverted from geodetic measurements as the main source, the Coulomb stress change on the causative fault plane itself can be calculated based on Equation (3.20). In addition, based on the known fault geometry and mechanism of the neighbouring active faults or previously studied faults, the Coulomb stress change on

these faults can be estimated by using them as the receiver faults. With the locations of the areas with positive stress change, the triggering relationship between the main shock and aftershocks can be evaluated over the affected region. Also, the Coulomb stress change on the neighbouring active faults gives us an overall evaluation of possible earthquake activities over these faults. Therefore, the Coulomb stress change calculation plays an important role in the assessment of the risk of seismic hazards.

3.3 Concluding Remarks

This chapter presented the mathematical model and detailed processing of geodetic modelling, including non-linear inversion for parameters of fault geometry and linear inversion for slip distribution. 3D co-seismic deformation components along the east, north and vertical directions can be generated from forward modelling based on the best-fitting source mode. The weighting matrix of geodetic data is built based on the variance-covariance matrix retrieved from the experimental semi-varigram. Also, the calculation of the Coulomb stress changes on the source fault or the neighbouring active faults is discussed. The combination of aftershock distribution and the Coulomb stress change allows us to assess the risk of seismic hazards over the target region.

In the next three chapters, the DInSAR processing technique described in Chapter 2 and the methods of geodetic modelling presented in this chapter will be applied in the case studies of major earthquakes.

Chapter 4 Co-seismic Deformation and Source Model of the 25 April 2015 M_w 7.8 Nepal Earthquake and the 12 May 2015 M_w 7.2 aftershock

In this chapter, the 2015 Nepal Earthquake sequence, both the main shock (M_w 7.8) on 25 April 2015 and the major aftershock (M_w 7.2) on 12 May 2015 are investigated by using co-seismic DInSAR and GPS measurements. Source model and slip distribution of both events are determined using geodetic inversion based on an elastic dislocation model. The optimised source model for the main shock shows a thrust fault striking 285.9° NW-SE and dipping 7.7° NE with a slight right-lateral component. The maximum slip of this event is up to 5.1m. The peak slip of distributed slip model for the major aftershock was found at the similar depth of main shock. The triggering relationship between main shock and major aftershocks is demonstrated based on the calculation of Coulomb stress change.

4.1 Introduction

On 25 April 2015, a significant earthquake with a magnitude of M_w 7.8 struck the central Nepal at 06:11:25 UTC, recorded by the United States Geological Survey (USGS). According to the USGS, the hypocentre of this event was located at 28.231°N , 84.731°E with a depth of 8.2km, about 80km NW of Kathmandu, the capital of Nepal. This destructive earthquake caused nearly 9,000 fatalities and 22,000 people injured. Within the first 45 days of the main shock, 553 aftershocks with local magnitude larger than 4.0 were recorded by the National Seismological Centre (NSC) and the Regional Seismological Centre (RSC). The relocated aftershocks shown in Figure 4.1 were collected from the (Adhikari et al., 2015), covering an area of approximately $220\text{km} \times 120\text{km}$. The largest aftershock with a magnitude of M_w 7.2 occurred on 12 May 2015, located about 140km SE of the main shock. More than 200 people were killed and over 2500 were injured during this major aftershock. Focal mechanism from the USGS and the Global Centroid Moment Tensor (GCMT) (Dziewonski et al., 1981) both show a co-seismic rupture occurred on a NW-SE striking, oblique-thrust fault with a low dip (6° from the GCMT and 7° from the USGS).

The epicentre of the 25 April Mw 7.8 main shock is located along the Himalayas, a huge mountain range generated by the collision between Indian Plate and Eurasian Plate with a rate of about 20mm year⁻¹ (Bilham et al., 1997, Lavé and Avouac, 2000, Stevens and Avouac, 2015). The collision between two plates also resulted in the highest and largest plateau in the world, the Tibetan Plateau. The Main Front Thrust (MFT) fault and the Main Himalaya Thrust (MHT) fault are the major active faults over this region. Historical earthquakes with $M_w \geq 7.0$ within 400km of this event indicated that the 2015 Nepal earthquake is not the largest event near this region. A magnitude of 8.0 (M_w) recorded by USGS occurred on 15 January 1934, located about 240km SE of this event. A smaller historical event with M_w 7.5 was recorded on 26 August 1833, located much closer to the main shock of the 25 April 2015 event (Szeliga et al., 2010).

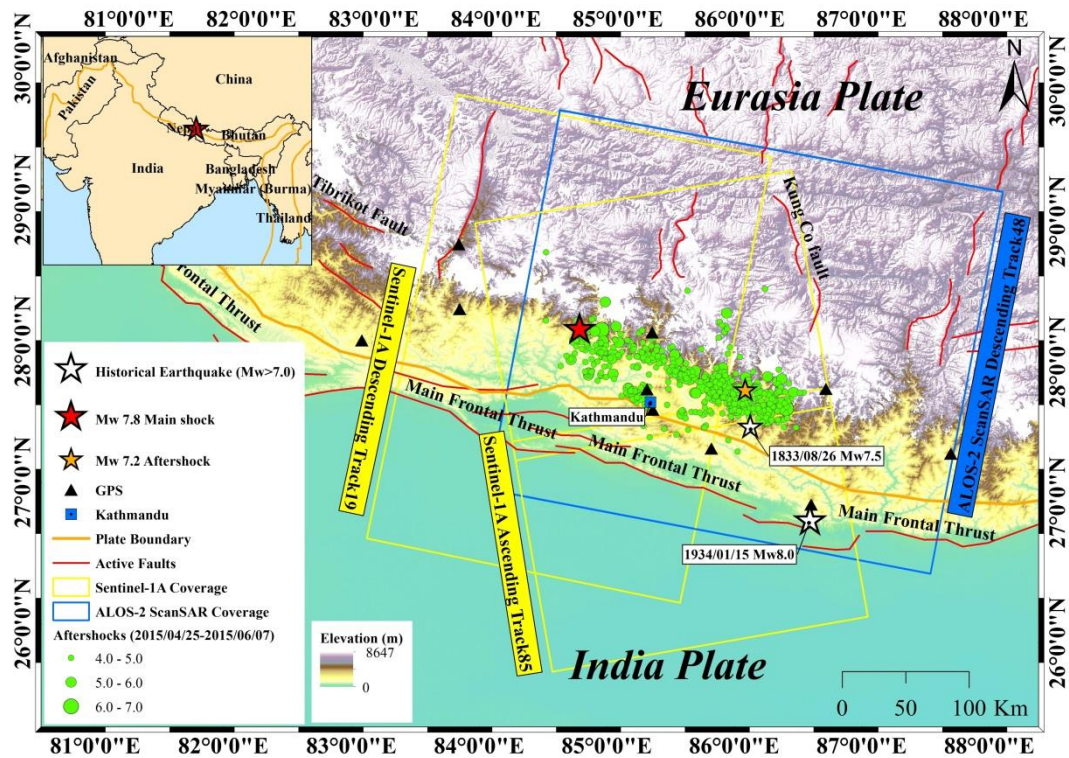


Figure 4.1 Geographical setting of the 25 April 2015 Mw 7.8 Nepal Earthquake and the 12 May 2015 Mw 7.2 Aftershock superimposed on the elevation map derived from 3-arc SRTM data (Farr et al., 2007). Red and orange stars show the epicentres of main shock and Mw 7.2 aftershock, respectively from USGS. Green dots are relocated aftershocks ($4.0 < M_w < 7.0$) within the first 45 days (Adhikari et al., 2015). White stars represent the large historical earthquakes ($M_w \geq 7.0$). Blue and yellow boxes show the spatial coverages of ALOS-2 and Sentinel-1A images used in this study. Black triangles are GPS stations. Red lines are active faults in this region (Styron et al., 2010).

Since the occurrence of the 25 April 2015 Nepal Earthquake, many researchers investigated this event using geodetic data. Wang and Fialko (2015) used the DInSAR observations from ALOS-2 data and GPS measurements to jointly model the co-seismic slip distribution and fault geometry for the main shock. Feng et al. (2015) jointly inverted the dataset of ALOS-2 descending ScanSAR, ascending StripMap and GPS data and revealed that a reverse fault with slight right-lateral strike-slip component. Feng et al. (2017) optimized the source model of this event using ALOS-2, Sentinel-1A, RADARSAT-2 and GPS data together. Fan and Shearer (2015) investigated the ruptures process of the main shock with globally recorded teleseismic P waves. Huang et al. (2017b) used the near-field and far-field high-rate GPS observations to explore the dynamic ground motions induced by the main shock. Wei et al. (2018) determined the co-seismic rupture process of the main shock using joint inversion of InSAR, GPS, strong motion and teleseismic waveforms.

In this study, the fault geometry and slip distribution of the 25 April 2015 M_w 7.8 main shock and the following 12 May 2015 M_w 7.2 aftershock were investigated using a joint inversion of DInSAR and GPS measurements based on an elastic dislocation model (Okada, 1985). Coulomb stress changes on the source fault of main shock and the M_w 7.2 aftershock were calculated to demonstrate the relationship with aftershock distribution. In addition, the triggering relationship between the main shock and the M_w 7.2 aftershock is discussed in Section 4.5.

4.2 Geodetic Data

4.2.1 SAR Data

In this study, we used two pairs of SAR images from ALOS-2 satellite operated by Japan Aerospace Exploration Agency (JAXA) and two pairs from Sentinel-1A satellite operated by the European Program Copernicus from European Space Agency (ESA) to generate four co-seismic interferograms for the 2015 M_w 7.8 Nepal Earthquake and the following significant aftershock with a magnitude of M_w 7.2. The detailed information for each pair is shown in Table 4.1. The wavelength of ALOS-2 and Sentinel-1A data are 22.9cm and 5.6cm, respectively. Both two pairs of ALOS-2 images used were acquired under the ScanSAR (Wide-Swath) mode with a swath of 350km. The Sentinel-1A image pairs were acquired in Terrain Observation by Progressive Scan (TOPS) mode with a swath width of 250km (Torres et al., 2012). The image coverage of each pair is shown in Figure 4.1.

The ALOS-2 ScanSAR images pairs used for the main shock and the Mw 7.2 aftershock were captured on the same track (Track 48). It is noted that the epicentre areas of main shock and aftershock are fully covered by both ALOS-2 ScanSAR image pairs used, while the Sentinel-1A image pair used for main shock only cover approximate 70% of the epicentre area. The temporal baseline of two image pairs used for mapping the significant aftershock are just 14 and 12 days owing to the short revisit time of these two new generation satellites. This suggests that SAR image with wide swath width plays an important role in mapping extremely large earthquake.

Table 4.1 Interferometric pairs used for the 2015 Nepal Earthquake Sequence

Event	Sensor	Track	Orbit	Image Mode	Interferometric	B_{\perp} (m)	B_T (d)	θ ($^{\circ}$)
					Pair (yyyy/mm/dd)			
M	A2	48	DESC	WD	2015/02/22- 2015/05/03	55.4	70	40.3
	S1A	19	DESC	IWS	2015/04/17- 2015/04/29	39.9	12	39.6
A	A2	48	DESC	WD	2015/05/03- 2015/05/17	100.7	14	40.3
	S1A	85	ASC	IWS	2015/05/03- 2015/05/15	94.0	12	39.6

A2 and S1A are ALOS-2 and Sentinel-1A, respectively. ASC and DESC are ascending and descending orbits, respectively. M and A represents the main shock and the Mw 7.2 aftershock, respectively. WD is Wide-Swath (ScanSAR) mode and IWS is Interferometric Wide Swath (TOPS) mode. B_{\perp} is perpendicular baseline, B_T is temporal baseline (day), θ is incidence angle.

4.2.2 DInSAR Measurements

The ALOS-2 and Sentinel-1A Single Look Complex (SLC) data were processed up to interferograms using the interferometric module of SARscape software. The multi-look ratio between range and azimuth direction was set as 1 by 5 and 8 by 2 looks for the ALOS-2 ScanSAR and Sentinel-1A images, respectively. We used the topographic phase

generated from the 3 arc-second Digital Elevation Model (DEM) from the Shuttle Radar Topography Mission (SRTM) (Farr et al., 2007) to remove the topographic effects. All the interferograms were then filtered using Goldstein Adaptive Filter (Goldstein and Werner, 1998) to further reduce the noise. Then, a linear function, consisting of slant range coordinate (range, azimuth) and error phase was estimated afterwards, with observations on the non-deforming areas to remove the residual phase and orbital error. After that, the interferograms were unwrapped using Minimum Cost Flow algorithm (Costantini and Rosen, 1999) and geocoded to WGS84 geographic coordinate.

The final displacement map for each pair is shown in Figure 4.2. Two long strip-like deformation areas along near west-east direction were observed from both pairs for the M_w 7.8 main shock, as shown in Figure 4.2(a, b). The length of deformation area is up to 140km. All of the deformation areas are located just between the epicentres of main shock and the M_w 7.2 aftershock occurred on 12 May from the USGS. The maximum LOS deformation is 99.1cm and 118.0cm for ALOS-2 and Sentinel-1A pairs, respectively. Regarding to the displacement maps for the M_w 7.2 aftershock, elliptic deformation area along west-east direction was observed on both sides of the epicentre of this event from ALOS-2 descending pair and Sentinel-1A ascending pair (Figure 4.2(c, d)). Both pairs show similar deformation pattern but with different maximum LOS deformation, 73.2cm for the ALOS-2 descending pair and only 68.8cm for the Sentinel-1A ascending pair. That could be caused by post-seismic deformation from small aftershock as the temporal baseline of ALOS-2 descending pair is longer than that of Sentinel-1A ascending pair.

To reduce the data points used for inversion and improve computation efficiency, two displacement maps of main shock were downsampled using a regular mesh with 1000m \times 1000m around the deforming area and 5000m \times 5000m for the rest area. However, owing to smaller deformation area caused by the M_w 7.2 aftershock, only the data points in the area between 27.0°N-28.9°N and longitude 85.3°E-86.9°E were preserved and then downsampled with the similar regular mesh with 500m \times 500m around the deforming area and 2000m \times 2000m for the rest. A total of 21591 points were obtained for the main shock, with 10760 for ALOS-2 and 10831 for Sentinel-1A, as shown in Figure 4.3(a, b). For the M_w 7.2 aftershock, a total of 28191 points were preserved, with 15794 for ALOS-2 and 12397 for Sentinel-1A (Figure 4.3(c, d)).

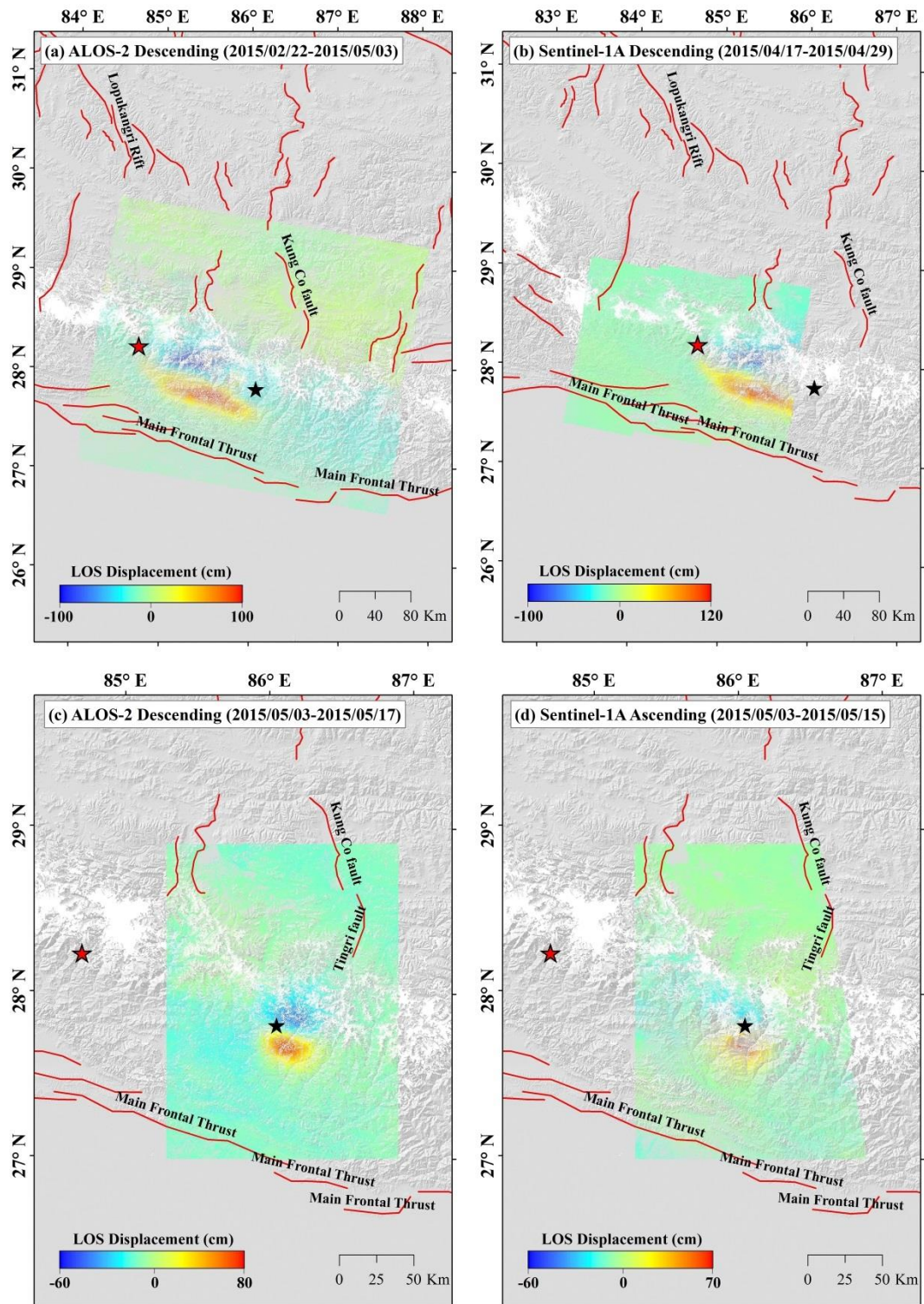


Figure 4.2 Co-seismic displacement maps of the 25 April M_w 7.8 Nepal Earthquake from (a)-(b) ALOS-2 and Sentinel-1A descending data and the 12 May M_w 7.2 aftershock from (c)-(d) ALOS-2 descending and Sentinel-1A ascending data. Red lines are active faults around this region. Red star and black star are the epicentres of main shock (M_w 7.8) and aftershock (M_w 7.2) from the USGS, respectively.

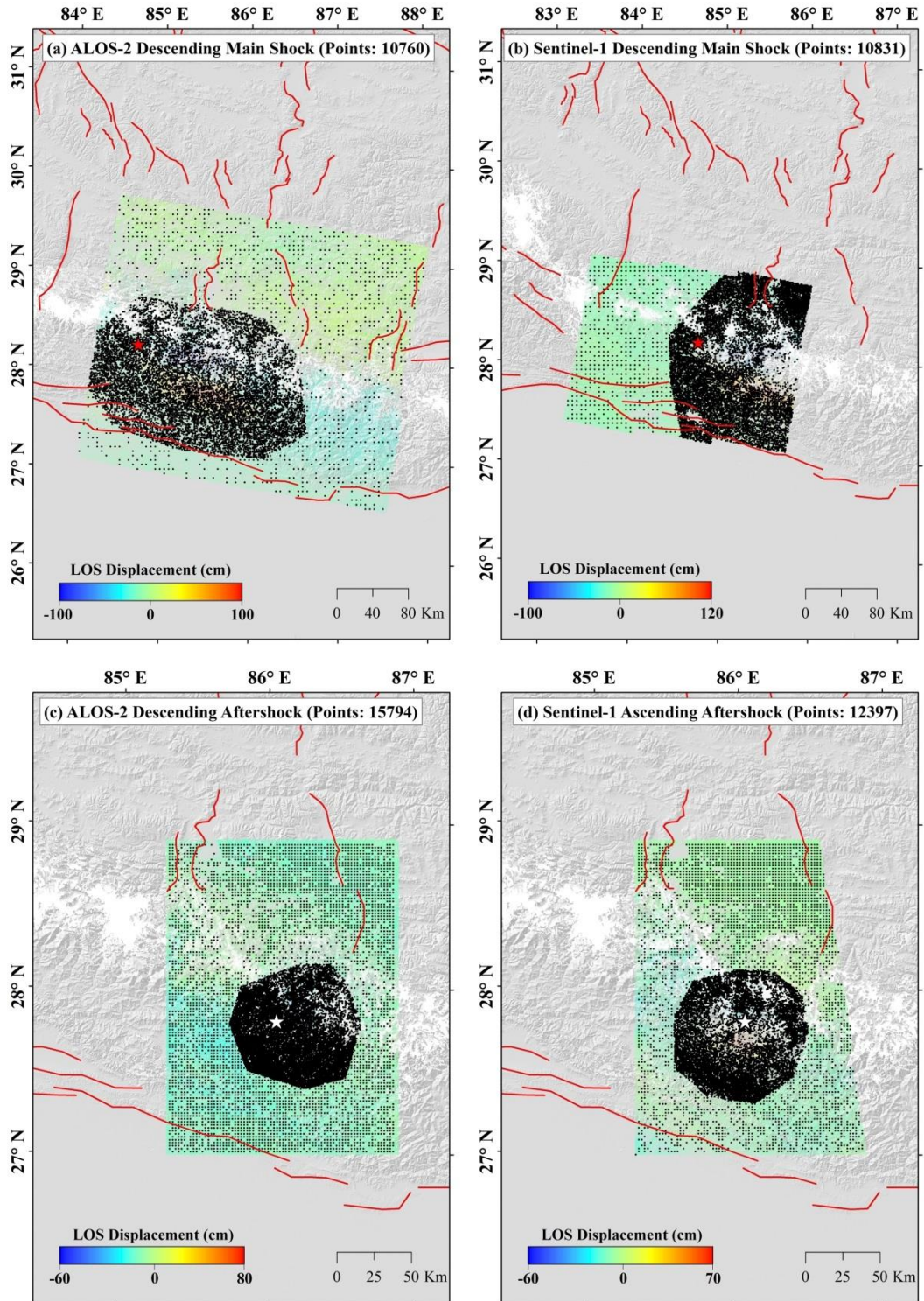


Figure 4.3 Downsamped points from four co-seismic displacement maps used in this study. (a)-(b) ALOS-2 and Sentinel-1A descending displacement maps for main shock (M_w 7.8); (c)-(d) ALOS-2 descending and Sentinel-1A ascending displacement maps for aftershock (M_w 7.2). Red lines are active faults around this region. Red star in (a)-(b) is main shock and white star in (c)-(d) is aftershock. Red and blue colours represent decrease and increase in the LOS range, respectively.

4.2.3 GPS Data

Co-seismic GPS measurements, processed by the Advanced Rapid Imaging and Analysis (ARIS) Project at Jet Propulsion Laboratory (JPL) for natural hazards are available online (http://aria-share.jpl.nasa.gov/events/20150425-Nepal_EQ/GPS/20150425Nepal_ARIA_Rapid_Offsets_v1.txt) with 9 GPS measurements in three directions and the corresponding standard deviations. We used the co-seismic measurements from 7 stations which are located between longitude 82°E and 88°E for inversion as the other two stations are too far away from the epicentre of main shock. Figure 4.4 shows co-seismic GPS measurements in horizontal and vertical directions, respectively. The nearest two GPS stations are KKN4 and NAST within 90km of the epicentre of main shock. Both maximum horizontal and vertical co-seismic displacements were recorded on KKN4, with 188.4cm and 127cm, respectively. Less than 1cm co-seismic displacements were recorded in the rest of GPS stations.

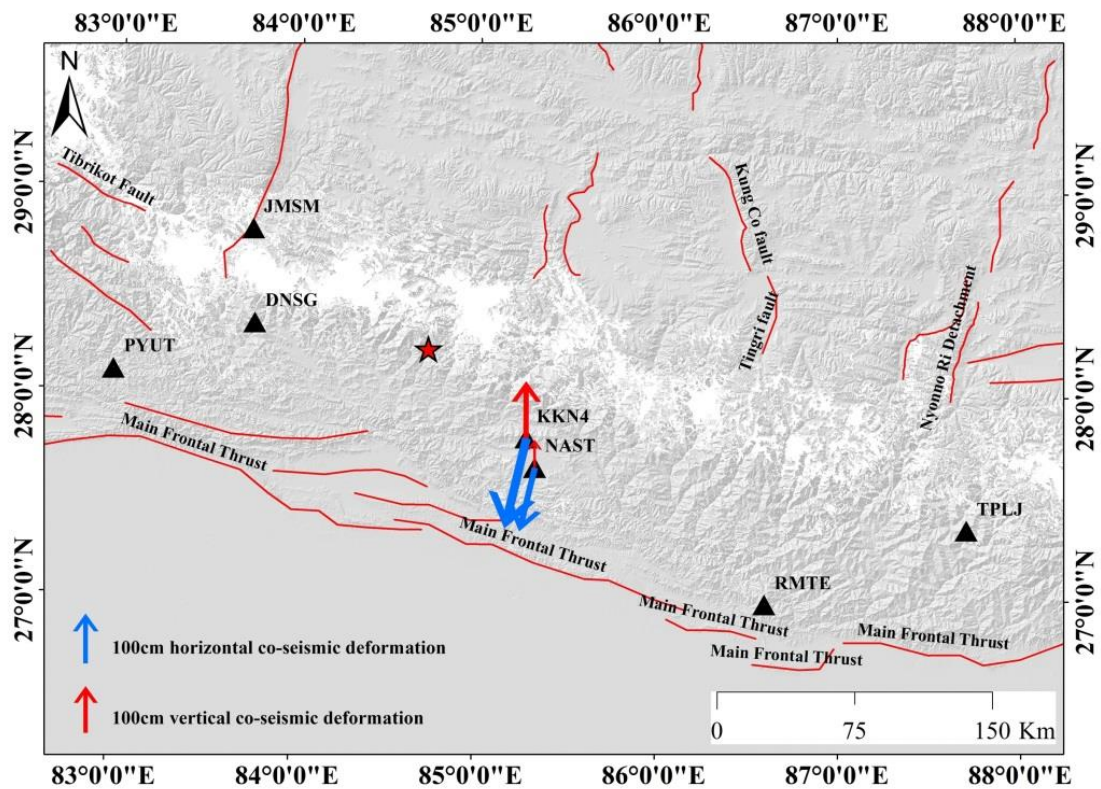


Figure 4.4 Co-seismic GPS measurements of the 25 April Nepal Earthquake. Black triangles represent the locations of GPS stations with horizontal (blue arrows) and vertical (red arrows) measurements. Red star is the epicentre of main shock. Red lines are active faults.

4.3 Modelling

All the downsampled DInSAR observations were inverted using a rectangular dislocation model in an elastic, homogeneous half-space (Okada, 1985) to describe the causative faults for the main shock and aftershock. Seven GPS measurements available with three components of co-seismic offsets were also included into the inversion for the main shock. Geodetic inversion consisted of two steps: a non-linear inversion was adopted to constrain all the fault parameters with a uniform slip model, followed by a linear inversion to infer slip distribution on the fault plane.

Non-linear inversion, a mix algorithm of Gauss-Newton iteration and gradient descent such as the Levenberg-Marquardt (LM) least-squares approach (Marquardt, 1963), was applied to constrain 9 fault parameters, namely, length, width, depth, longitude, latitude, strike, dip, rake and slip. We applied one single rectangle fault plane as the causative fault for the main shock. After adopting the initial value from GCMT, the bounds of strike, dip and rake were set as $[265^\circ, 300^\circ]$, $[5^\circ, 20^\circ]$ and $[90^\circ, 110^\circ]$ in the Non-linear search, respectively. It should be noted that only ALOS-2 ScanSAR descending data can fully cover the epicentre area and the bounds of fault location should be within the coverage of ALOS-2 descending displacement maps. As for the aftershock, a single fault plane was again adopted as being responsible for this significant event. And the bounds of strike, dip and rake were set as $[295, 315]$, $[5^\circ, 20^\circ]$ and $[95^\circ, 120^\circ]$ in the search, respectively. To retrieve the distributed slip model, a linear inversion was adopted by fixing the fault geometry estimated from non-linear inversion. The length and width of fault plane for the main shock were extended to $160\text{km} \times 100\text{km}$ to fully cover the epicentre area, but only $60\text{km} \times 45\text{km}$ for the aftershock owing to smaller epicentre area. Then the fault plane is subdivided into small patches along the strike and dip, with each of them measured $5\text{km} \times 5\text{km}$ for both of events. To avoid extremely high values or oscillations in the result, a constrained least-squares algorithm with a damping parameter can be introduced into the system, as shown in Equation (4.1):

$$\begin{bmatrix} d_{\text{DInSAR}} \\ d_{\text{GPS}} \\ 0 \end{bmatrix} = \begin{bmatrix} G \\ \varepsilon \cdot \nabla^2 \end{bmatrix} \cdot m \quad (4.1)$$

Where d_{DInSAR} and d_{GPS} are DInSAR and GPS measurement vectors, m is slip vector, G is Green's function with an extended Laplacian operator ∇^2 which is weighted by an

empirical coefficient ϵ (Wright et al., 2003). Note that GPS measurement is only available for the main shock. The empirical coefficient ϵ , also called damping factor, is determined based on the trade-off curve between the misfit of measurement and the solution roughness of slip distribution (Jónsson et al., 2002, Wright et al., 2004a). The optimal damping factor is chosen when it achieves the low misfit and small roughness at the same time (Figure 4.5). The damping factors were set to be 0.3 and 0.35 for main shock and aftershock, respectively to obtain the best-fitting results.

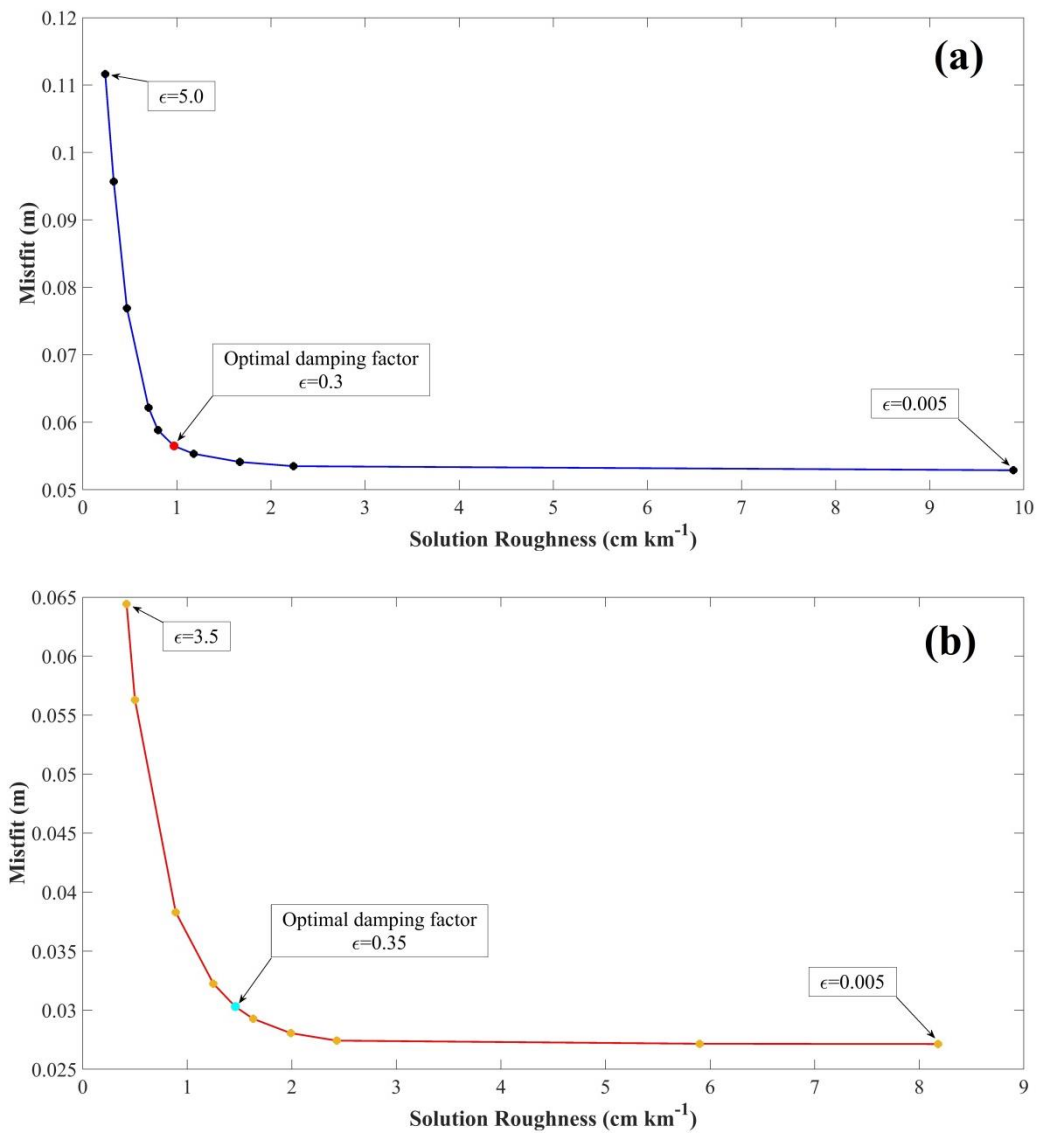


Figure 4.5 Trade-off curve between the misfit of measurement and the solution roughness for the slip distribution of (a) the main shock and (b) the major aftershock. Each dot on the curves represents one individual experiment with specific value of damping factor. The red dot in (a) and green dot in (b) are the optimal damping factor with 0.3 and 0.35, respectively.

4.4 Result

4.4.1 Modelling Result for the 25 April 2015 Mw 7.8 main shock

A joint inversion using DInSAR and GPS measurements was processed to invert the best-fitting source fault. Our optimised uniform slip model shows that the 25 April 2015 Nepal Earthquake ruptured on a thrust fault with minor right-lateral component, striking 285.9° NW-SE and dipping 7.7° NE with a depth of 8km (referring to the top edge of the fault plane). The angle of strike in our study is similar to the results from the GCMT and (Wang and Fialko, 2015) but slightly smaller than that from the USGS and (Feng et al., 2017), as shown in Table 4.2. The rake is close to the solution from the GCMT and slightly smaller than that of the USGS and (Feng et al., 2017). However, the dip from this study, seismological and previous studies all suggest a small angle with about 7° NE.

Fixing the fault geometry inverted from uniform slip model, extending the fault length and width, respectively, resulted in a distributed slip model from linear inversion. Figure 4.6 shows the slip distribution on the fault plane as well as the aftershock distribution. Most of slip occurred on the fault segments at depth between 8-14km, with a peak slip of 5.13m at a depth of 10.3km. The slip under the city of Kathmandu was up to 3m, which brought serious damage to the capital of Nepal. The slip pattern is similar with the displacement pattern observed from DInSAR, located around the middle of the main shock and the Mw 7.2 aftershock. The estimated fault trace intersecting with the surface in our source model is close to the surface trace of MFT, indicating a good agreement between these two faults. The total inferred seismic moment was calculated at 5.87×10^{20} Nm, equivalent to a moment magnitude of Mw 7.75, which is consistent with the results of the USGS and (Wang and Fialko, 2015) but slightly smaller than the GCMT (Mw 7.9) and (Feng et al., 2017) (Mw 7.85). Also, most of aftershocks located around the source plane (Figure 4.6(b)), suggesting consistence between fault geometry and aftershock distribution.

Table 4.2 Fault parameters of the 25 April 2015 M_w 7.8 Nepal Earthquake from seismology and geodetic inversion

Source	Length (km)	Width (km)	Strike ($^{\circ}$)	Dip ($^{\circ}$)	Lon ($^{\circ}$)	Lat ($^{\circ}$)	Depth (km)	Rake ($^{\circ}$)	Slip (m)	Seismic Moment (10^{20} Nm)	M_w	Data
USGS			290.0	7.0	84.731	28.731	8.2	101.0		6.62	7.80	
GCMT			287.0	6.0	85.330	27.910	12.0	96.0		8.39	7.90	
NSC/RSC					84.750	28.240					7.60	
(Wang and Fialko, 2015)	150.0		285.0	7.0					5.80	6.08	7.79	A2, GPS
(Feng et al., 2017)	180.0	92.0	290.0	6.0	85.392 ^a	27.917 ^a	9.1 ^a	102.3	~6.0	7.80	7.84	A2, S1A, RS2 and GPS
Uniform Slip Model	84.9	35.3	285.9	7.7	85.351 ^a	27.901 ^a	8.0 ^b	97.8	4.20	5.51	7.70	A2, S1A, GPS
Distribution Slip Model	160.0	100.0	285.9	7.7	85.377 ^a	27.984 ^a	5.0 ^b	97.8	5.12	5.87	7.75	A2, S1A, GPS

A2, S1A and RS2 are ALOS-2, Sentinel-1A and RADARSAT-2, respectively

^a the location refers to the centre of the fault plane projected to the surface; ^b the depth refers to the top centre of the fault plane

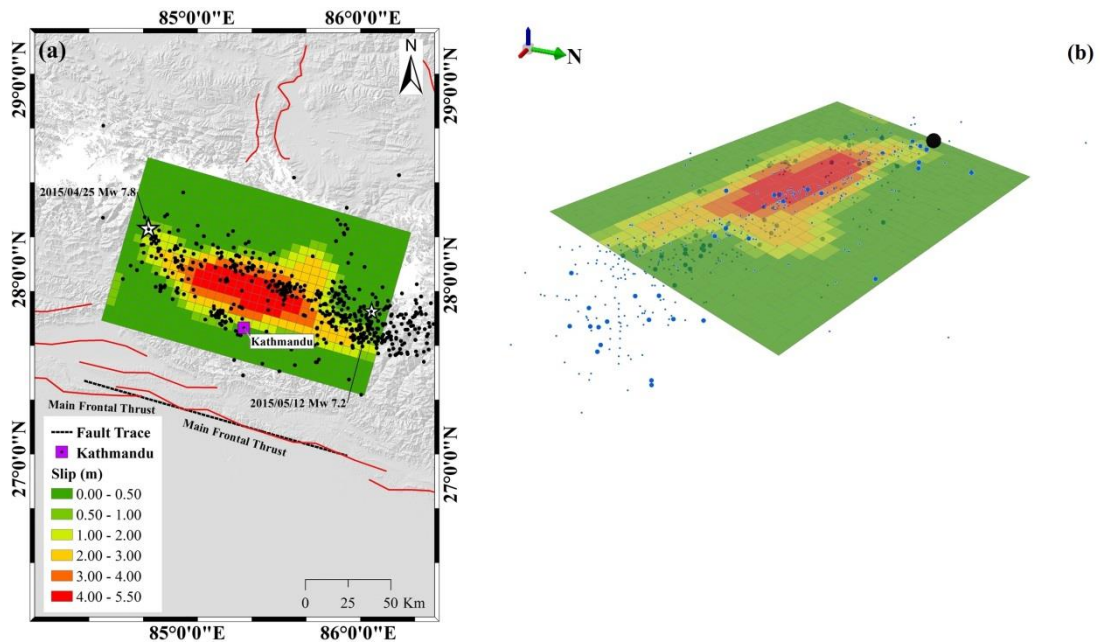


Figure 4.6 Slip distribution and aftershock distribution of the 25 April 2015 M_w 7.8 main shock, 2D view of surface projection (a) and the corresponding 3D view (b). The white star in (a) is main shock, corresponding to the black sphere in (b). Blue square represents the city of Kathmandu. Black dashed line in (a) is fault trace intersected with the surface. Black dots in (a) are aftershocks, corresponding to the blue dots in (b). Red lines are active faults.

The residual from DInSAR misfit analysis between observed and modelled data for the main shock as shown in Figure 4.7. The observed data were well reproduced for the most of the areas. The root mean square error (RMSE) values are 5.5cm and 3.2cm for the ALOS-2 ScanSAR descending and Sentinel-1A descending pairs, respectively. The residual deformation is probably caused by post-seismic deformation or secondary co-seismic hazards. Also, the misfit between GPS observed and modelled data in horizontal and vertical directions, respectively, as shown in Figure 4.8. The GPS modelled data fit observed data considerably, with overall RMSE of 2.9cm.

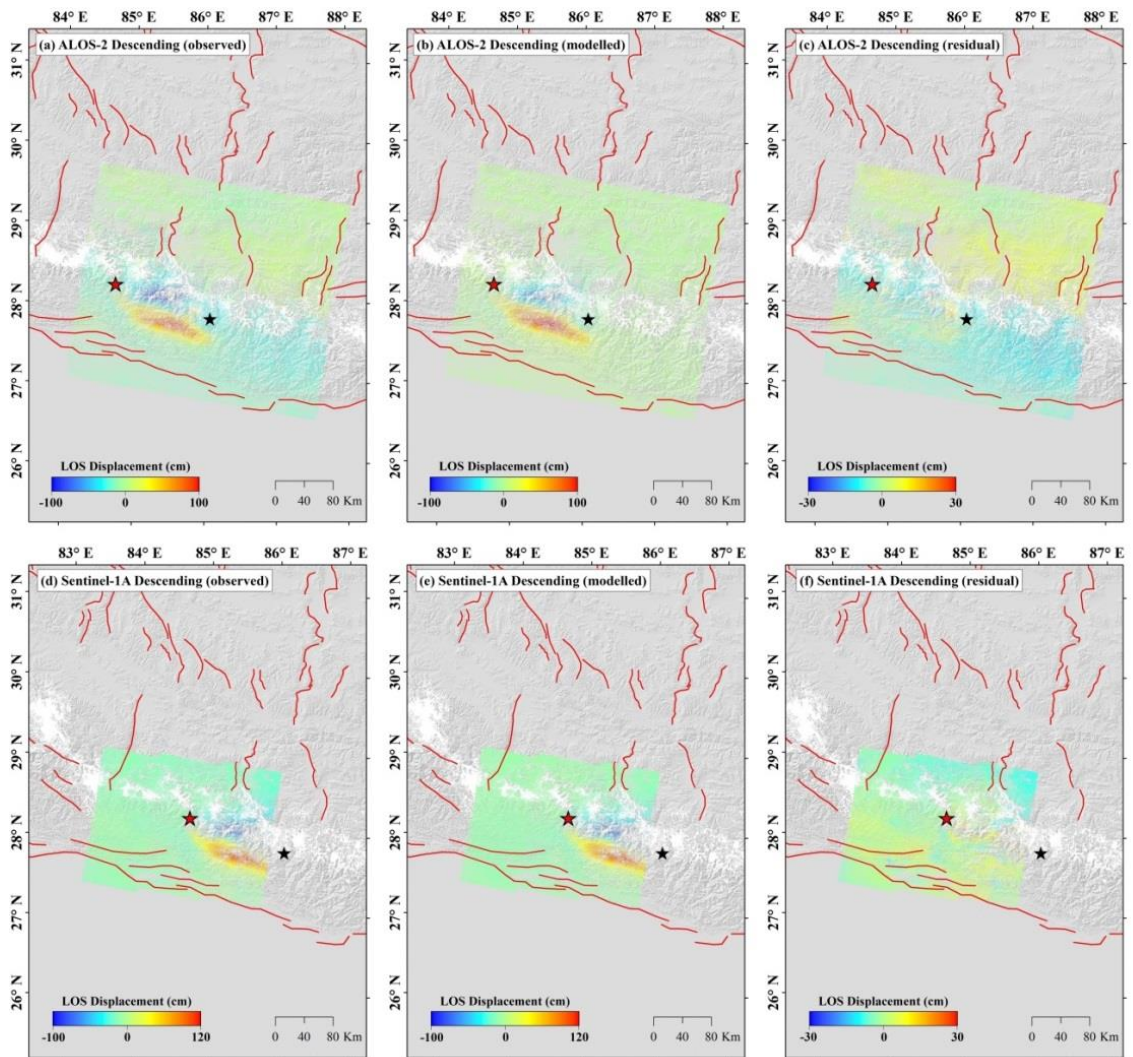


Figure 4.7 DInSAR misfit analysis for the 25 April 2015 M_w 7.8 main shock. Observed, modelled and residual data are ALOS-2 ScanSAR descending (a-c) and Sentinel-1A descending (d-f), respectively. Red star is main shock (M_w 7.8) and black star is aftershock (M_w 7.2). Red lines are active faults.

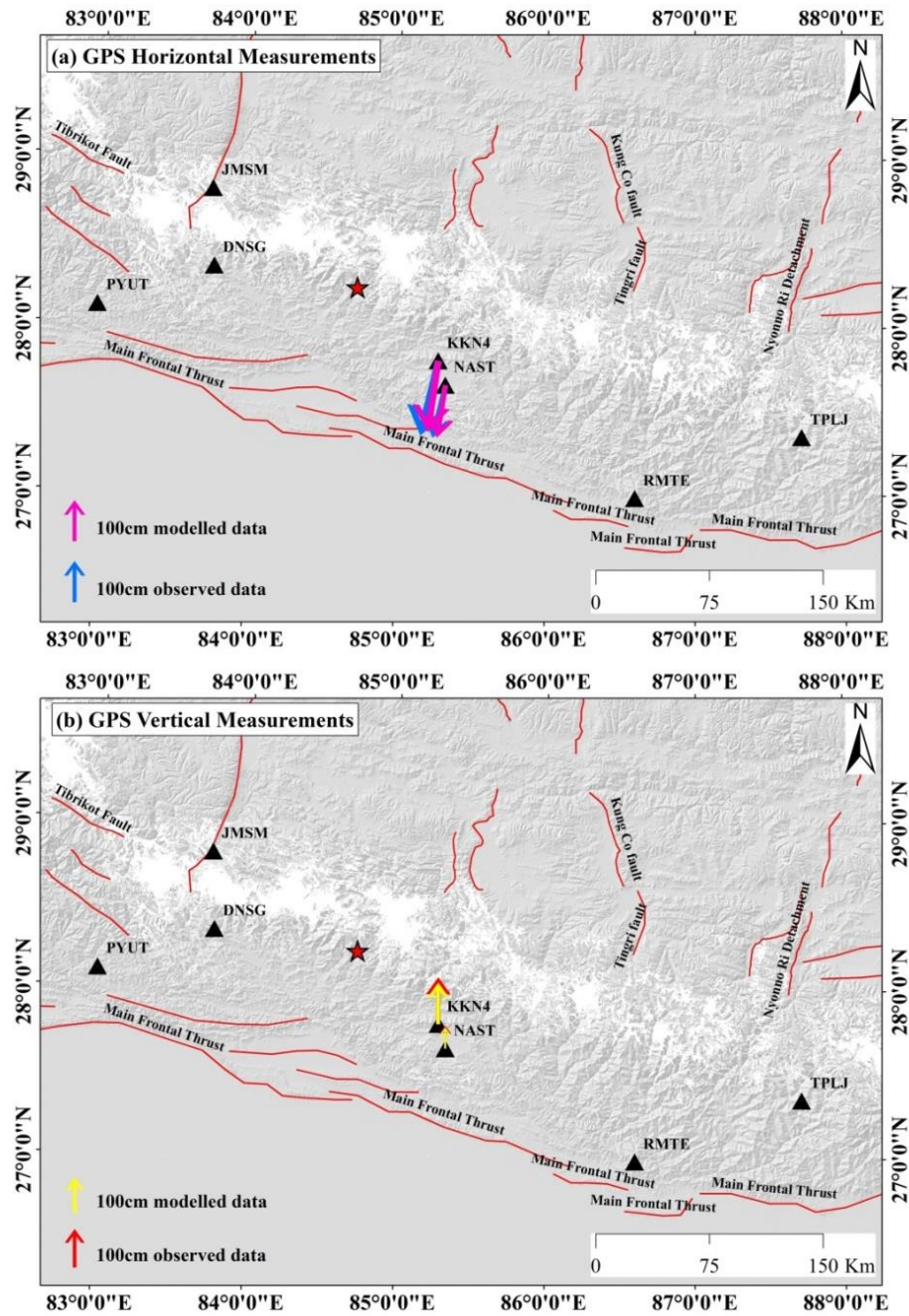


Figure 4.8 GPS (a) horizontal observed data (blue arrow) and modelled data (violet arrow), as well as (b) vertical observed data (red arrow) and modelled data (yellow arrow). The red star is main shock and black triangles are locations of GPS stations. Red lines are active faults.

4.4.2 Modelling Result for the 12 May 2015 Mw 7.2 aftershock

The fault parameters of the 12 May 2015 Mw 7.2 aftershock were inverted using ALOS-2 descending and Sentinel-1A ascending data. The best-fitting uniform slip model inverted from non-linear inversion shows that the aftershock occurred on a reverse fault

with slightly large right-lateral component, with a strike of 303.0° and a dip of about 13° (Table 4.3). The initial optimised model from non-linear inversion suggests a smaller strike angle with just 287° . However, we fixed the strike to be 303° estimated from the USGS to obtain a fault model with a smaller dip angle. The dip angle in our study is slightly higher than the results of the USGS, GCMT and (Feng et al., 2017). The angle of strike, dip and rake are all larger than those from the main shock, suggesting this event ruptured on a different fault plane. Then fixing the fault geometry and extending the fault plane to $60\text{km}\times 45\text{km}$ (length and width), slip distribution for this event is inverted based on linear inversion, as shown in Figure 4.9. Most of slip concentrated at depth of 8-12km, with a maximum slip of 4.51m at a depth of 10.0km where the peak slip of the main shock was identified. The concentrated slip is much closer to the surface than the main shock but no surface rupture was observed. And the fault plane of this major aftershock is located on the eastern end of the source fault of main shock. The total inferred seismic moment was estimated at $4.87\times 10^{19}\text{Nm}$, equivalent to a moment magnitude of $M_w 7.17$, which is similar with the results of the USGS, GCMT and (Feng et al., 2017).

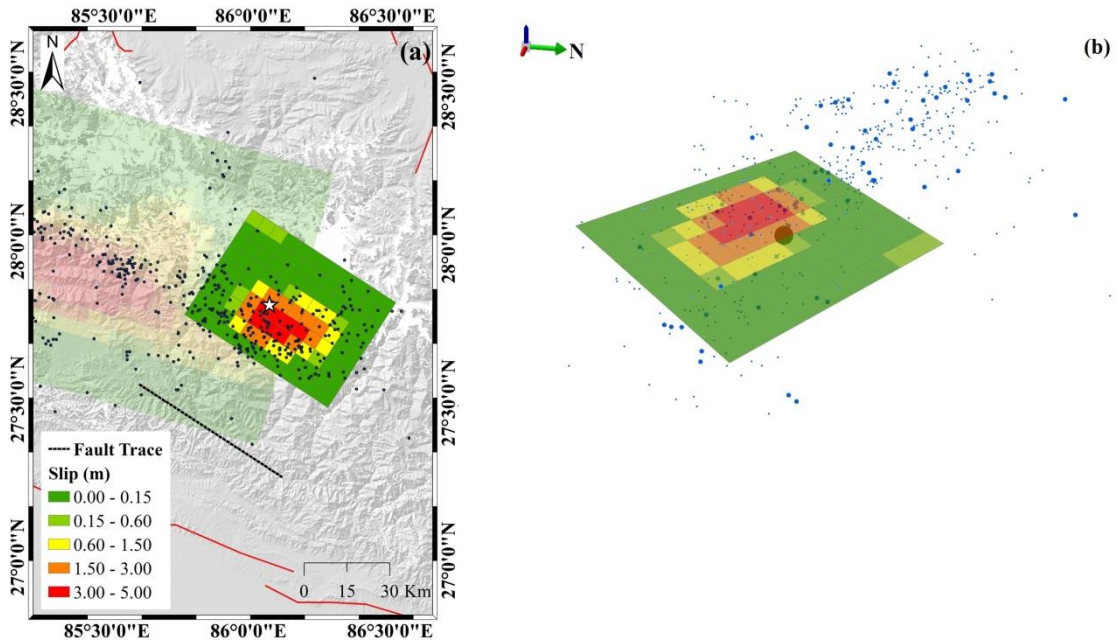


Figure 4.9 Slip distribution of 12 May 2015 $M_w 7.2$ aftershock, 2D view of surface projection of fault plane (a) and the corresponding 3D view (b). White star in (a) is the epicentre of aftershock ($M_w 7.2$), corresponding to the black sphere in (b). Black dashed line in (a) is fault trace intersected with the surface. Black dots in (a) are aftershocks, corresponding to the blue dots in (b). Red lines are active faults.

Table 4.3 Fault parameters of the 12 May 2015 aftershock from seismology and geodetic inversion

Source	Length (km)	Width (km)	Strike (°)	Dip (°)	Lon (°)	Lat (°)	Depth (km)	Rake (°)	Slip (m)	Seismic Moment (10^{19} Nm)	M_w	Data
USGS			303.0	9.0	86.066	27.809	15.0	110.0		9.89	7.20	
GCMT			307.0	11.0	86.080	27.670	12.0	117.0		8.84	7.20	
(Feng et al., 2017)	26.9	17.2	303.0	10.0	86.117 ^a	27.757 ^a	11.6 ^a	113.0	~6.0		7.20	A2, S1A and RS2
Uniform Slip Model	25.4	16.1	303.0	12.9	86.107 ^a	27.751 ^a	8.6 ^b	116.3	3.7	4.50	7.12	A2 and S1A
Distribution Slip Model	60.0	45.0	303.0	12.9	86.139 ^a	27.795 ^a	6.7 ^b	116.3	4.5	4.87	7.17	A2 and S1A

A2, S1A and RS2 are ALOS-2, Sentinel-1A and RADARSAT-2, respectively

^a the location refers to the centre of the fault plane projected to the surface; ^b the depth refers to the top centre of the fault plane

The residual from DInSAR misfit analysis between observed and modelled data for the aftershock (M_w 7.2), as shown in Figure 4.10. The modelled data fits the observed data well around the epicentre area but with slightly high residual in the far field. The root mean square error (RMSE) values are 3.2cm and 2.6cm for the ALOS-2 descending and Sentinel-1A ascending pairs, respectively. The residual is likely due to post-seismic deformation or secondary hazards caused by the main shock.

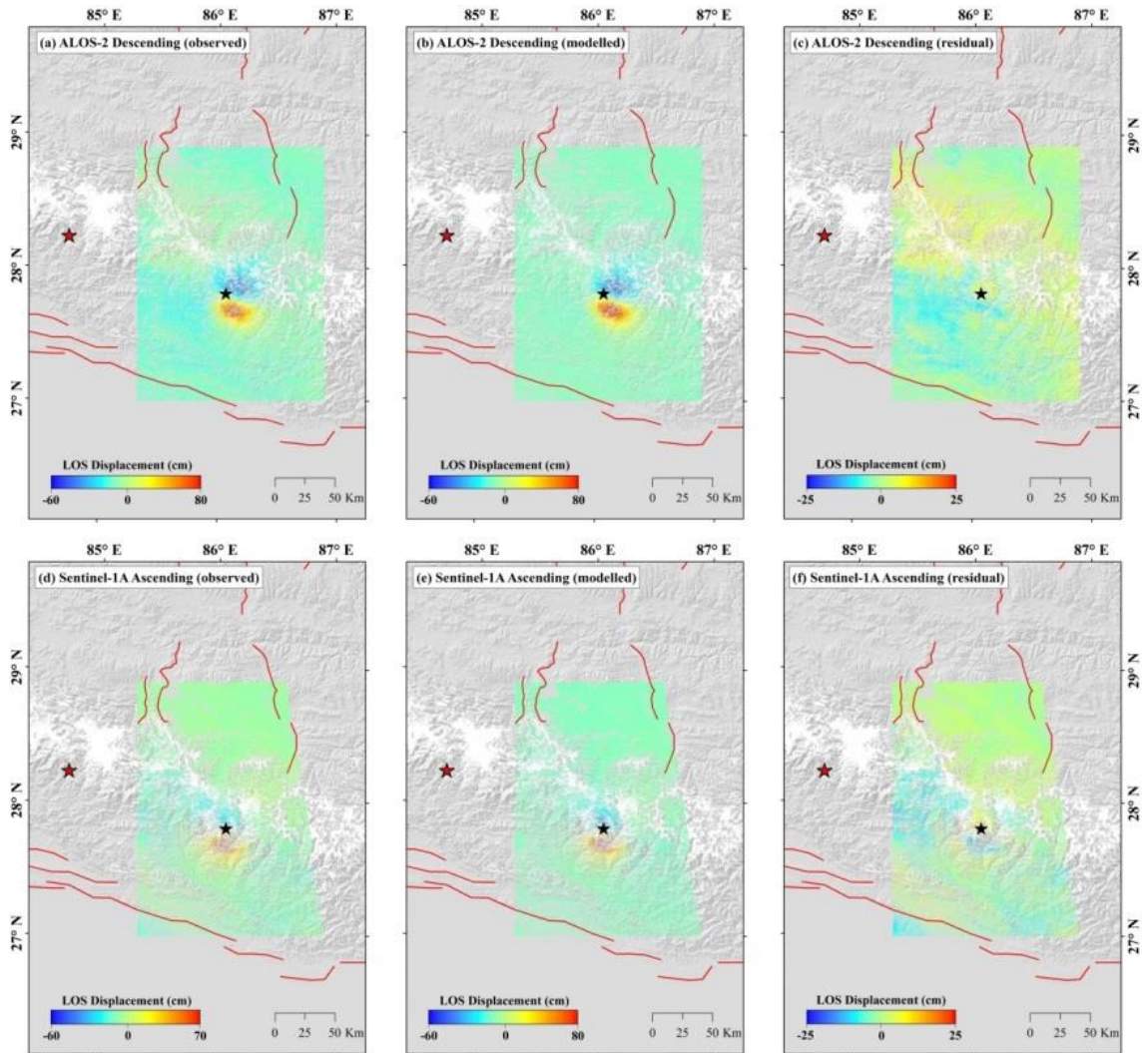


Figure 4.10 DInSAR misfit analysis for the 12 May 2015 M_w 7.2 aftershock. Observed, modelled and residual data are ALOS-2 ScanSAR descending (a-c) and Sentinel-1A ascending (d-f), respectively. Red star is epicentre of main shock (M_w 7.8) and black star is the epicentre of aftershock (M_w 7.2) from USGS. Red lines are active faults.

4.5 Discussion

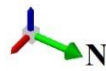
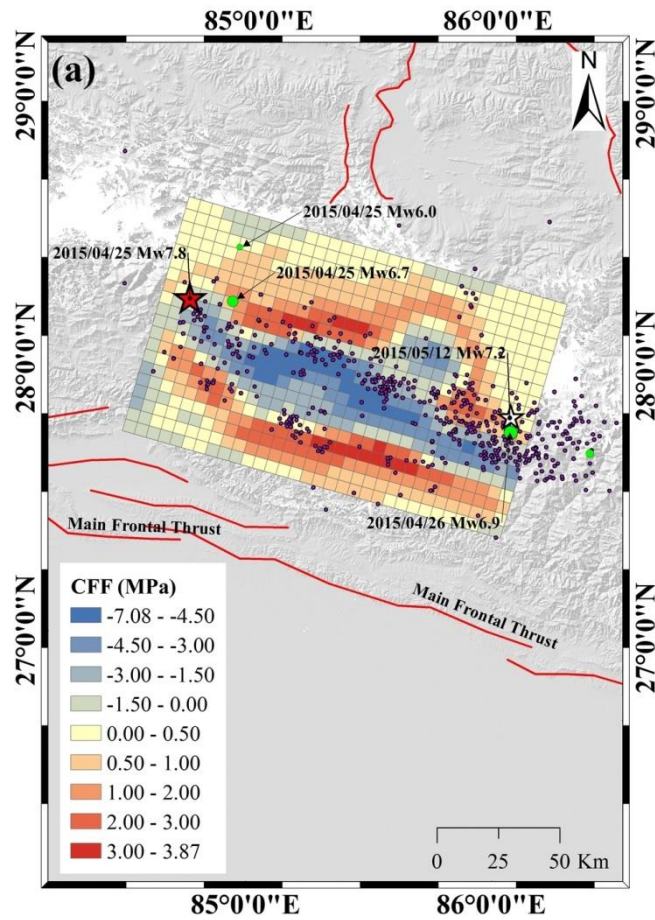
4.5.1 Coulomb Stress Change Analysis for the Mw 7.8 main shock

A co-seismic slip caused by large earthquake could lead to stress change on its source fault or the neighbouring active faults, which probably triggered further failure of the faults. To estimate the stress change induced by the 2015 Mw 7.8 main shock, we adopted the inferred distributed slip model as the source fault, and calculate the stress change on the fault plane itself using a Coulomb Failure Function (Harris, 1998). Based on Coulomb Failure Function, the stress change on the specific receiver fault is shown as Equation (4.2):

$$\Delta CFF = \Delta\tau + \mu \cdot (\Delta\sigma_n - \beta \cdot T / 3) \quad (4.2)$$

Where $\Delta\tau$ is the shear stress change, μ is the friction coefficient, $\Delta\sigma_n$ is the normal stress change, β is the Skempton's coefficient and T is the stress tensor trace. It is noted that negative Coulomb stress change represents stress is decreasing, suggesting the risk of the failure is reducing. Positive Coulomb stress change indicates that the stress is increasing, which could further trigger earthquakes in the same location. We set the friction coefficient μ and shear modulus to be 0.4 and 3.0×10^{10} N/m, respectively. Figure 4.11 shows the stress change on the fault plane of the main shock in 2D and 3D views. The maximum stress increase is 3.87MPa at a depth of 7km, and the peak stress decrease is -7.08MPa at a depth of 10.3km. The fault segments with stress increase mainly located at depth ranging from 5-8km and 12-16km, with high loaded stress areas (≥ 1.0 MPa) up to 3450km^2 . Most of the aftershocks occurred on the fault segments with positive stress change. In addition, the segments with stress decrease (negative stress change) areas were basically identified at the middle of the fault plane where the main shock occurred. Therefore, the locations of stress increase areas are in good agreement with the aftershock distribution.

We also found that the Mw 7.2 event occurred in the areas of stress increase in the eastern end of source fault. In addition, four aftershocks ($6.0 \leq M_w < 7.0$) were found at the eastern end and the west of the fault plane, i.e. the green circles shown in Figure 4.11. Three of them, Mw 6.0 and Mw 6.7 on 25 April, and Mw 6.9 on 26 April 2015 all occurred in the segments with positive stress change, indicating that these aftershocks were promoted or triggered by the main shock.



(b)

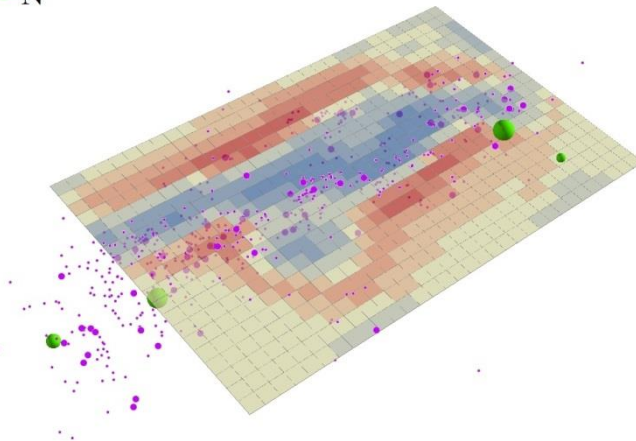
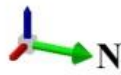
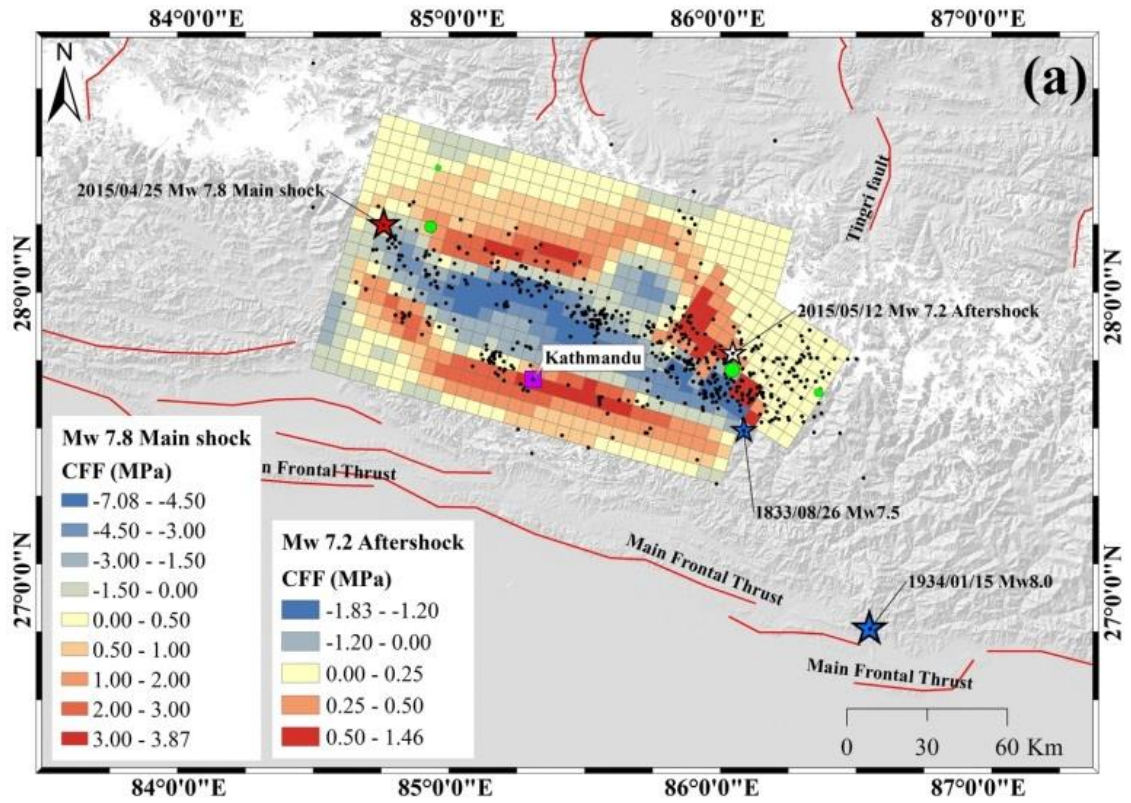


Figure 4.11 Coulomb stress change on the source fault of the 25 April 2015 M_w 7.8 main shock. (a) 2D view of stress change on the fault plane with aftershock distribution (violet dots), main shock (red star) and white star (M_w 7.2 aftershock). Red lines are active faults. (b) 3D view corresponding to (a). Green circles show the locations of aftershocks ($6.0 \leq M_w < 7.0$).

4.5.2 Triggering relationship between main shock and aftershock

Our best-fitting source model of main shock suggests that the peak slip is up to 5.1m, smaller than 5.8m of the geodetic model from (Wang and Fialko, 2015) and 6.0m of the optimized model with more co-seismic DInSAR measurements from (Feng et al., 2017). Both source models of main shock and the following M_w 7.2 aftershock reveal a reverse fault with a right-lateral component, which is consistent with the results from (Wang and Fialko, 2015) and (Feng et al., 2017). And our inverted model of the M_w 7.2 aftershock ruptured on a smaller fault plane located on the eastern end of the source fault of main shock, with a maximum slip up to 4.8m. It is worth noting that both events reach its peak slip at the similar depth, with 10.3km for the main shock and 10.0km for the M_w 7.2 aftershock.

Owing to the proximity between the M_w 7.8 main shock and the M_w 7.2 aftershock, it is essential to explore the stress transfer between these two different fault planes. To further investigate the triggering relationship between them, we adopted the distributed slip model of the M_w 7.8 main shock as source fault and the M_w 7.2 aftershock as receiver fault in the stress change estimation. Figure 4.12 shows the Coulomb stress change on the fault plane of main shock and stress transfer on the fault plane of aftershock. The fault plane of aftershock overlaps with the source plane of main shock at about 50% of its areas, as shown in Figure 4.12(a). It is also worth noting that fault plane of aftershock intersects with the source plane of main shock at depth ranging 10-13km (Figure 4.12(b)). We found that the stress changes on the fault plane of aftershock are mainly positive (stress increase) with only a few segments of stress decrease. High loaded stress areas ($\geq 0.5\text{MPa}$) on this fault are equal to 400km^2 . The peak positive stress on the fault plane of aftershock was estimated at 1.46MPa at a depth of 11km. The high amounts of positive stress changes on this fault evidenced that the 12 May 2015 M_w 7.2 aftershock was probably promoted or triggered by the 25 April 2015 M_w 7.8 main shock.



(b)

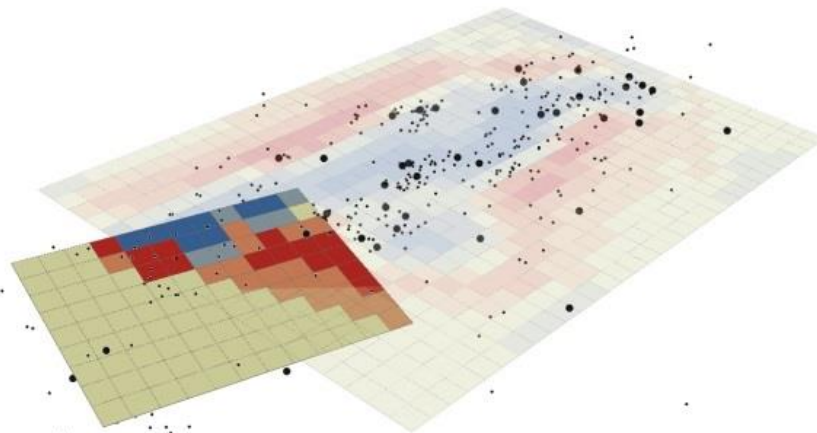


Figure 4.12 Coulomb stress change on the source fault of the M_w 7.8 main shock and the stress transfer on the M_w 7.2 aftershock. (a) 2D view, red star and white star represent the epicentres of main shock and major aftershock (M_w 7.2), respectively. Blue stars are historical earthquakes. Violet square represents the city of Kathmandu. Black dots are aftershock distribution. Red lines are active faults. (b) 3D view corresponding to (a).

Also, two major historical earthquakes, the M_w 8.0 Nepal-India border Earthquake on 15 January 1934 and the M_w 7.5 Nepal Earthquake on 26 August 1833 both occurred near or along the MFT. And the 1833 M_w 7.5 event is close to the 2015 M_w 7.8 main shock and the M_w 7.2 aftershock. It is likely that these two events occurred on the same source fault.

4.6 Conclusion

In this study, we jointly used DInSAR and GPS measurements to determine the source parameters and slip distribution for the 25 April 2015 M_w 7.8 Nepal Earthquake. The maximum DInSAR measurement for this event is up to 120cm along the LOS direction. The best-fitting source model indicate a thrust fault striking 285.9° NW-SE and dipping 7.7° NE with a slight right-lateral component. The peak slip is up to 5.12m at a depth of 10.3km. The total seismic moment is estimated at 5.87×10^{20} Nm, equivalent to a moment magnitude of M_w 7.75, slightly smaller than the solution of the USGS.

The following 12 May 2015 M_w 7.2 aftershock was also investigated using ALOS-2 ScanSAR descending and Sentinel-1A data. The inverted results of strike, dip and rake angles for the aftershock are higher than those for the main shock but both events reach its own peak slip at a similar depth (~ 10.0 km). A maximum slip of 4.87m is observed at a depth of 10.3km for the aftershock. The estimation of Coulomb stress change on the source fault of main shock demonstrated the consistence between stress increase areas and aftershock distribution. Also, we found that the M_w 7.2 event and other three major aftershocks ($6.0 \leq M_w < 7.0$) occurred on the high stress loaded areas of the source fault of main shock, which evidenced the triggering relationship between the main shock and these major aftershocks. New generation of SAR satellites (e.g. ALOS-2, Sentinel-1A/B) plays an important role in mapping and monitoring the large earthquakes owing to their larger spatial coverage and higher resolution.

Chapter 5 Finite Fault Model of the 24 August 2016 Amatrice Earthquake (Central Italy) Inferred from DInSAR and GPS Co-seismic Deformation

The co-seismic deformation and source model of the 24 August 2016 M_w 6.2 Amatrice Earthquake (Central Italy) are investigated by using a combined inversion of Differential Interferometric Synthetic Aperture Radar (DInSAR) and GPS measurements. In this study, the SAR images acquired by ALOS-2 (L-band) and Sentinel-1A/B (C-band) satellites from both ascending and descending tracks are used to map the co-seismic deformation caused by this event. The ground deformation measured from DInSAR is up to 30cm in the radar line-of-sight (LOS) direction and clearly shows two similar lobes of co-seismic deformation located in the NW and SE of the epicentre area. Firstly, the source parameters are estimated by a non-linear inversion in a homogeneous elastic half-space with DInSAR measurements and GPS data. Our best-fit uniform slip model shows a normal single fault with a small left-lateral component, striking $\sim 163^\circ$ NNW-SSE and dipping $\sim 46^\circ$ SW and the average rake is -79° . Then the slip distribution is inferred from linear inversion by fixing source geometry estimated from uniform slip model and dividing the fault plane into 576 patches with each of them measured $1\text{km}\times 1\text{km}$. The distributed slip model clearly shows two separate asperities on the north and south of the fault plane, which is in accordance with the deformation pattern measured from DInSAR. The maximum slip reaches 1.3m with a depth of 5km and the inferred seismic moment is 2.48×10^{18} Nm, corresponding to a magnitude of M_w 6.2, which is in agreement with the seismological solution from the National Earthquake Information Centre (NEIC) under the United States Geological Survey (USGS).

5.1 Introduction

On 24 August 2016, at 01:36 UTC, an M_w 6.2 earthquake struck central Italy, causing severe damage over a large area and about 300 casualties between the towns of Norcia and Amatrice and surroundings. The town of Amatrice suffered the most severe damage due to the vulnerability of local buildings and site amplification from basin (Piccardi et al., 2016). The overall geological setting of the affected region is shown in Figure 5.1.

The main shock is located on the central Apennines mountain belt which is the most seismically active zone in Italy (Pizzi and Galadini, 2009), with its epicentre at (42.723°N, 13.188°E) according to the USGS, about 45km north of L'Aquila which suffered an M_w 6.3 quake in 2009 (Atzori et al., 2009). And the hypocentre is located at a depth of about 8km, along the pre-existing Mt. Vettore-Mt. Bove Fault System (VBFS) and Laga Mountains Fault System (LMFS) striking in the NNW-SSE direction. The main shock was followed by a relative large aftershock with M_w 5.3, located about 15km from the NW of the main shock. Figure 5.1 also presents the aftershocks distribution (yellow circles) which is above M_w 2.0 recorded until 15 September 2016, and the spatial coverage of SAR images from ALOS-2 and Sentinel-1A/B. The epicentre area is well covered by SAR images both in the ascending and descending tracks. The aftershocks covered a large area with a 30km strike along SSE to NNW and about a width of 10km to 15km. On 26 October 2016, another major shock (M_w 5.9) occurred at about 30km northwest of the Amatrice Earthquake, and a few days later, another earthquake (M_w 6.6) occurred on 30 October 2016, located just between the former two shocks, as shown in Figure 5.1 (red stars).

Many researchers have investigated the source model of the Amatrice Earthquake using geodetic data and seismological data. (Tinti et al., 2016) presented the source model by inverting the strong motion data. (Cheloni et al., 2016) used continuous Global Positioning System (GPS) measurements to determine the fault geometry and co-seismic slip. (Lavecchia et al., 2016) used co-seismic DInSAR measurements to determine both double-fault model and single-fault model. Co-seismic GPS (105 stations) and DInSAR measurements are used to optimized the fault geometry of the Amatrice Earthquake by (Huang et al., 2017a). (Liu et al., 2017) jointly inverted data set of near-field strong motion, teleseismic and static GPS displacements to determine the rupture features of this event. (Cheloni et al., 2017) determined the source parameters for the Amatrice Earthquake by investigating geodetic data set of InSAR and GPS measurements (58 stations). (Xu et al., 2017) used joint inversion of InSAR and full set of GPS (128 stations) measurements to investigate the source parameters. The results of source parameters for each study are shown in Table 5.1.

In this study, we mainly investigated the co-seismic deformation and source model of the 2016 Amatrice Earthquake by using the combination of Differential Interferometric Synthetic Aperture Radar (DInSAR) observations from ALOS-2 and Sentinel-1A/B and

co-seismic GPS measurements. Based on the elastic fault model (Okada, 1985), the fault parameters and slip distribution were inverted for the Amatrice Earthquake. Our overall strategies are similar with the published work using DInSAR and GPS (Lavecchia et al., 2016, Huang et al., 2017a, Cheloni et al., 2017, Xu et al., 2017), but we obtained a different result of stress change from the Coulomb stress change analysis. Finally, we demonstrated that the combination of DInSAR and GPS measurements is an effective tool for co-seismic deformation monitoring and earthquake source modelling.

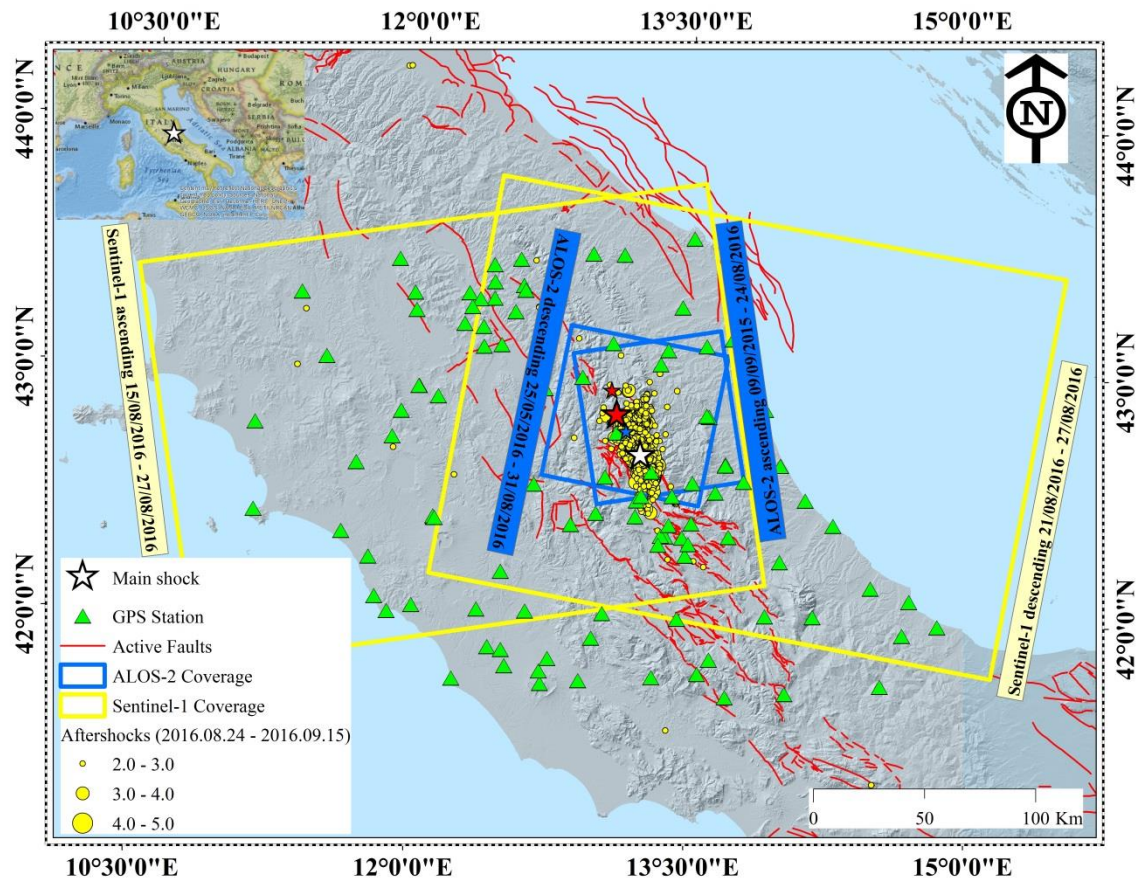


Figure 5.1 Geographical setting with main shock (white star), aftershocks (yellow circles), active faults (red lines) from INGV, GPS stations (green triangles) and spatial coverage of SAR images (blue rectangles for ALOS-2 images and yellow rectangles for Sentinel-1A/B images). The blue star represents the significant Mw 5.3 aftershock. The red stars represent the October 26 and October 30 main shocks. The yellow scaled circles present the locations of aftershocks ($M_w > 2.0$) from 24/08/2016 to 15/09/2016 collected from Institute of Geophysics and Volcanology (INGV) National Earthquake Centre [<http://cnt.rm.ingv.it/tdmt>].

Table 5.1 Source parameters of the 24 August 2016 Amatrice Earthquake

Source	Length (km)	Width (km)	Depth (km)	Strike (°)	Dip (°)	Lon (°)	Lat (°)	Rake (°)	Slip (m)	Seismic Moment (10^{18} Nm)	M _w	Data
USGS			4.4	165.0	49.0	13.188	42.723	-78.0		2.45	6.2	
GCMT			12.0	145.0	38.0	13.220	42.640	-101.0		2.48	6.2	
INGV			5.0	155.0	41.0	13.220	42.710	-93.0		1.07	6.0	
(Tinti et al., 2016)	26.0	12.0	7.3	156.0	50.0	13.230	42.700	-120.0~ -70.0		1.60	6.1	Strong motion
(Cheloni et al., 2016)	20.4	5.0	2.8	161.5	45.6	13.255	42.745	-78.0	0.70	2.13	6.2	GPS
(Lavecchia et al., 2016)	38.0	14.0	0.5	161.0	46.0	13.237	42.728	-92.0	0.60	2.50	6.2	A2, S1
(Huang et al., 2017a)	39.0	15.0		167.0	46.0			-73.0		1.88	6.2	A2, S1, GPS
(Liu et al., 2017)	28.8	16.0	4.4	155.0	46.0	13.234	42.698			2.30	6.2	GPS, strong motion, teleseismic waveforms

(Cheloni et al., 2017)					50.0/ 40.0					2.12	6.2	A2, S1, GPS
(Xu et al., 2017)												
Uniform Slip Model	18.6	5.9	2.7	164.0	43.6	13.259	42.735	-68.2	0.63	2.07	6.2	A2, S1, GPS
(Xu et al., 2017)												
Distributed Slip Model	36.0	18.0	2.7	164.0	43.6	13.259	42.735	-89.7	1.26	2.16	6.2	A2, S1, GPS
Uniform Slip Model	19.0	5.4	1.5**	163.4	46.1	13.237*	42.730*	-78.6	0.62	1.89	6.2	A2, S1, GPS
Distributed Slip Model	36.0	16.0	0.8**	163.4	46.1	13.218*	42.725*	-78.6	1.33	2.48	6.2	A2, S1, GPS

A2 and S1A represent ALOS-2 and Sentinel-1A/B, respectively.

* the location refers to the centre of the fault plane projected to the surface

** the depth refers to the top centre of the fault plane

5.2 Geodetic Data

5.2.1 SAR Data

We generated four co-seismic interferograms with two pairs of SAR images from ALOS-2 satellite operated by Japan Aerospace Exploration Agency (JAXA), and another two from Sentinel-1A/B satellite operated by European Program Copernicus from European Space Agency (ESA), both of them available in the ascending and descending tracks. Specifically, Table 5.2 shows the detailed information for each interferometric pair. The wavelengths of ALOS-2 and Sentinel-1A/B are 22.9cm and 5.6cm, respectively. It is noted that the post-seismic ALOS-2 image in the ascending track was captured immediately on the same day of main shock thanks to the emergency response of JAXA. The ascending ALOS-2 pair, though its long time delay (350 days) and relatively larger spatial baseline (198m), achieve a good level of coherence due to the L-band's high penetration in vegetation area.

Table 5.2 The processed interferometric pairs for the 2016 Amatrice Earthquake

Sensor	Orbit	Image Mode	Interferometric Pair (dd/mm/yyyy)	Track	B_{\perp} (m)	B_T (days)	θ ($^{\circ}$)
A2	ASC	SM	09/09/2015- 24/08/2016	197	198.9	350	36.6
A2	DESC	SM	25/05/2016- 31/08/2016	92	-88.2	98	32.9
S1	ASC	IWS	15/08/2016- 27/08/2016	117	-33.1	12	39.0
S1	DESC	IWS	21/08/2016- 27/08/2016	22	-79.3	6	39.0

A2 and S1A are ALOS-2 and Sentinel-1A/B, respectively. ASC and DESC are ascending and descending orbits, respectively. SM is StripMap mode and IWS is Interferometric Wide Swath (TOPS) mode. B_{\perp} is perpendicular baseline (m), B_T is temporal baseline (day), θ is incidence angle.

5.2.2 DInSAR measurements

Four interferometric pairs were processed with Two-Pass DInSAR technique (Massonnet et al., 1993) using the interferometric module of SARscape software. Note that the ascending Sentinel-1A/B interferogram is composed of two frames to fully cover the epicentral area. We processed each ascending Sentinel-1A/B frame to wrapped phase and then both of them were mosaicked to form one interferogram. The signal-to-noise ratio (SNR) of each interferogram was improved by averaging the ALOS-2 images with 3 by 8 or 6 looks and 1 by 5 looks for Sentinel-1A/B images, in range and azimuth directions respectively. Eight or six looks is applied in azimuth direction owing to different overlapping rates between master and slave images. Topographic effects were removed with the topographic phases derived from 3 arc-second Digital Elevation Model (DEM) from the Shuttle Radar Topography Mission (SRTM) (Farr et al., 2007). The interferometric noise was further reduced by using Goldstein Adaptive Filter (Goldstein and Werner, 1998), and then the interferometric phase was unwrapped by using Minimum Cost Flow algorithm (Costantini, 1998). After interferometric processing, four geocoded co-seismic displacement maps with 90m resolution can be generated by converting the unwrapped phase to deformation. Figure 5.2 shows four co-seismic deformation maps generated from the ALOS-2 and Sentinel-1A/B interferometric pairs. The ground deformation maps generated from four co-seismic interferograms show similar displacement pattern, with two similar deformation lobes in the NNW-SSE direction. The maximum negative LOS displacement was estimated at 20.5cm for ALOS-2 ascending track, 30.3cm for ALOS-2 descending track, 20.2cm for Sentinel-1 ascending track and 21.5cm for Sentinel-1 descending track, respectively, which is similar with the published results (Lavecchia et al., 2016, Huang et al., 2017a, Cheloni et al., 2017, Xu et al., 2017).

The vertical and east-west displacement components can be estimated through weighted least squares fitting by assuming the insensitive north-south displacement was negligible (Ng et al., 2011, Ng et al., 2012). The ascending and descending Sentinel-1A/B displacement maps were combined to retrieve the vertical and east-west displacement components, as shown in Figure 5.3. The westward deformation is identified in the both sides of the epicentre, with peak deformation of 10.5cm. The eastward movement is relatively smaller, with 7.8cm at most, located around and northwest of the epicentre. In contrast, the deformation pattern of vertical component is similar with the DInSAR LOS deformation pattern, suggesting that the vertical component contributes the most for this

event. There are two significant subsidence lobes around and northwest of the epicentre, with peak deformations of 20.5cm and 22.0cm, as shown in the profile plot along A-A' section (Figure. 5.3(c)).

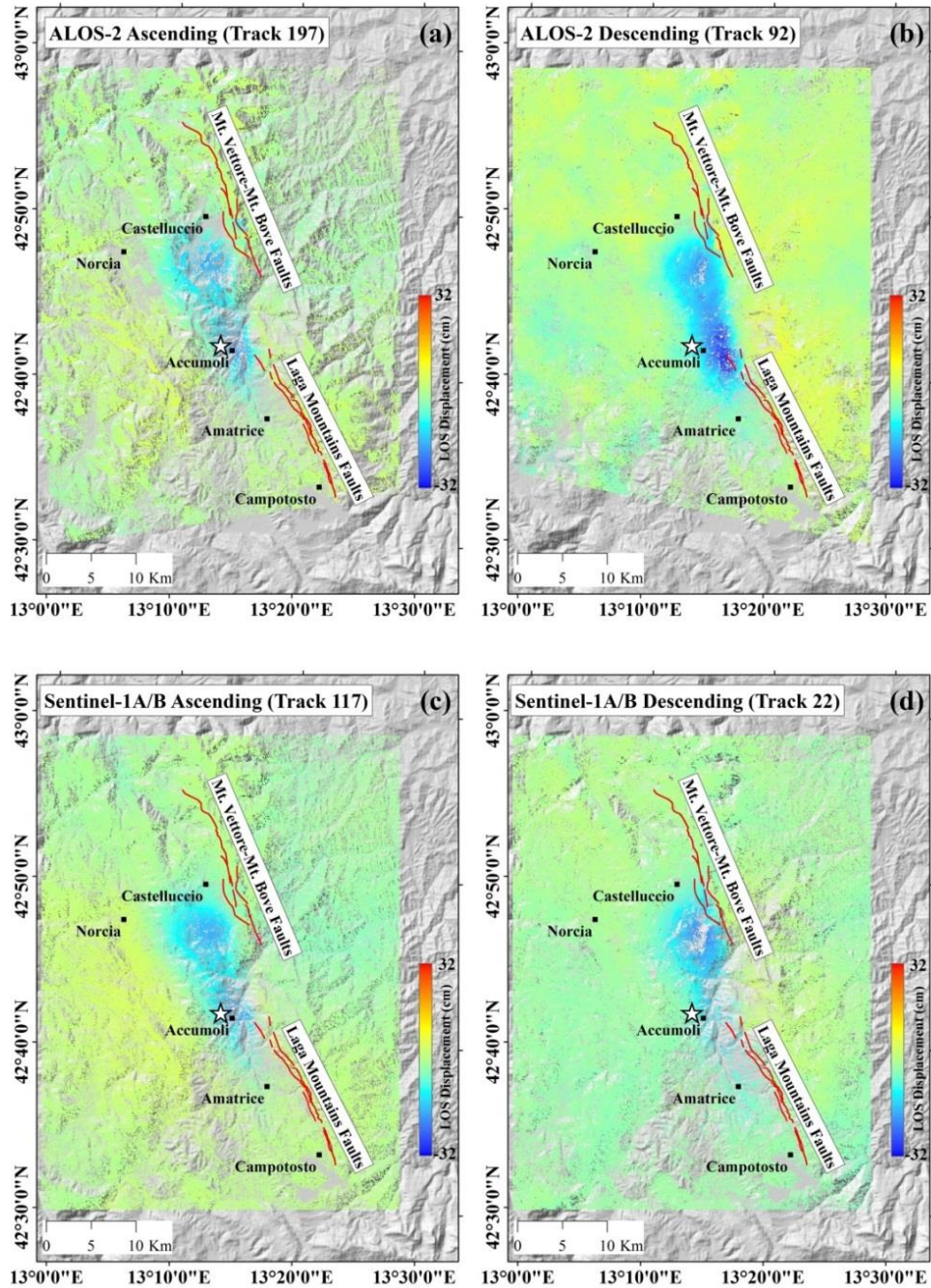


Figure 5.2 ALOS-2 and Sentinel-1A/B co-seismic deformation maps. (a) ALOS-2 ascending (Track 197); (b) ALOS-2 descending (Track 92); (c) Sentinel-1A/B ascending (Track 117); (d) Sentinel-1A/B descending (Track 22). Black squares represent the major cities. The white star is main shock and red lines are active faults.

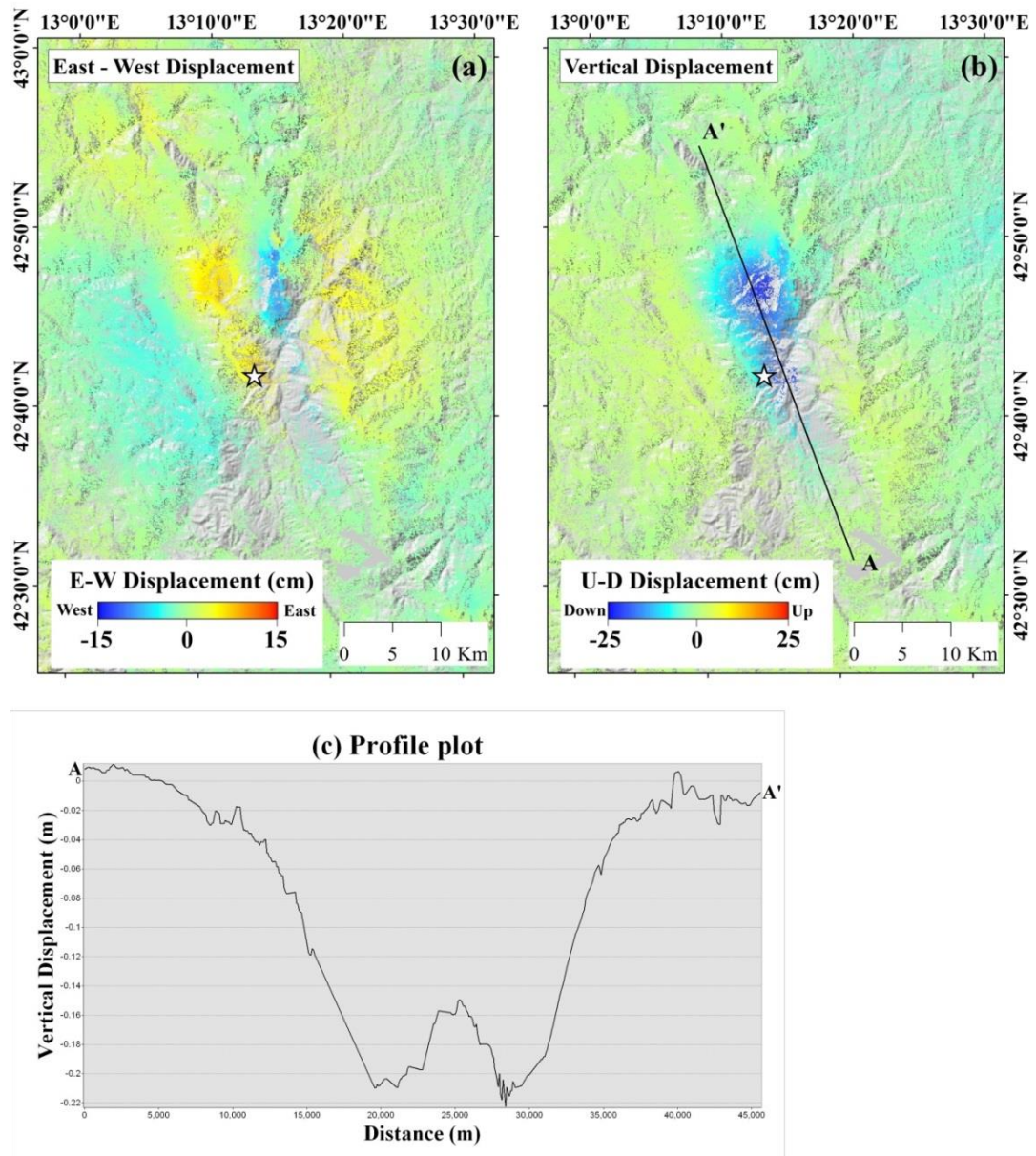


Figure 5.3 Co-seismic displacement in (a) east-west and (b) vertical directions retrieved from Sentinel-1A/B ascending and descending LOS displacement maps. The white star shows the epicentre from the USGS. (c) Profile plot along A-A' section across the areas of maximum deformation in the vertical displacement (b).

The four displacement maps include several millions data points, so it is unnecessary to use all of them. We preserve the data points in the area between latitude 42.505°N-42.975°N and longitude 12.977°E - 13.479°E. And the four displacement maps were downsampled with a regular mesh which is 500m × 500m around the deforming area and 2000m × 2000m for the rest area. A total of 7891 data points are obtained, 3480 points for ALOS-2 and 4411 points for Sentinel-1A/B, as shown in Figure 5.4.

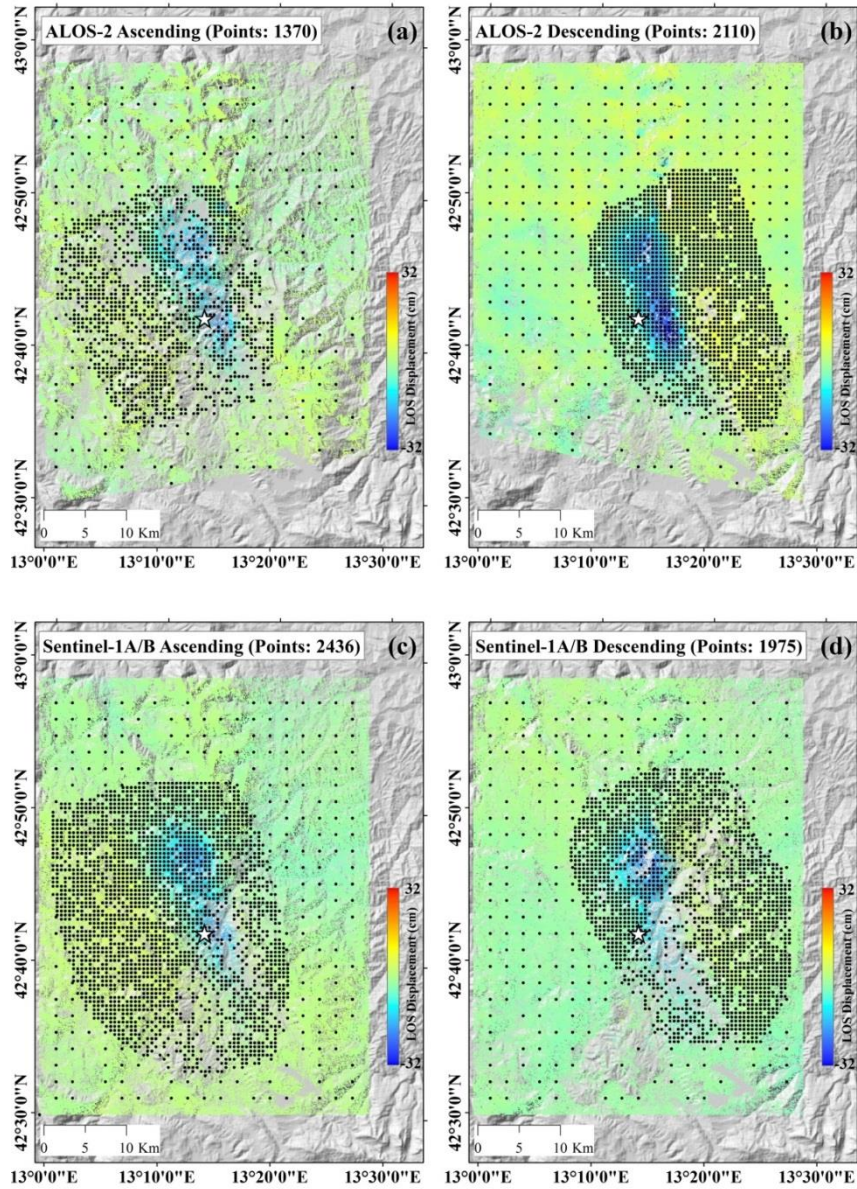


Figure 5.4 Downsampled measurement points from four co-seismic deformation maps used in this study. (a) ALOS-2 ascending (Track 197); (b) ALOS-2 descending (Track 92); (c) Sentinel-1A/B ascending (Track 117); (d) Sentinel-1A/B descending (Track 22). White star is main shock.

5.2.3 GPS Data

Co-seismic GPS measurements, collected and processed by INGV National Earthquake Center (CNT) (Cheloni et al., 2016), are available online with 106 GPS measurements in three directions (East/North/Up) and the corresponding standard deviations. These co-seismic GPS measurements are obtained from the analysis of pre- and post-seismic data from continuous GPS stations (INGV Working group "GPS Geodesy (GPS data and data

analysis center)", 2016). It should be noted that the measurement from GPS station named GUB2 is not included in the following inversion steps due to its relatively high vertical measurement in the far field (Huang et al., 2017a). Figure 5.5 shows the GPS horizontal and vertical co-seismic measurements with main shock.

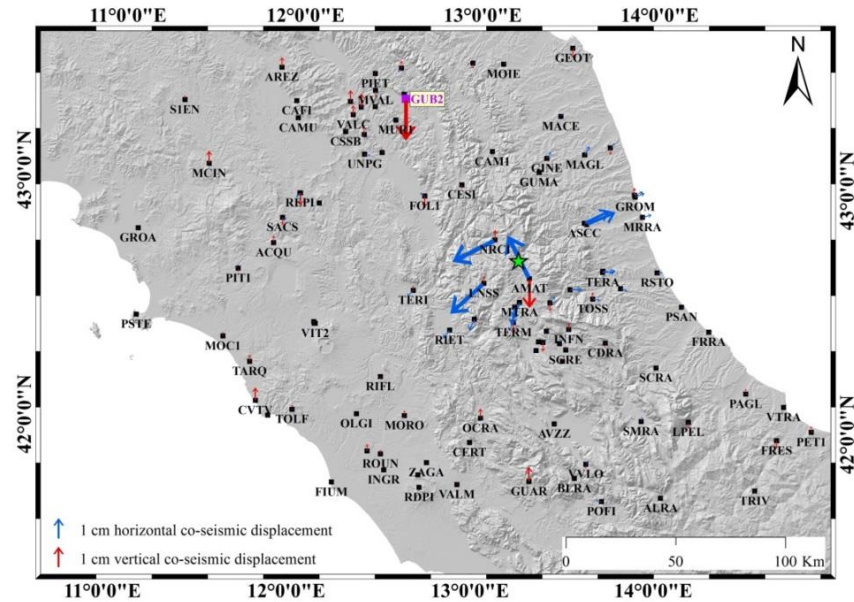


Figure 5.5 GPS horizontal (blue arrows) and vertical (red arrows) co-seismic measurements. Black squares denote the location of each GPS station. The station named GUB2 is highlighted with violet squares and label. The white star represents main shock.

5.3 Modelling

To further analyse and describe the causative fault for the main shock, we jointly invert the DInSAR and GPS measurements using a finite dislocation model in an elastic, homogeneous half-space (Okada, 1985). Basically, our geodetic modelling method consists of two steps: firstly a non-linear inversion is adopted to constrain all the fault parameters with a uniform slip model, followed by a linear inversion to infer the slip distribution on the fault plane.

Firstly a non-linear inversion, a mix algorithm of Gauss-Newton iteration and gradient descent as the Levenberg-Marquardt (LM) least-squares approach (Marquardt, 1963), is applied to constrain 9 fault parameters (namely, length, width, depth, longitude, latitude, strike, dip, rake, slip) by assuming no dilation between the hanging wall and footwall. In order to retrieve the slip distribution on the fault plane, a linear inversion is adopted by

fixing the fault geometry inverted from the non-linear inversion (Table 5.1). According to the aftershock distribution, the length and width of the fault plane are extended to 36km and 16km, respectively. Then the fault plane is subdivided into 576 patches along the strike and dip, with each of them measured 1km×1km. To avoid very high value or oscillations in the result, a damping parameter can be introduced into the system, shown as Equation (5.1):

$$\begin{bmatrix} d_{\text{DInSAR}} \\ d_{\text{GPS}} \\ 0 \end{bmatrix} = \begin{bmatrix} G \\ \mathcal{E} \cdot \nabla^2 \end{bmatrix} \cdot m \quad (5.1)$$

Where d_{DInSAR} and d_{GPS} are DInSAR and GPS measurement vectors, m is slip vector, G is Green's function with an extended Laplacian operator ∇^2 which is weighted by an empirical coefficient \mathcal{E} (Wright et al., 2003). The empirical coefficient \mathcal{E} , also called damping factor, is determined based on the trade-off curve between the measurement misfit and the roughness of the slip distribution (Jónsson et al., 2002, Wright et al., 2004a). The optimal damping factor was set to be 0.18 to obtain the best-fitting results (Figure 5.6). To increase the reliability of the source model, a non-negative least square algorithm is adopted to positively invert this system (Atzori and Salvi, 2014).

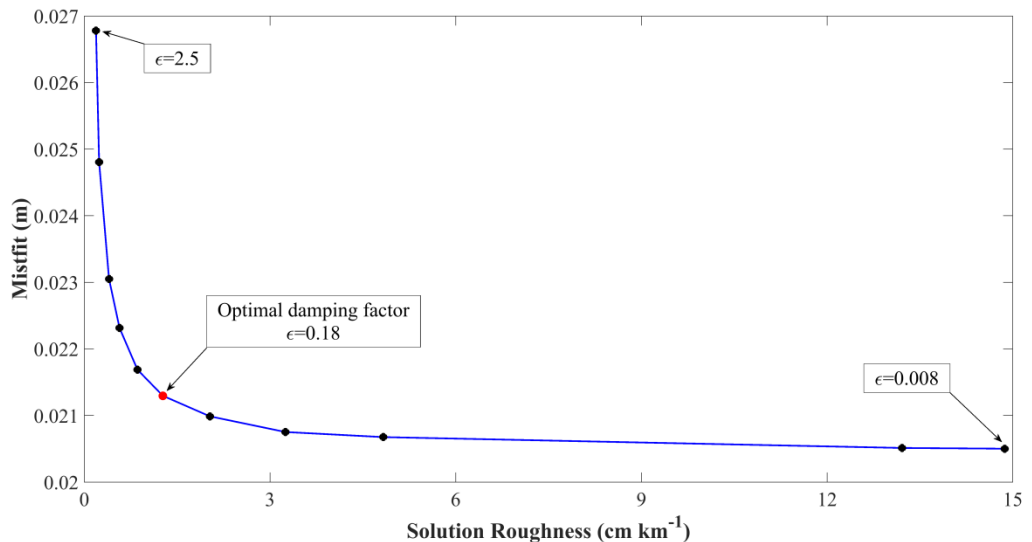


Figure 5.6 Trade-off curve between the misfit of measurement and the solution roughness for the slip distribution. Each dot on the curves represents one individual experiment with specific value of damping factor. The red dot is the optimal damping factor with 0.18.

5.4 Result

The non-linear inversion was processed with 9 fault parameters free and the best-fit source parameters from seismology, published research and our study are shown in Table 5.1. Note that both (Lavecchia et al., 2016) and (Cheloni et al., 2017) have the double-fault solution and only single-fault solution is presented for Lavecchia et al. (Lavecchia et al., 2016). The latitude and longitude in (Cheloni et al., 2017) indicate the coordinates of the centre of the top edge of the fault plane. The depth in the uniform slip model and distributed slip model is the distance between the upper edge of fault plane and the surface. The slip in the distributed slip model is the peak slip. The best-fit source parameters constrained from the non-linear inversion shows a normal single fault with a small left-lateral component, striking 163.4° NNW-SSE and dipping 46.1° SW and the average rake is -78.6° . The strike, dip and rake angle are similar to the result from U.S. Geological Survey National Earthquake Information Center (NEIC) (strike/dip/rake - $165^\circ/49^\circ/-78^\circ$). Figure 5.7(a) shows the slip distribution on the fault plane inverted from distributed slip model. The orientation and location of the fault plane are fixed from non-linear inversion, while the length and width are extended. The inferred slip distribution shows two distinct asperities on the north and south of the fault plane, which is in accordance with the deformation pattern measured from DInSAR. The maximum slip reaches up to 1.3m with a depth of 5km in the northern asperity and the peak slip in the southern part is 1.1m. Furthermore, the aftershocks presented in Figure 5.7(a, b) are located near the two slip asperities and around the fault plane, indicating a good agreement between fault geometry and aftershock distribution. Note that the top edge of the fault plane is just 800m below the surface and some of slip might reach up to the surface, which could lead to local surface ruptures in certain areas. This also can be proved by the co-seismic rupture evidence surveyed by the INGV geological survey teams (EMERGEO Group) (EMERGEO Working Group, 2016). The inferred overall seismic moment is 2.48×10^{18} Nm, corresponding to a magnitude of Mw 6.2, which is consistent with the solutions from the UGSS NEIC and the Global Centroid Moment Tensor (GCMT), but slightly larger than the INGV (Mw 6.0).

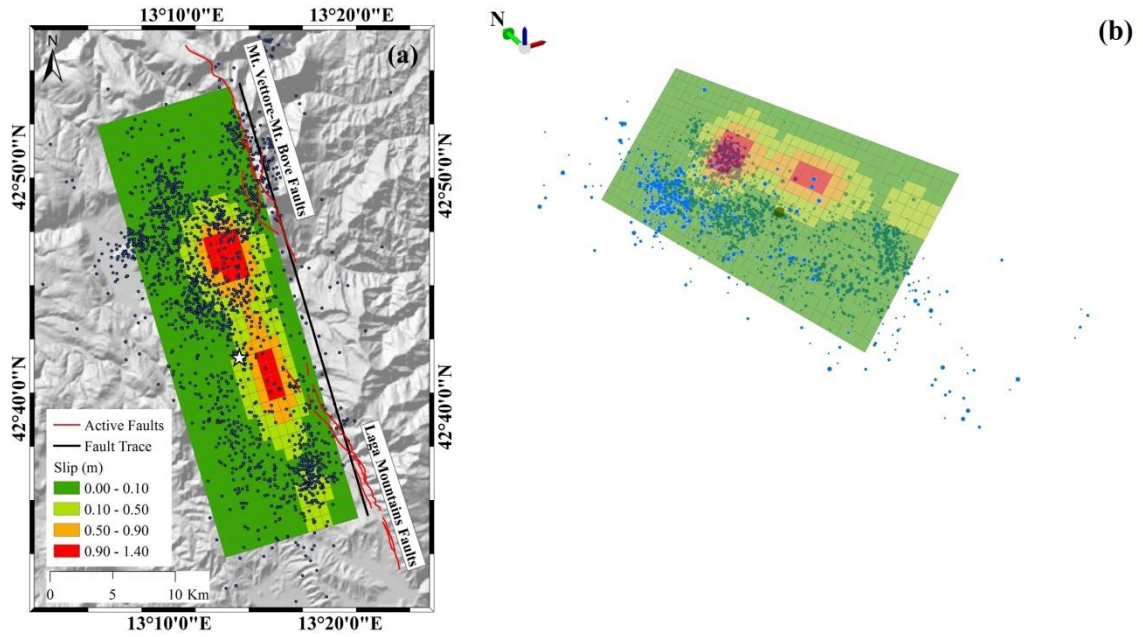


Figure 5.7 Slip distribution for the Amatrice Earthquake. (a) 2D map view of slip distribution with main shock (white star), aftershocks (blue dots), active faults (red lines) and estimated fault trace (black line). (b) 3D view of slip distribution with aftershock distribution and main shock (black sphere).

To estimate the misfit between DInSAR observations and model data, the residual data is also shown in the Figure 5.8(a-1). The RMSE estimated from residual data are 1.8cm, 2.0cm, 1.3cm and 1.5cm for ALOS-2 ascending, ALOS-2 descending, Sentinel-1A/B ascending and Sentinel-1A/B descending, respectively. We can see that the misfits for the ALOS-2 data both are higher than those from Sentinel-1A/B data possibly because ALOS-2 data (L-band) is more sensitive to ionospheric disturbances (Huang et al., 2017a). Also, the misfit and possible noise could be caused by atmospheric delay, orbital and unwrapping errors, neglected slip from major aftershocks and secondary co-seismic geological disasters (landslides and rockfalls). Also, the comparison between GPS observed and model data in horizontal and vertical directions, respectively, are shown as Figure 5.9(a, b). The GPS model data fit observed data considerably, with RMSE estimations are 1.81, 1.06 and 4.15mm for east, north and vertical directions, respectively.

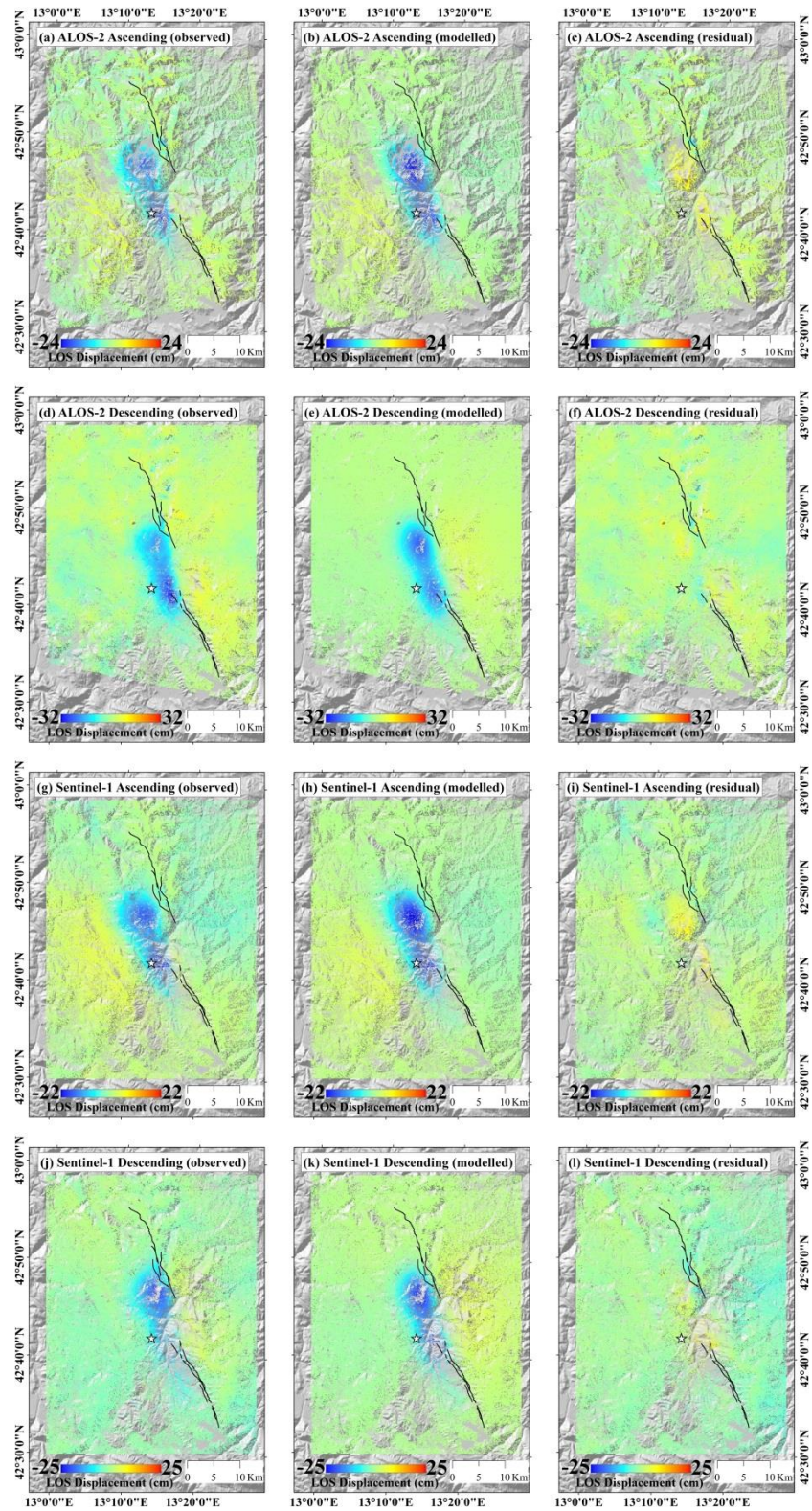


Figure 5.8 DInSAR fitting deformation for the 2016 24 August, Amatrice Earthquake.

Observed, modelled, and residual data from ALOS-2 ascending (a-c), ALOS-2 descending (d-f), Sentinel-1A/B ascending (g-i), Sentinel-1A/B descending (j-l). The white star is main shock and black lines in (a)-(l) are active faults from INGV.

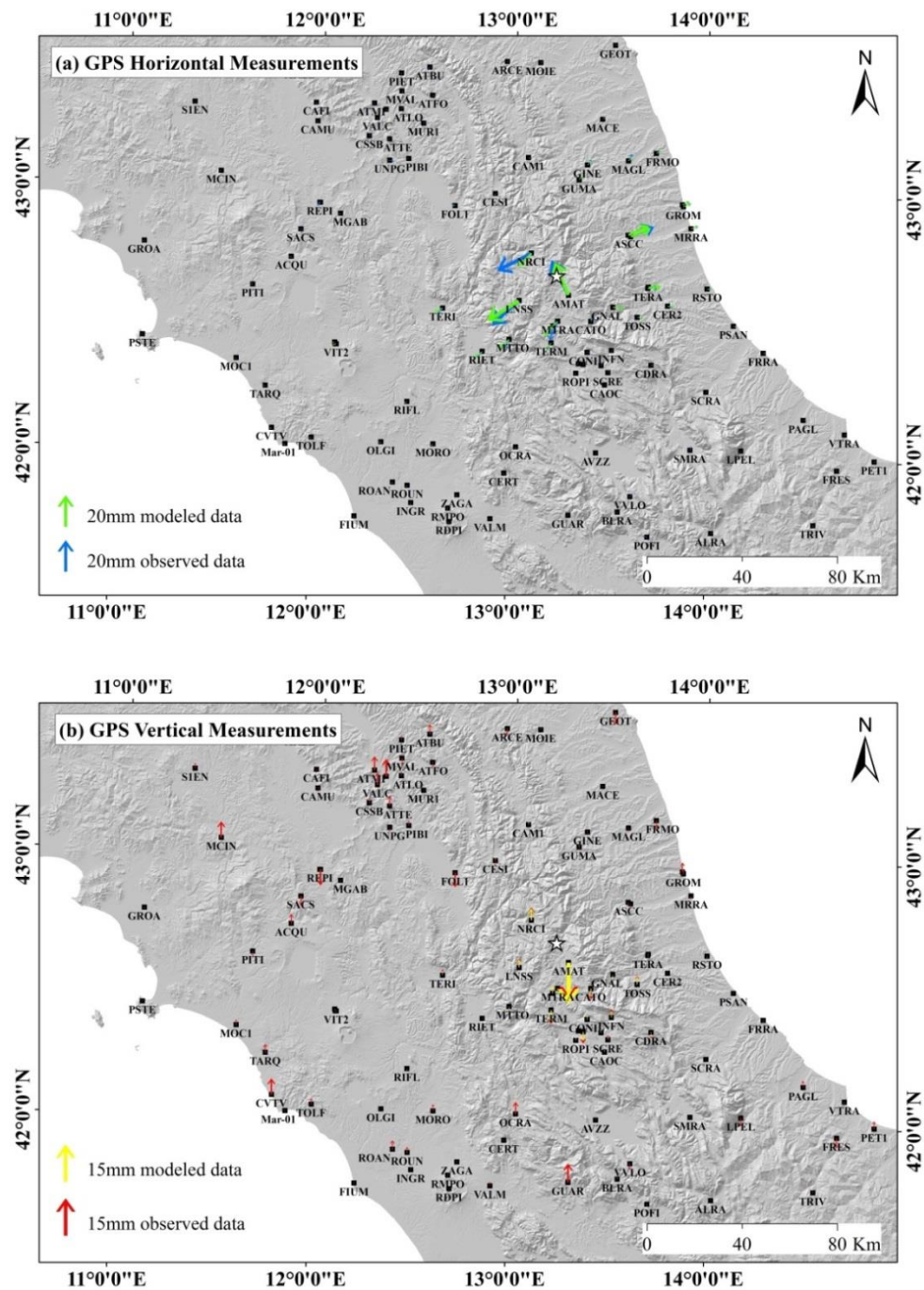


Figure 5.9 GPS horizontal (a) observed (blue) and model (green) data, as well as GPS vertical (b) observed (red) and model (yellow) data. The white star is main shock.

5.5 Discussion

5.5.1 Coulomb Stress Change Analysis

To understand the stress variation induced by the Amatrice Earthquake, we used the inferred distributed slip model as the source and estimated the stress change on the fault

plane itself using the Coulomb Failure Function (Harris, 1998). Based on the Coulomb Failure Function, the stress change on the specific receiver fault is shown as Equation (5.2):

$$\Delta CFF = \Delta\tau + \mu \cdot (\Delta\sigma_n - \beta \cdot T / 3) \quad (5.2)$$

Where $\Delta\tau$ is the shear stress change, μ is the friction coefficient, $\Delta\sigma_n$ is the normal stress change, β is the Skempton's coefficient and T is the stress tensor trace. Positive stress change indicates the risk of failure is increasing, which could further trigger earthquakes in this area, and vice versa. We set the friction coefficient μ and shear modulus to be 0.4 and $3.0 \times 10^{10} \text{N/m}$, respectively. Figure 5.10(a) shows the stress change induced by the slip distribution on the fault plane. The maximum stress variation reaches -11.33MPa , located in the northern slip asperity with 5km of depth. From the 3D view of stress change and aftershocks (Figure 5.10(b)), positive stress changes mainly occurred at a depth ranging from $1\text{-}2 \text{km}$ and $7\text{-}9 \text{km}$, coinciding with the majority of aftershocks. Therefore, high stress-loaded areas are consistent with the aftershock distribution. The positive stress change on the fault plane was up to 4.8MPa and high loaded stress areas ($>0.5 \text{MPa}$) equated to about 193km^2 .

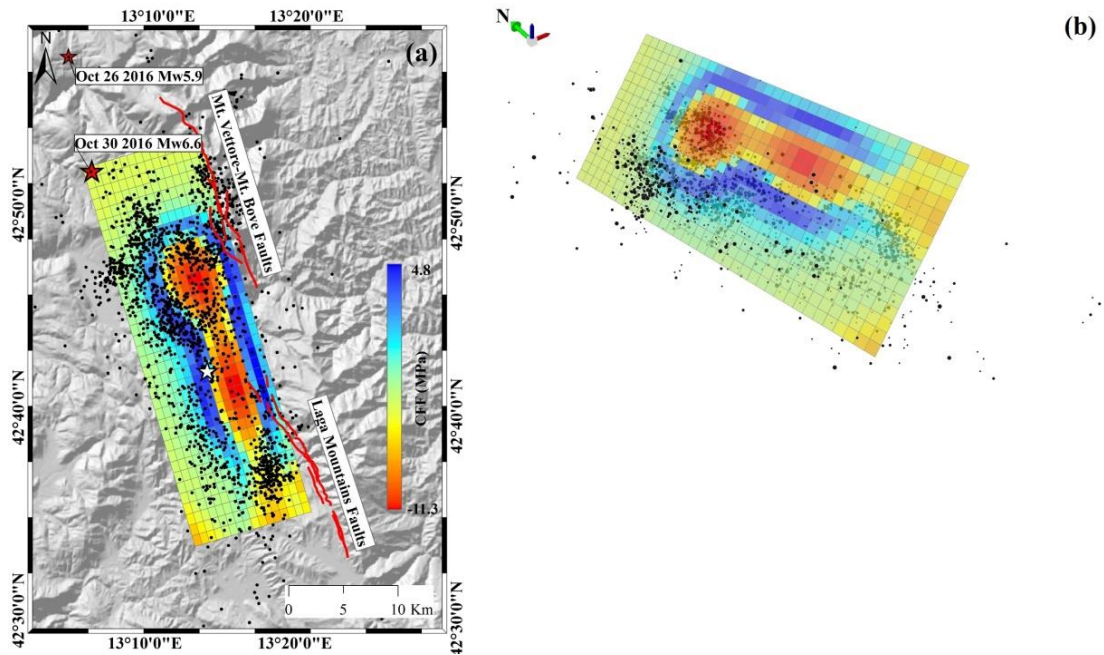


Figure 5.10 Stress change on (a) the source plane and (b) the corresponding 3D view. The white star is main shock, black dots are aftershocks and red lines are active faults from INGV. The red stars are October 26 Mw5.9 and October 30 Mw6.6 main shocks.

5.5.2 Triggering Relationship with the October 26 and 30 Event

The following two events (the 26 and 30 October earthquakes) occurred in the vicinity of the epicentre area of the Amatrice Earthquake (Figure 5.10). To further explore whether these two events were triggered by the first main shock (the Amatrice Earthquake), we adopted the distributed slip model of the Amatrice Earthquake obtained in this study as source fault, and the fault geometries and slip distribution of two posterior events inverted from the published work (Xu et al., 2017) as the receiver faults based on the calculation of the Coulomb stress change. The stress change on the fault plane of 26 October event is estimated only based on the source fault of the Amatrice Earthquake, while the stress change on the 30 October event is obtained based on the joint effect of the previous two events since this event is located just between the previous shocks.

The result of stress change on the fault plane of the 26 October event is shown in Figure 5.11(a). The stress increase dominated the whole fault plane, with the peak positive stress change of 0.33MPa located in the southern end of the fault plane. The high stress loaded areas ($\geq 0.05\text{MPa}$) on the fault plane is up to 113km^2 . Around the epicentre of the 26 October event, the average stress increase is about 0.02MPa, suggesting that the fault plane was brought closer to failure by the Amatrice Earthquake. Figure 5.11(b) shows the result of the Coulomb stress change on the fault plane of the 30 October event. Similar with the result of the 26 October event, the segments with stress increase occupied most of the areas of the fault plane, with totally 311km^2 . The highest positive stress change is up to 0.97MPa. The epicentre of the 30 October event is located on the segments with positive stress change, and the mean stress increase around the epicentre is approximate 0.09MPa. It should be noted that the peak stress increases estimated for both events in this work are relatively higher than the result of (Xu et al., 2017).

Both two following events are located around the areas with positive stress change (stress increase), also known as the stress triggering zones. This suggested that the Amatrice Earthquake may promote or trigger the following earthquake sequence (26 October 2016 Mw 5.9 and 30 October 2016 Mw 6.6 earthquakes).

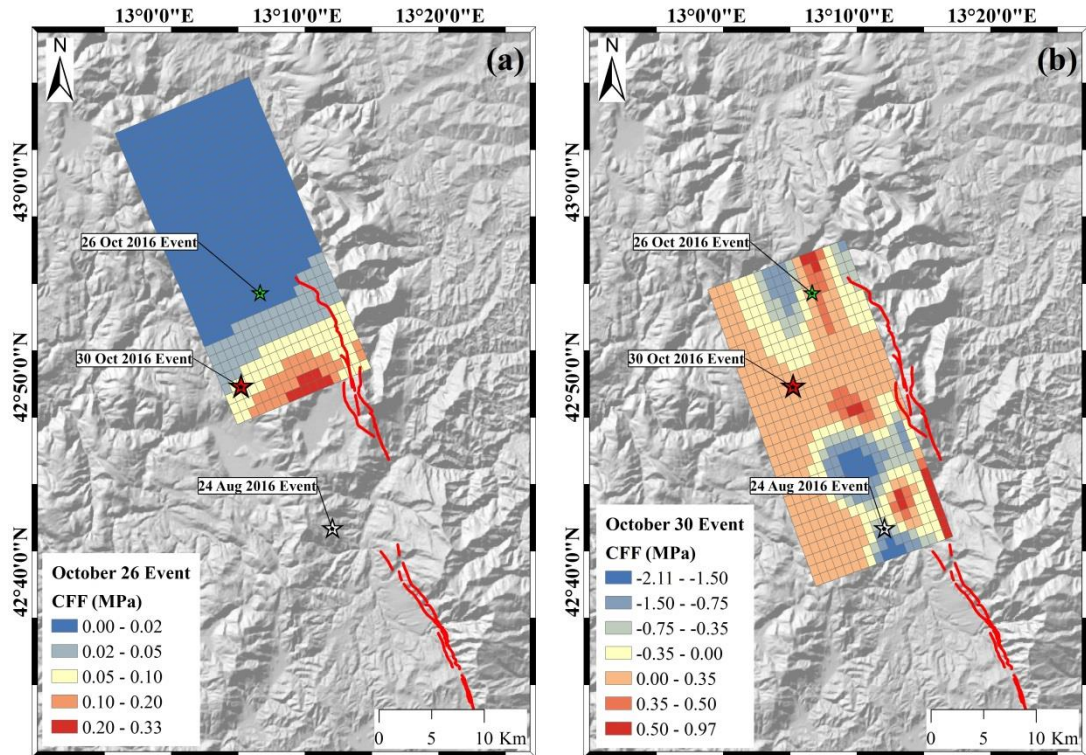


Figure 5.11 Coulomb stress change on (a) the fault plane of the 26 October 2016 event (Xu et al., 2017) induced by the Amatrice Earthquake, (b) the fault plane of the 30 October 2016 event jointly induced by the 26 October 2016 and the Amatrice Earthquake. The red lines are active faults from INGV. The white, green and red stars represent the epicenter of the Amatrice Earthquake, the 26 October event and the 30 October event, respectively.

5.6 Conclusion

In this study, source parameters and slip distribution of the 24 August 2016 Mw 6.2 Amatrice Earthquake (Central Italy) are investigated by using the DInSAR and GPS measurements. Our best-fit source parameters are in good agreement with the results of USGS, GCMT, INGV, the published work (Tinti et al., 2016, Cheloni et al., 2016, Lavecchia et al., 2016, Huang et al., 2017a, Liu et al., 2017, Cheloni et al., 2017, Xu et al., 2017) and aftershock distribution. Our study presents a normal fault plane striking NNW-SSE direction with a small left-lateral component. We found a maximum slip of 1.33m in the slip distribution and estimated seismic moment is $2.48 \times 10^{18} \text{Nm}$ (Mw 6.2). Two slip asperities from the distributed slip model are consistent with the deformation pattern measured from DInSAR. The stress change on the fault plane also shows consistency between high stress-loaded areas and aftershock distribution. Most

importantly, based on the source model of the published work (Xu et al., 2017), we found that the following earthquake sequence (October 26 and October 30 Earthquakes) could be probably triggered by the Amatrice Earthquake through the Coulomb stress change transfer. Thanks to the short revisit time of ALOS-2 and Sentinel-1A/B satellites, DInSAR can be used to map the co-seismic deformation of epi-central area and deliver comprehensive geological information for assessment of seismic hazard within a week after the main shock.

In the future, the double-fault solution for the 2016 Amatrice Earthquake will be studied to compare with the single-fault solution in this chapter. Furthermore, we hope that the natural hazard response and risk assessment for earthquakes can be carried out in near real-time with the development of satellites and DInSAR technique.

Chapter 6 Co-seismic deformation and source model of the 12 November 2017 M_w 7.3 Kermanshah Earthquake (Iran-Iraq border) investigated through DInSAR measurements

A large earthquake with a magnitude of M_w 7.3 struck the border of Iran and Iraq at the province of Kermanshah, Iran. In our study, co-seismic deformation and source model of the 12 November 2017 Kermanshah Earthquake are investigated using ALOS-2 ScanSAR and Sentinel-1A/B TOPS SAR Differential Interferometric Synthetic Aperture Radar (DInSAR) techniques. Geodetic inversion has been performed to constrain source parameters and invert slip distribution on the fault plane. The optimised source model from joint inversion shows a blind reverse fault with a relatively large right-lateral component, striking 353.5° NNW-SSE and dipping 16.3° NE. The maximum slip is up to 3.8m at 12-14km depth and the inferred seismic moment is 1.01×10^{20} Nm, corresponding to M_w 7.3, consistent with seismological solutions. The high spatial resolution optical images from SuperView-1 satellite suggest that most of linear surface features mapped by DInSAR measurements are landslides or surface cracks triggered by the earthquake. Coulomb stress changes on the source fault indicating consistency between aftershock distribution and high loaded stress zones. Based on the stress change on neighbouring active faults around this area, the Kermanshah Earthquake has brought two segments of the Zagros Mountain Front Fault (MFF), MFF-1 and MFF-2, 0.5-3.1MPa and 0.5-1.96MPa closer to failure, respectively, suggesting the risk of future earthquakes. Recent major aftershocks ($M_w \geq 5.0$) could probably ease the seismic hazard on MFF-2, but the risk of earthquakes on MFF-2 is still increasing.

6.1 Introduction

6.1.1 The 12 November 2017 Kermanshah Earthquake

On 12 November 2017, an M_w 7.3 earthquake struck the border region between Iran and Iraq, causing severe infrastructure damage over large areas with more than 620 fatalities and 8100 people injured. According to the United States Geological Survey (USGS), the epicentre was located at 34.905° N and 45.956° E with a depth of 19km (<https://www.usgs.gov/news/magnitude-73-earthquake-iraniraq-border>). A significant

foreshock with a magnitude of 4.4 occurred about one hour before the main shock, located just 60km SW of the main shock. Aftershocks with $M_w > 2.5$, as collected from the Iranian Seismological Centre (IRSC) between 12 November 2017 and 15 April 2018 suggest that the epicentre zone covered an area of approximately 100km×80km (Figure 6.1). The epicentre location and moment magnitude of this event were also determined by the strong motion data of 109 stations from the Iran Strong Motion Network (ISMN), indicating a magnitude of 7.3 occurred at a depth of 18.0km (Farzanegan et al., 2017). Focal mechanism resolved by seismological data from the USGS and the Global Centroid Moment Tensor (GCMT) (Dziewonski et al., 1981) both show a co-seismic rupture occurred on a NNW-SSE strike, oblique-thrust fault.

Preliminary field investigation carried out by the International Institute of Earthquake Engineering and Seismology (IIEES) reveals that the Sarpol Zahab and Qasr Shirin cities of Kermanshah Province in Iran suffered the most serious destruction and the maximum intensities (Zare et al., 2017). In addition, a preliminary assessment conducted by the Geological Survey of Iran also shows many local photos of the secondary co-seismic geological features on the ground, including landslide-rock avalanche, rockfalls and cracks on the Sarpol Zahab region and Ezgaleh city (Shahryar Solaymani Azad, 2017). According to the News report from the Nalia Radio and Television (NRT), the Darbandikhan Dam, a multi-purpose embankment located in the city of Darbandikhan, has suffered a 450m long crack in the upper part of the dam. The field survey carried by Building & Housing Research Centre (BHRC) also shows that there were many surface ruptures over the city of Sarpol Zahab, with a vertical displacement up to 3m, and a width of rupture reaching 1km. Hence, this study aims to further investigate whether most of surface ruptures and cracks around the epicentre area were caused by secondary faults, or triggered by gravitational deformation.

6.1.2 Tectonic background

The epicentre of the 2017 Kermanshah Earthquake is close to the Zagros Mountains which is originated by the northward collision between Eurasian plate and Arabian plate with a rate of approximately 20mm year⁻¹ (Reilinger et al., 1997, Mouthereau et al., 2012, Madanipour et al., 2013). These two plates converge at the Main Recent Fault and Main Zagros Reverse Fault which both bounded the Zagros fold and thrust belt (McQuarrie, 2004). The active faults in this region are mostly trending NW-SE, NNW-SSE with dips of 30-60° and rakes of 60-120° along the plate boundary (Hessami et al., 2003). The

Zagros Main Recent Fault (MRF), the High Zagros Fault (HZF), the Zagros Mountain Front Fault (MFF) and the Zagros Foredeep Fault (ZFF) are major faults in this region, as shown in Figure 6.1.

Even though this event is located close to the compressional boundary between two major plates, fewer large historical earthquakes have been recorded around this region. Historical earthquakes with $M_w > 6.0$ within 400km of the main shock recorded by the USGS before 1976, and the GCMT from 1976 to 2014, indicate a low rate of seismicity background for this region. A total of 13 previous earthquakes with $M_w > 6.0$ occurred in this region, and only two of them had a magnitude of over 6.5. The nearest one, recorded at a magnitude of 6.1, occurred on 11 January 1967 on the MFF, located about 100km south of the 2017 Kermanshah Earthquake. The earliest recorded earthquake (M_w 6.5) struck on the MRF on 13 December 1957, followed by another two major earthquakes with a peak magnitude of 6.7 in 1958 in the same area, about 190km SE of the Kermanshah Earthquake. A field investigation of this earliest reported earthquake shows an area of over 2800 km² was damaged, and nearly 1200 lives were lost (Ambraseys et al., 1973). However, the most serious and largest historical earthquake around this region was recorded on 20 June 1990, located around 400km NE of the Kermanshah Earthquake zone, on the Lahijian Fault, this quake of a magnitude of 7.4 (M_w) caused over 40,000 fatalities, and 60,000 injuries, leaving 500,000 people homeless (Berberian et al., 1992). The most recent historical event was reported on the SE segments of the MFF on 18 August 2014 (M_w 6.2), approximately 290 km SE of the 2017 Kermanshah Earthquake. Owing to fewer major earthquakes and lack of GPS stations installed in this region, the local strain around the plate boundary was not accurately estimated by seismological or geodetic data (Kreemer et al., 2014). However, the 2017 Kermanshah Earthquake provides researchers an opportunity to assess the risk of seismic hazard around this region using remote sensing data.

Hence, this study is set to measure the co-seismic deformation induced by the 2017 Kermanshah Earthquake using the ALOS-2 ScanSAR and Sentinel-1A/B TOPSAR data. The source model and slip distribution of the event were determined from a joint inversion of DInSAR measurements based on an elastic dislocation model (Okada, 1985). High spatial resolution optical images from SuperView-1 and DInSAR wrapped interferograms were used to investigate the linear surface features mapped by DInSAR measurements. In addition, co-seismic Coulomb stress changes on the source fault and neighbouring

active faults were explored to understand the stress change between aftershock distribution and different fault planes. The triggering relationship between most recent events ($M_w > 5.0$) and stress changes on different fault planes was further explored. We aim to demonstrate that remote sensing data, either radar or optical data, can play an important role in earthquake monitoring and natural hazard response in regions of scarce ground survey data.

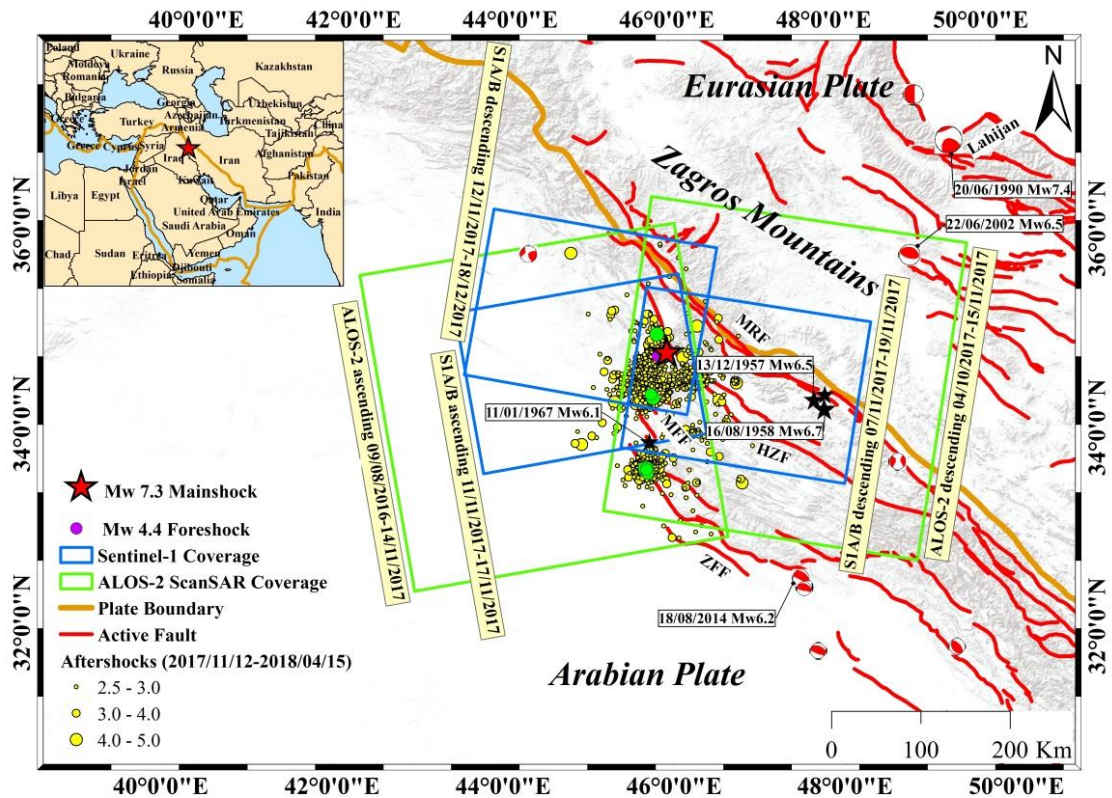


Figure 6.1 Tectonic setting of the 2017 M_w 7.3 Kermanshah Earthquake. Red star is the main shock and violet circle is the foreshock. Yellow circles are aftershocks with $2.5 < M_w < 5.0$ collected from the Iranian Seismological Centre (IRSC). Green circles are major events with $M_w > 5.0$ after the main shock. Red lines are active faults from the International Institute of Earthquake Engineering and Seismology (IIEES) (Hessami et al., 2003). Green and blue boxes represent the spatial coverage of ALOS-2 and Sentinel-1A/B SAR image pairs, respectively. Black stars represent the major historical earthquakes ($M_w > 6.0$) before 1976 from the USGS. Red focal mechanism plots denote the historical earthquakes ($M_w > 6.0$) between 1976 and 2014 from the GCMT.

6.2 Data availability and DInSAR measurements

6.2.1 Data availability

The dataset for this study consist of two SAR image pairs from ALOS-2 satellite and three pairs from Sentinel-1A/B. Table 6.1 provides detailed information for each pair of images, and Figure 6.1 shows their spatial coverage. The Sentinel-1A/B image pairs were acquired in Terrain Observation by Progressive Scans (TOPS) mode. TOPS SAR data can cover a swath width of 250km at about 5m by 20m resolution in the range and azimuth directions, respectively (Torres et al., 2012, De Zan and Guarnieri, 2006). The ALOS-2 image pairs used were acquired in the ScanSAR (Wide Swath) mode with a swath of 350km. Two pairs of descending Sentinel-1A/B data were needed to fully cover the area of interest. Because of the low vegetation and desert-like conditions in Iran and Iraq (Funning et al., 2005), it was expected that both L-band (ALOS-2) and C-band (Sentinel-1A/B) data can achieve high interferometric coherence.

Table 6.1 SAR image pairs used for the 2017 Kermanshah Earthquake

Satellite	Track	Orbit	Image Mode	Interferometric Pair (dd/mm/yyyy)	B_{\perp} (m)	B_T (day)	θ ($^{\circ}$)
ALOS-2	180	ASC	WD	09/08/2016- 14/11/2017	-86	462	40
	71	DESC	WD	04/10/2017- 15/11/2017	167	42	40
Sentinel-1A/B	72	ASC	IWS	11/11/2017- 17/11/2017	62	6	39
	79	DESC	IWS	12/11/2017- 18/11/2017	56	6	41
	6	DESC	IWS	07/11/2017- 19/11/2017	15	12	39

ASC is ascending and DESC is descending path. WD is Wide-Swath (ScanSAR) mode and IWS is Interferometric Wide Swath (TOPS) mode. B_{\perp} is perpendicular baseline, B_T is temporal baseline (day), θ is incidence angle.

6.2.2 DInSAR Measurements

All Single Look Complex (SLC) data were processed to generate the interferograms using the SARscape software. The Signal-to-Noise Ratio (SNR) of each interferogram was improved by multi-looking the ALOS-2 ScanSAR images with 1 by 5 looks, and Sentinel-1A/B images with 8 by 2 looks, in range and azimuth directions, respectively. For ALOS-2 ScanSAR interferometry, timing and phase compensation at the bounds of bursts and sub-swaths must be conducted in order to avoid phase discontinuities (Guarnieri and Prati, 1996). Regarding Sentinel-1A/B TOPS SAR data, co-registration with an accuracy of about 1/1000th of one pixel in the azimuth direction is required due to the Doppler centroid frequency variations caused by azimuth beam sweeping (González et al., 2015). The topographic phases, derived from the 3 arc-second Digital Elevation Model (DEM) from the Shuttle Radar Topography Mission (SRTM) (Farr et al., 2007), were used for removing the topographic effects. Interferograms were subsequently filtered using Goldstein Adaptive Filter (Goldstein and Werner, 1998). A linear function, consisting of slant range coordinate (range, azimuth) and error phase was estimated afterwards, with observations on the non-deforming areas to remove the residual phase and orbital error. Once this step was completed, the interferograms were unwrapped using Minimum Cost Flow method (Costantini, 1998, Costantini and Rosen, 1999), and geocoded to the WGS84 geographic coordinates with 180m resolution for ALOS-2 ScanSAR pairs, and 30m resolution for Sentinel-1A/B TOPS pairs (Figure 6.2).

Two elliptic deformation areas were observed in all the deformation maps. The maximum line-of-sight (LOS) deformation was 91.8cm and 48.8cm for ALOS-2 ascending and descending pairs, respectively. As for the DInSAR measurements from the Sentinel-1A/B ascending pair, the deformation pattern was similar to the ALOS-2 ascending result but with a peak deformation of 87.3cm along the LOS direction. Two Sentinel-1A/B descending deformation maps show similar deformation pattern but with different maximum LOS deformation around the epicentre, 65.0cm and 54.8cm for the 6-day and 12-day pairs, respectively. The difference of maximum LOS deformation detected from these two similar interferometric pairs is owing to various looking geometries. To reduce the number of data points and improve computational efficiency, several million data points in the area between latitude 33.41°N - 36.14°N and longitude 43.78°E - 47.90°E were subsampled using a regular mesh, of higher density around the deforming area. As

a result, 51,559 points were obtained, with 19,909 for ALOS-2 and 31,650 for Sentinel-1A/B (Figure 6.3).

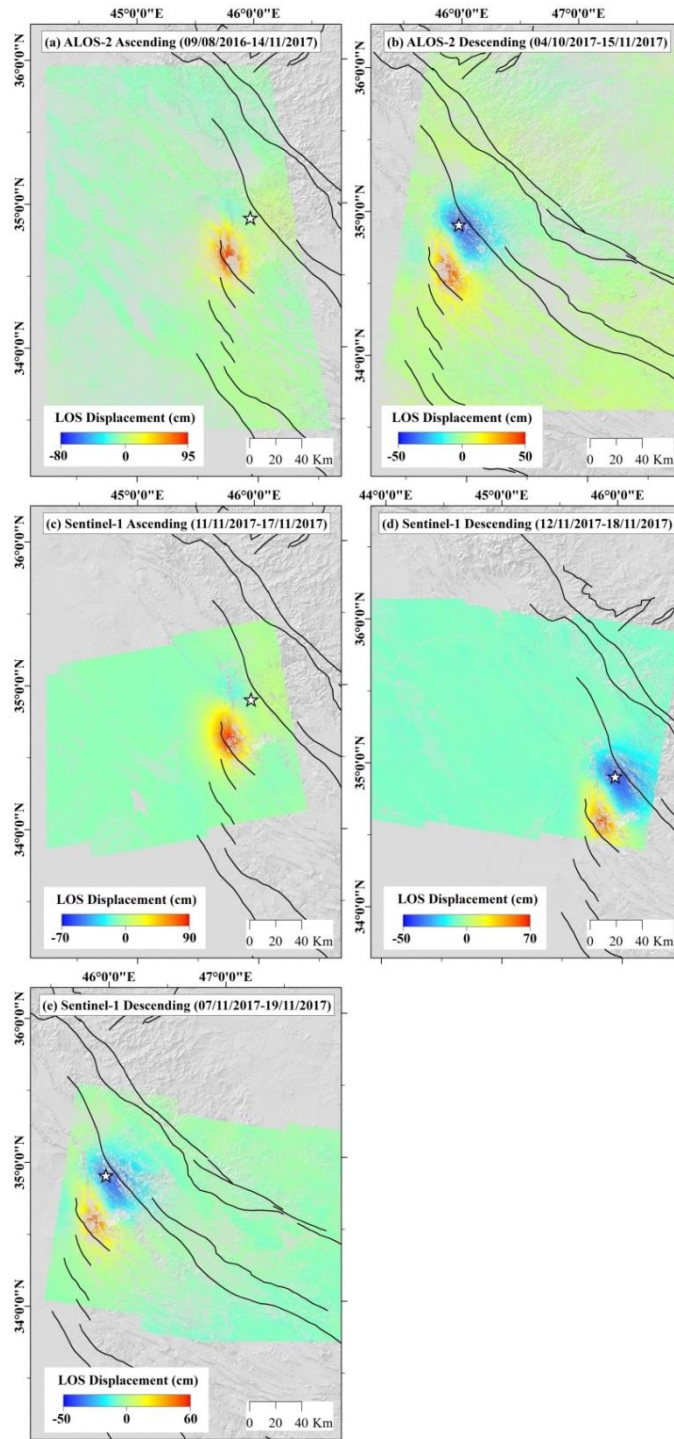


Figure 6.2 DInSAR measurements (LOS) of the 2017 M_w 7.3 Kermanshah Earthquake. (a)-(b) ALOS-2 ascending and descending displacement maps; (c)-(e) Sentinel-1A/B ascending and descending displacement maps. Red and blue colours represent decrease and increase in the LOS range, respectively. The white star is main shock, and black lines are active faults in western Iran.

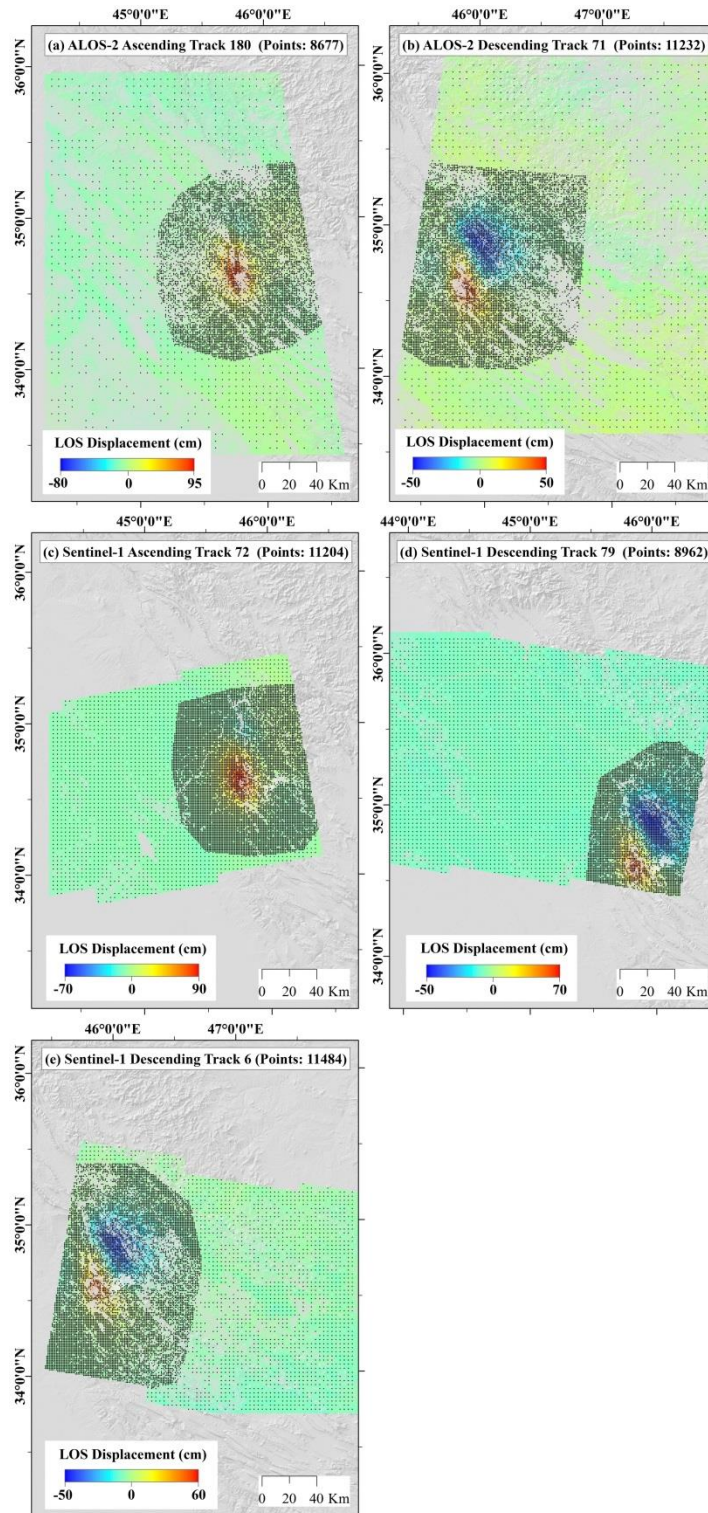


Figure 6.3 Down-sampled points from five co-seismic displacement maps used in this study. (a)-(b) ALOS-2 ascending (Track 180) and descending (Track 71) displacement maps; (c)-(e) Sentinel-1A/B ascending (Track 72) and descending (Track 79 and 6) displacement maps. Red and blue colours represent decrease and increase in the LOS range, respectively.

6.3 Modelling

To further analyse and describe the causative fault for the main shock, all subsampled observations were inverted using a finite dislocation model in an elastic, homogeneous half-space (Okada, 1985). Geodetic inversion consisted of two steps: a non-linear inversion was adopted to constrain all the fault parameters with a uniform slip model, followed by a linear inversion to infer slip distribution on the fault plane.

Non-linear inversion, a mix algorithm of Gauss-Newton iteration and gradient descent as the Levenberg-Marquardt (LM) least-squares approach (Marquardt, 1963), was applied to constrain 9 fault parameters (namely, length, width, depth, longitude, latitude, strike, dip, rake and slip) by assuming no dilation between the hanging wall and footwall. In order to retrieve slip distribution on the fault plane, a linear inversion was applied by fixing the fault geometry inverted from non-linear inversion. The length and width of the fault plane were extended to cover the earthquake's epicentre area. Subsequently, the fault plane was subdivided into small patches along the strike and dip; each patch measuring 5km×5km. To avoid extremely high values or oscillations in the result, a non-negative least-squares algorithm with a damping parameter was introduced into the system, as shown in Equation (6.1):

$$\begin{bmatrix} d_{\text{DInSAR}} \\ d_{\text{GPS}} \\ 0 \end{bmatrix} = \begin{bmatrix} G \\ \mathcal{E} \cdot \nabla^2 \end{bmatrix} \cdot m \quad (6.1)$$

Where d_{DInSAR} and d_{GPS} are DInSAR and GPS measurement vectors, m is slip vector, G is Green's function with an extended Laplacian operator ∇^2 which is weighted by an empirical coefficient \mathcal{E} (Wright et al., 2003). The empirical coefficient \mathcal{E} , also called damping factor, is determined based on the trade-off curve between the misfit of measurement and the solution roughness of slip distribution (Jónsson et al., 2002, Wright et al., 2004a). The solution roughness can be estimated as the mean, absolute Laplacian of the slip distribution (Jónsson et al., 2002), as shown in Equation (6.2):

$$\rho = \frac{\sum_i |P_i|}{2N} \quad (6.2)$$

Where $P = \nabla^2 m$ and N represents the total number of small patches on the fault plane. Changes in values of the damping factor generated different optimal solutions. High values resulted in a large misfit; low values led to small misfit, but with large oscillation in slip distribution. After several trials the damping factor was set to be 0.36 to obtain the best-fitting results, that is, a compromised solution minimising misfit and providing small roughness at the same time (Figure 6.4). A non-negative least square algorithm was adopted to positively invert this system and increase the reliability of the source model, as suggested by (Atzori and Salvi, 2014).

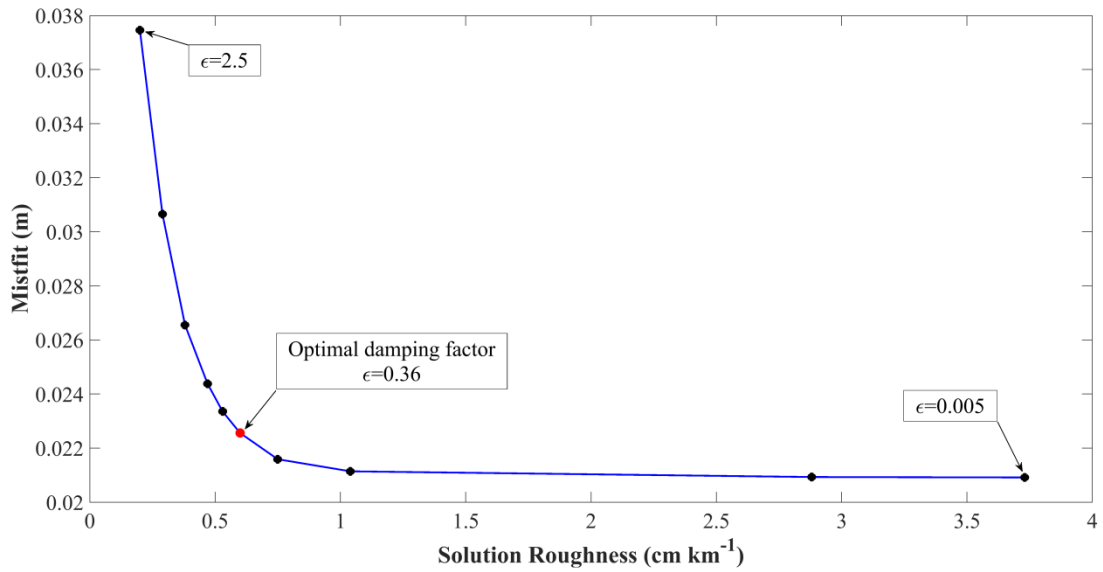


Figure 6.4 Trade-off curve between the misfit of measurement and the solution roughness for the slip distribution. Each black dot on the curve represents one individual experiment with specific value of damping factor. The red dot is the optimal damping factor with 0.36 we chose in this study.

6.4 Result

6.4.1 Separate inversion results using ALOS-2 and Sentinel-1A/B ascending and descending data individually

Firstly, we separately inverted the source model, using ALOS-2 or Sentinel-1A/B ascending and descending data independently. Table 6.2 shows the source parameter of uniform slip model using different dataset. The source fault models, as constrained by using ALOS-2 ascending and descending measurements separately, show a strike of about 353° and a rake of 140° , though with different dips. Both solutions are dipping NE, with a slightly larger dip (21.9°) for the ALOS-2 ascending inversion, as compared to a dip of 13.5° for the ALOS-2 descending solution. As well, different slip patterns can be identified from the slip distribution, as shown in Figures 6.5(a, b). A wider concentrated high-slip patch with a magnitude over 1.75m was retrieved from the slip distribution inversion using ALOS-2 ascending data, with a peak slip of approximately 4m at a depth of 14km, much higher than that from ALOS-2 descending inversion. With regard to source fault model constrained from Sentinel-1A/B ascending and descending measurements separately, strike and rake exhibit results similar to the ALOS-2 data; both solutions implied larger dip angles, with 27.3° and 15.4° for Sentinel-1A/B ascending and descending inversion, respectively. Figures 6.5(d, e) show the slip distributions for Sentinel-1A/B ascending and descending data, respectively. The results evidence a slip pattern similar to the comparison between ALOS-2 ascending and descending inversion, while the peak slip for Sentinel-1A/B descending solution is 3.58m at a depth of 15km.

Secondly, we inverted the slip distribution by jointly using ALOS-2 or Sentinel-1A/B ascending and descending data. Both solutions showed similar fault geometries, striking 353° NNW, dipping about 16.0° NE with a rake of $\sim 137^\circ$. Figures 6.5(c, f) show the inverted slip distributions, as constrained by ALOS-2 and Sentinel-1A/B data, respectively. The slip patterns from both solutions are consistent, suggesting a concentrated slip patch with a magnitude of over 1.0m at a depth of 10-17km. However, the peak slip inverted from the ALOS-2 ascending and descending inversion was 3.57m at a depth of 13km, which is slightly smaller than the Sentinel-1A/B ascending and descending solution, with a peak slip of 3.76m at the same depth.

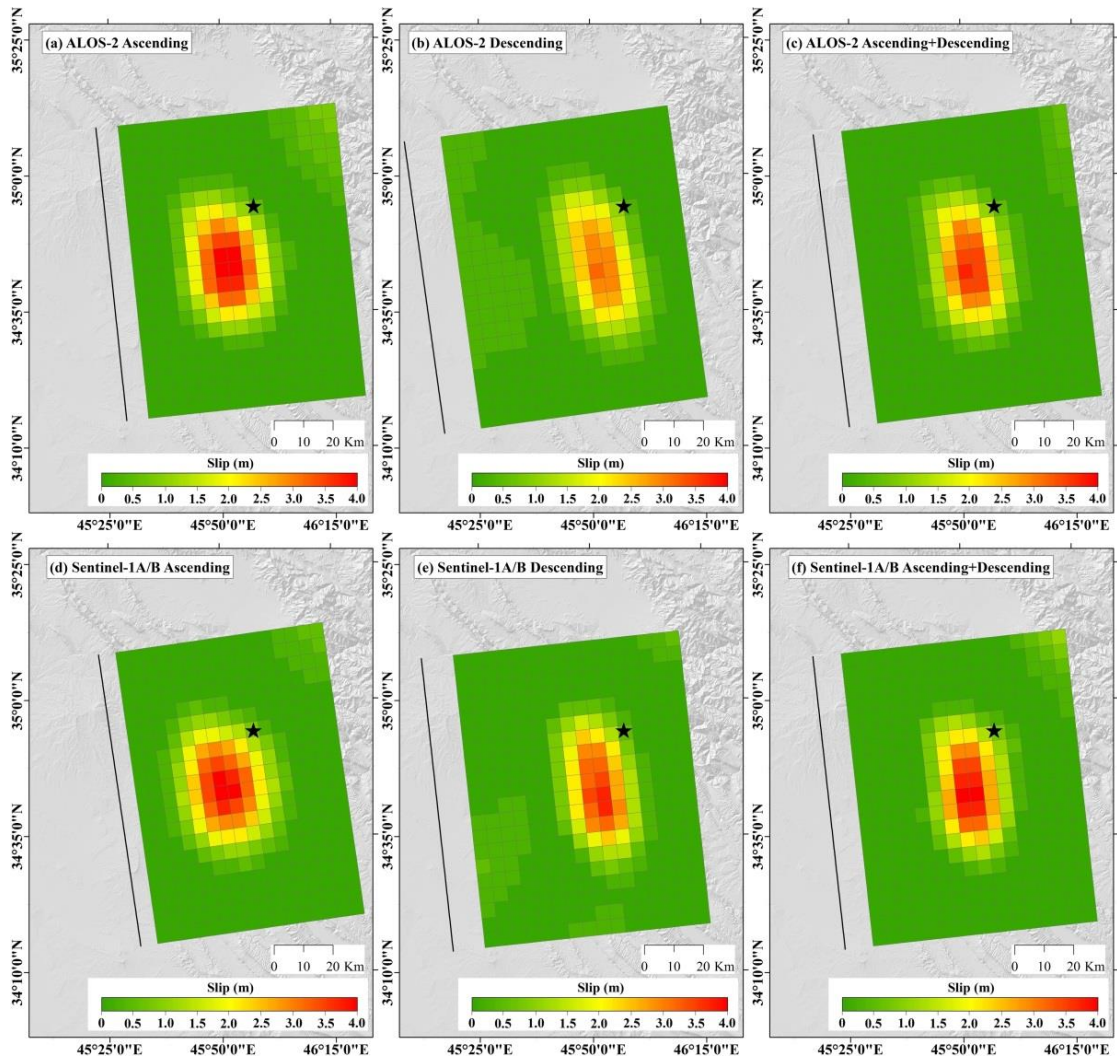


Figure 6.5 Slip distribution inverted by using (a) ALOS-2 ascending DInSAR measurements (Track 180), (b) ALOS-2 descending DInSAR measurements (Track 71), (c) ALOS-2 ascending and descending DInSAR measurements (Track 180 and 71), (d) Sentinel-1A/B ascending DInSAR measurements (Track 72), (e) Sentinel-1A/B descending DInSAR measurements (Track 79 and 6), (f) Sentinel-1A/B ascending and descending DInSAR measurements (Track 72, 79 and 6). The black star shows the epicentre from USGS and the black lines are corresponding fault traces intersected with the surface.

Table 6.2 Source parameters of uniform slip model inverted from different data

Data	Length (km)	Width (km)	Depth* (km)	Strike (°)	Dip (°)	Longitude** (°)	Latitude** (°)	Rake (°)	Slip (m)
ALOS-2 ASC	38.9	21.8	11.7	353.9	21.9	45.850	34.732	140.8	3.78
ALOS-2 DESC	43.6	17.0	12.4	352.1	13.5	45.861	34.729	139.6	3.35
Sentinel-1 ASC	37.8	19.5	13.6	351.7	27.3	45.835	34.736	143.2	4.60
Sentinel-1 DESC	41.4	15.2	13.2	353.8	15.4	45.858	34.731	141.0	3.85
ALOS-2 ASC and DESC	41.1	21.7	10.6	352.9	16.0	45.861	34.728	136.3	3.04
Sentinel-1 ASC and DESC	40.5	20.2	11.4	353.7	16.6	45.861	34.731	138.4	3.14

* The depth refers to the top centre of the fault plane

** Centre of the fault plane projected to the surface

6.4.2 Joint inversion results using both ALOS-2 and Sentinel-1A/B data

A joint inversion using ALOS-2 and Sentinel-1A/B data was implemented to invert the optimized source fault. The best-fit source fault constrained from the uniform slip model shows a reverse fault with a relatively large right-lateral component, striking 353.5° NNW-SSE and dipping 16.3° NE with a depth of 11km (refer to top edge of the fault plane). The strike, dip and rake are similar to the solutions reported by the USGS and the GCMT (Table 6.3). Also, the small NE-dipping angle obtained generally agrees with the results from the Geospatial Information Authority of Japan (GSI) (Kobayashi et al., 2017) and previous studies in this region (Vergés et al., 2011, Madanipour et al., 2013). Fixing the fault geometry from the uniform slip model, and extending the fault length and width 100km along the strike and 80km along the dip, respectively, resulted in an inverted slip distribution, with a distributed slip model. Likewise, the fault plane was discretized into 320 patches of $5\text{km} \times 5\text{km}$. Figure 6.6 shows the slip distribution on the fault plane; with most of the slip occurring at depth between 10-17km, the peak slip appears to have been of 3.87m at a depth of 13km. The total inferred seismic moment was estimated at 1.01×10^{20} Nm, corresponding to a moment magnitude of M_w 7.3, which is consistent with results from the USGS, IRSC and ISMN, but slightly smaller than the GCMT (M_w 7.4). The aftershocks (Fig. 6.6(b)) generally appear to be located around the fault plane, indicating a good agreement between fault geometry and aftershock distribution.

Figure 6.7 shows the residuals from the misfit between DInSAR LOS observations and model data. The small root mean square error (RMSE) values from misfit analysis indicate that the observed data were well reproduced for most of the areas. The RMSE values are 2.8cm, 2.2cm, 1.9cm, 1.5cm and 2.9cm for ALOS-2 ascending, ALOS-2 descending, Sentinel-1 ascending, Sentinel-1 descending and Sentinel-1 12-day descending pairs, respectively. The residual deformation is likely due to secondary co-seismic geological disasters (landslides and rockfalls).

Table 6.3 Fault parameters of Kermanshah Earthquake from seismology and geodetic inversion

Source	Length (km)	Width (km)	Depth (km)	Strike (°)	Dip (°)	Longitude (°)	Latitude (°)	Rake (°)	Slip (m)	Seismic Moment (10 ²⁰ Nm)	Mw	Data
USGS			19.0	351.0	16.0	45.956	34.905	137.0		1.12	7.3	
GCMT			16.9	351.0	10.0	45.880	34.790	143.0		1.72	7.4	
IRSC			18.1			45.762	34.772				7.3	
ISMN			18.0			45.910	34.810				7.3	Strong motion
(Kobayashi et al., 2017)	100.0	80.0	3.0		16.0				~3.0	1.18	7.3	ALOS-2
Uniform Slip Model	40.7	21.0	11.0*	353.5	16.3	45.862**	34.730**	137.5	3.06	0.79	7.2	ALOS-2, Sentinel-1A/B
Distributed Slip Model	100.0	80.0	2.8*	353.5	16.3	45.865**	34.730**	137.5	3.87	1.01	7.3	ALOS-2, Sentinel-1A/B

* The depth refers to the top centre of the fault plane

** Centre of the fault plane projected to the surface

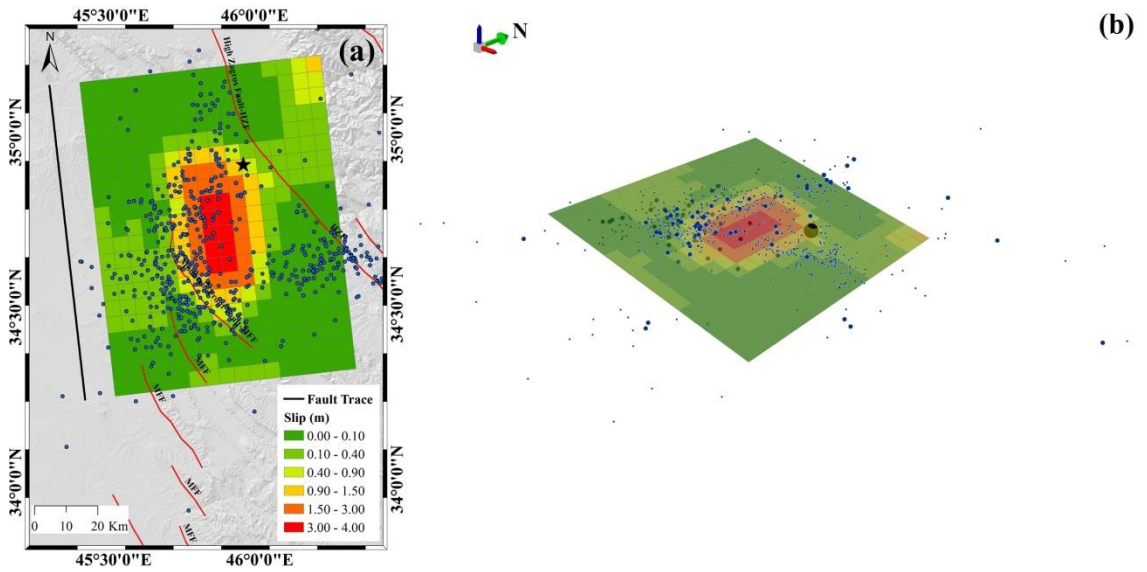
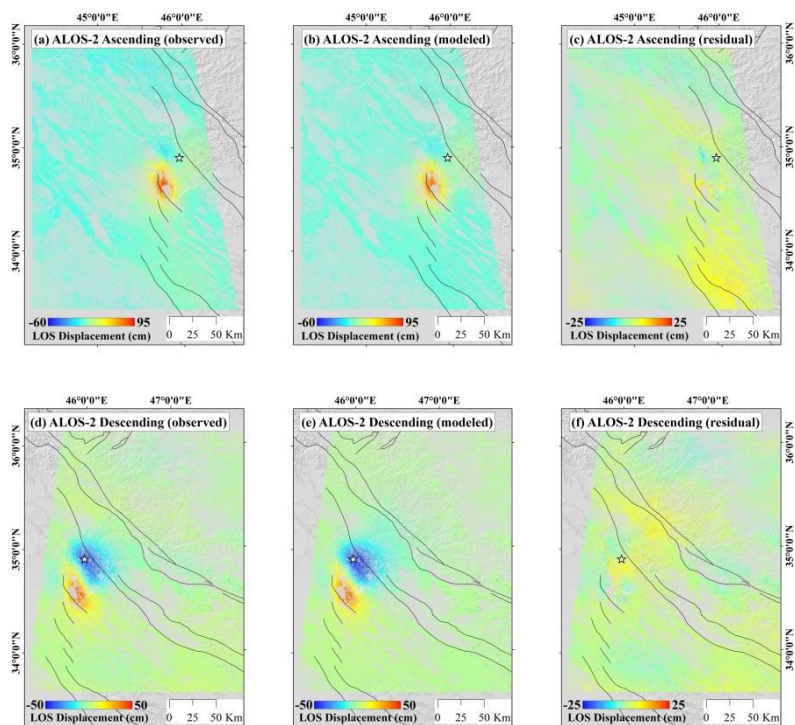


Figure 6.6 Fault slip distribution and aftershock distribution of the 2017 Mw 7.3 Kermanshah Earthquake, 2D view of surface projection (a) and 3D view (b). The black star in (a) is main shock, corresponding to the black sphere in (b). Black line is fault trace intersected with the surface. Blue dots in (a-b) are aftershocks, and red lines in (a) are active faults.



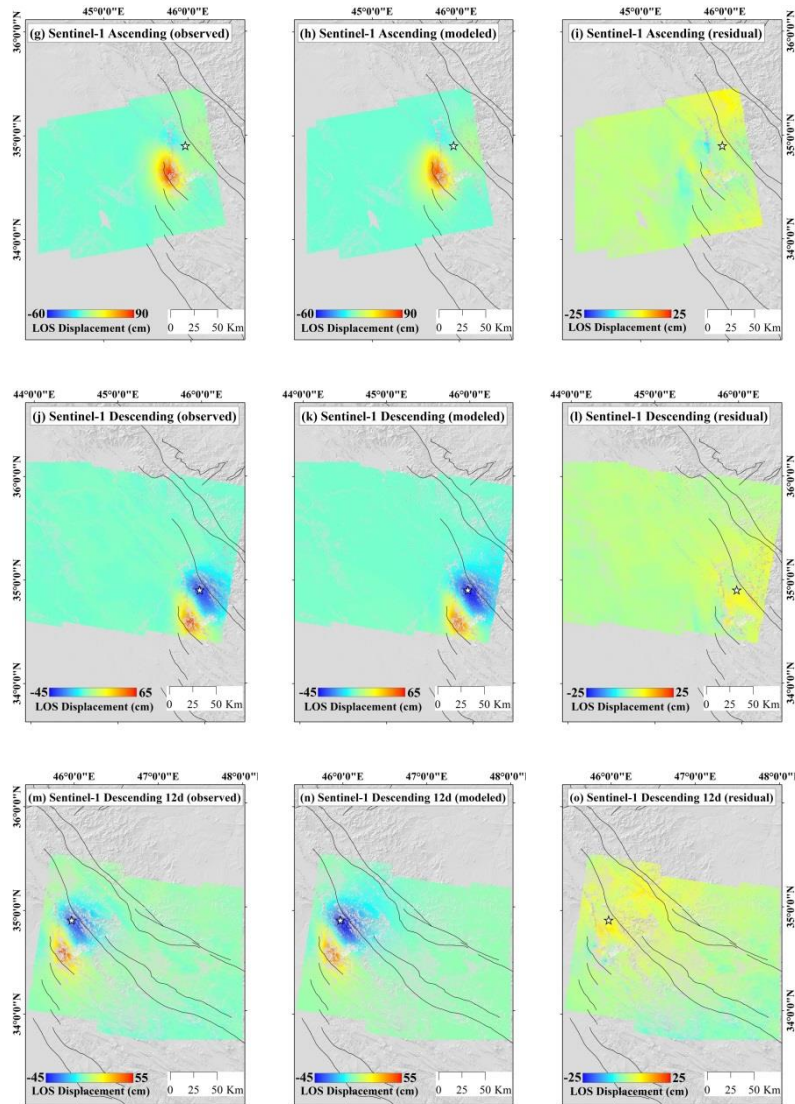


Figure 6.7 Misfit analysis for the 2017 Mw 7.3 Kermanshah Earthquake. Observed, modelled and residual data from ALOS-2 ScanSAR ascending (a-c) (Track 180) and descending (d-f) (Track 71), Sentinel-1A/B ascending (g-i) (Track 72), descending (j-l) (Track 79) and descending of 12days (m-o) (Track 6). White star is main shock, and black lines are active faults in western Iran.

6.5 Discussion

6.5.1 Linear surface ruptures of the 2017 Kermanshah Earthquake

Linear surface ruptures were mapped in the epicentre area from both ALOS-2 and Sentinel-1A/B ascending and descending interferograms, as shown in Figure 6.8. Large linear phase discontinuities reached tens of kilometres, featured by loss of coherence near the cities of Sarpol Zahab and Darbandikhan. Especially around the village of Sar Cheqa,

as shown by the dash violet rectangle in Figure 6.8(a-d), clear linear features were found away from the epicentre area. High spatial resolution optical images can be used to verify some small deformation, when combining with the SAR images. This study gathered three SuperView-1 images, acquired three days after the main shock, on 16 November 2017, with 0.5m and 2m spatial resolution in panchromatic and multispectral mode, respectively. The spatial coverage of each image is shown as white boxes in Figure 6.8(a-d). Image 098 was acquired around the city of Sarpol Zahab, images 097 and 087 jointly cover the city of Darbandikhan, where the Darbandikhan dam is located.

The optimized source fault model indicated that the 2017 Kermanshah Earthquake occurred on a right-lateral reverse fault without obvious surface rupture on the ground. The abovementioned high spatial resolution SuperView-1 images were used to verify the linear surface features mapped by DInSAR measurements. A SuperView-1 Pan-sharpened image with 0.5m resolution was generated by merging the panchromatic (0.5m) and multispectral (2m) imagery. Linear surface features near the cities of Sarpol Zahab, Darbandihab and Sar Cheqa were investigated (Figure 6.9). A large area of loss of coherence along the linear features was observed near the city of Sarpol Zahab, shown with a green dashed rectangle in Figure 6.9(a), corresponding to the same area of the SuperView-1 098 image of Figures 6.9(b, c). Obvious surface cracks and landslides in both of panchromatic and pan-sharpened images were clearly identified within the same area. The crack traces on the ground are consistent with the linear surface features mapped from DInSAR measurements. Most surface cracks spread in a NNW-SSE direction and the width of crack zone is up to 400m. The landslides generally expanded downward, along a SW direction, reaching an area of up to 14488.8m². Two areas near the city of Darbandikhan exhibit phase discontinuity and loss of coherence (green dashed rectangles in Figure 6.9(d)). For the area (e) highlighted in Figure 6.9(d), two significant landslides were identified close to the Darbandikhan Dam, which is a rockfill embankment with a central clay core, as shown in Figure 6.9(e). Visual interpretation of the pan-sharpened SuperView-1 097 image acquired three days after the earthquake (Figure 6.9(e)), evidence the floodgates of the dam opened to decrease the water level behind the dam. Area (f) highlighted in Figure 6.9(d), and corresponding to the pan-sharpened SuperView-1 087 pan-sharpened image (Figure 6.9(f)), exhibit several landslides along the road, with the largest area of 60549.9m².

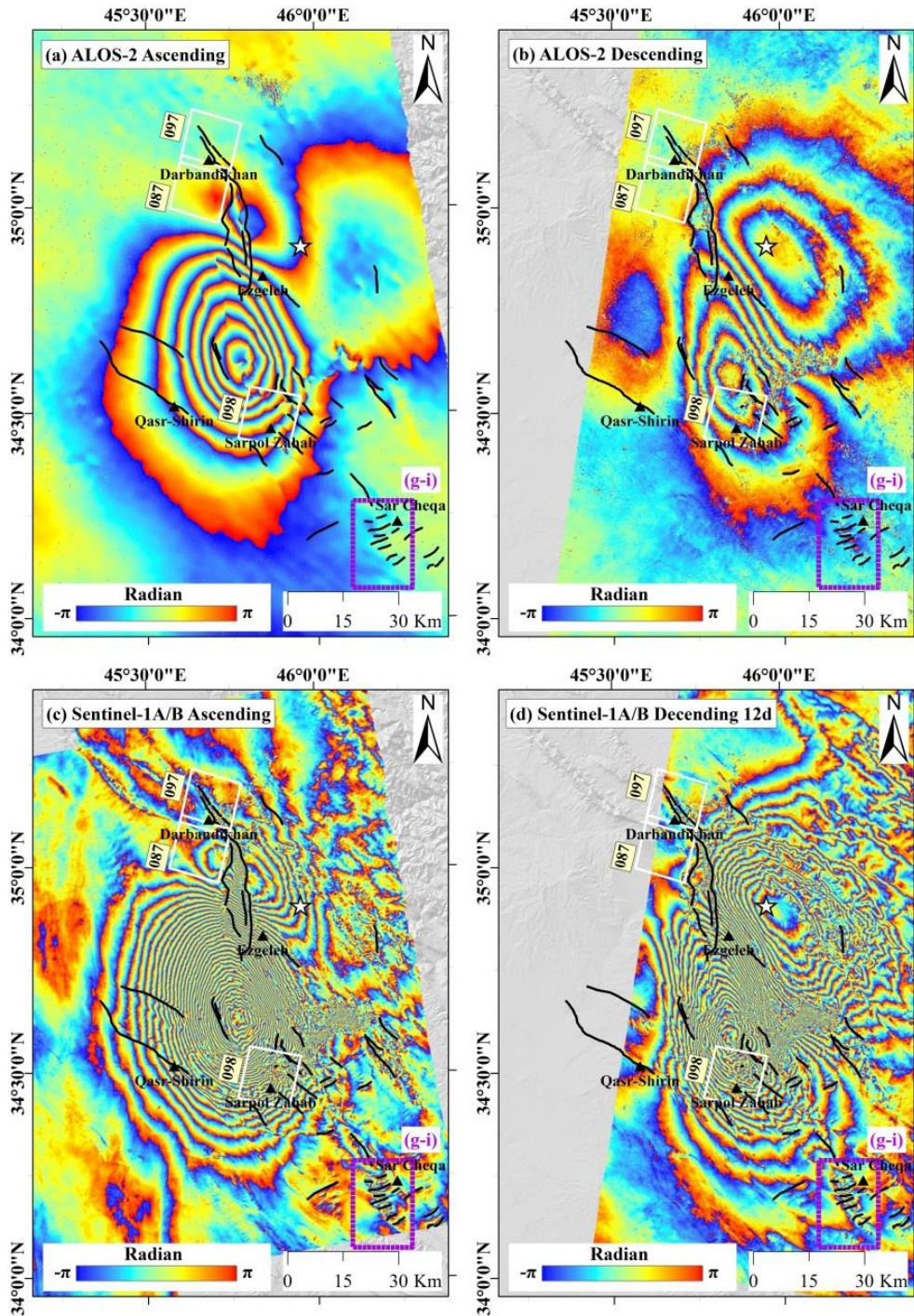


Figure 6.8 Linear surface ruptures (black lines) identified in (a) ALOS-2 ascending interferogram (Track 180), (b) ALOS-2 descending interferogram (Track 71), (c) Sentinel-1A/B ascending interferogram (Track 72) and (d) Sentinel-1A/B descending interferogram (Track 6). The white star shows the epicentre from USGS and the black triangles are major cities nearby. The white boxes are the footprints of SuperView-1 images. The violet rectangle is the coverage of Figure 9(g-i).

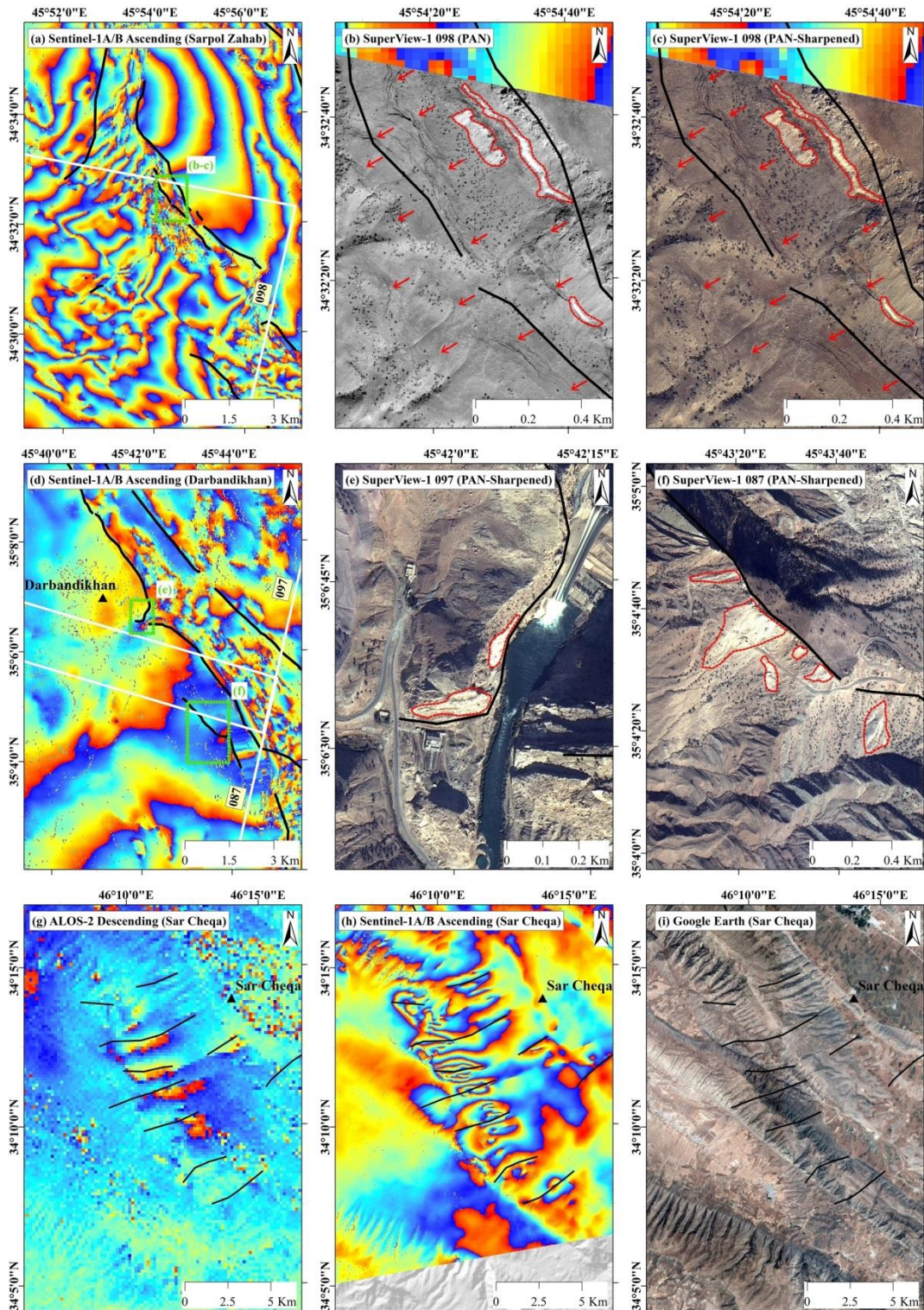


Figure 6.9 Triggered landslides and surface ruptures near the city of Sarpol Zahab (a-c), Darbandikhan (d-f) and Sar Cheqa (g-i). See Figure 6.8 for the location of (g-i). The black lines are mapped linear surface ruptures from DInSAR measurements, and the black triangles are major cities or villages. The red arrows show the surface cracks and the red polygons indicate the triggered landslides.

We also found a cluster of linear fringes on ALOS-2 and Sentinel-1A/B ascending and descending interferograms near the village of Sar Cheqa (violet dashed rectangles in Figure 6.8). Figures 6.9(g) and 6.9(h) correspond to the same area and show persistence of the cluster over different satellites and time spanning, indicating possible secondary deformation over this area. Owing to the small spatial baseline of ALOS-2 and Sentinel-1A/B interferometric pairs used in this study (Table 6.1), potential topographic errors or artifacts are unlikely to be responsible for these observed large deformations. An analysis of the area using Google Earth (Figure 6.9(i)), shows that most of the fringes with the linear surface features are located on the slopes of mountains, suggesting high potential for the occurrence of landslides, rockfalls or slump blocks over the area.

Corroboration between DInSAR measurements and the high spatial resolution SuperView-1 images over these three cities, suggest that most of the linear surface ruptures mapped by DInSAR could be landslides, cracks or any other triggered gravitational deformation over the epicentre area, rather than secondary fault ruptures. There are other two main reasons to support this conclusion. None of surface rupture features appear to connect directly to the source fault at depth. Most of them are superficial fractures or landslides rather than fault ruptures on the surface. As well, the topography of steep slopes and rough mountainous landscape dominating this region are supportive of these gravitational deformations.

6.5.2 Triggering relationships with neighbouring active faults

A co-seismic slip caused by earthquake is relevant to aftershock distribution and Coulomb stress change on the causative fault and the neighbouring active fault systems. To calculate the stress variation induced by the 2017 Kermanshah Earthquake, we used the inferred distributed slip model as the source, and estimated the stress change on the fault plane itself using a Coulomb Failure Function (Harris, 1998). Subsequently, the impact of stress change caused by this earthquake on neighbouring active faults was explored. Based on the Coulomb Failure Function, the stress change on the specific receiver fault is shown as Equation 6.3:

$$\Delta CFF = \Delta\tau + \mu \cdot (\Delta\sigma_n - \beta \cdot T / 3) \quad (6.3)$$

Where $\Delta\tau$ is the shear stress change, μ is the friction coefficient, $\Delta\sigma_n$ is the normal stress change, β is the Skempton's coefficient and T is the stress tensor trace. Negative

Coulomb stress change denotes decrease in stress, reducing the risk of the failure. Positive Coulomb stress change indicates the stress on the specific fault is increasing, which could further accelerate the failure of the fault. Aftershocks generally occur around the segments of fault plane with positive stress change.

As Equation (6.3) shows, the friction coefficient μ and shear modulus were set to be 0.4 and 3.0×10^{10} N/m, respectively. Figure 6.10(a, b) shows the stress change on the source fault plane, with a maximum stress release of up to 7.2MPa at a depth of 13km, and a peak stress increase of 2.63MPa at a depth of 9km. Positive stress changes mainly occurred at a depth ranging from 7-10km and 15-20km, where most aftershocks occurred. On the other hand, stress decrease (negative stress changes) areas were identified at the middle of the source fault plane, coinciding with the occurrence of the main shock. Hence, high loaded stress areas are consistent with the aftershock distribution.

Several active faults are observed on, or near, the stress increase areas (Figure 6.10(a, c)), could be influenced by the 2017 Kermanshah Earthquake. Hence, we further explored the impact that stress changes caused by the earthquake may have had on neighbouring active faults, specifically on the fault plane of the High Zagros Fault (HZF) and the Zagros Mountain Front Fault (MFF), as shown in Figure 6.10(c). Two fault segments at MFF (MFF-1 and MFF-2) and one fault segment at HZF were adopted as receiver sources in the stress change estimation. The estimated fault geometry of MFF-1, MFF-2 and HZF from a previous study of active faults in Iran (Hessami et al., 2003) was adopted to reconstruct the receiver faults, generally striking NNW and dipping NE 30-60°. It is worth noting that MFF-1, MFF-2 and HZF intersect with the source fault of the Kermanshah Earthquake at a depth of 10km, 11km and 18.5km, respectively. We found a positive stress change on the MFF-1 and MFF-2, and mainly negative stress change on the HZF. The peak positive stress changes on the MFF-1 and MFF-2 were estimated at 3.1MPa at a depth of 9.5km, and 1.96MPa at a depth of 10km, respectively. High loaded stress areas (>0.5 MPa) on the MFF-1 and MFF-2 are equal to 264km^2 and 136km^2 , respectively.

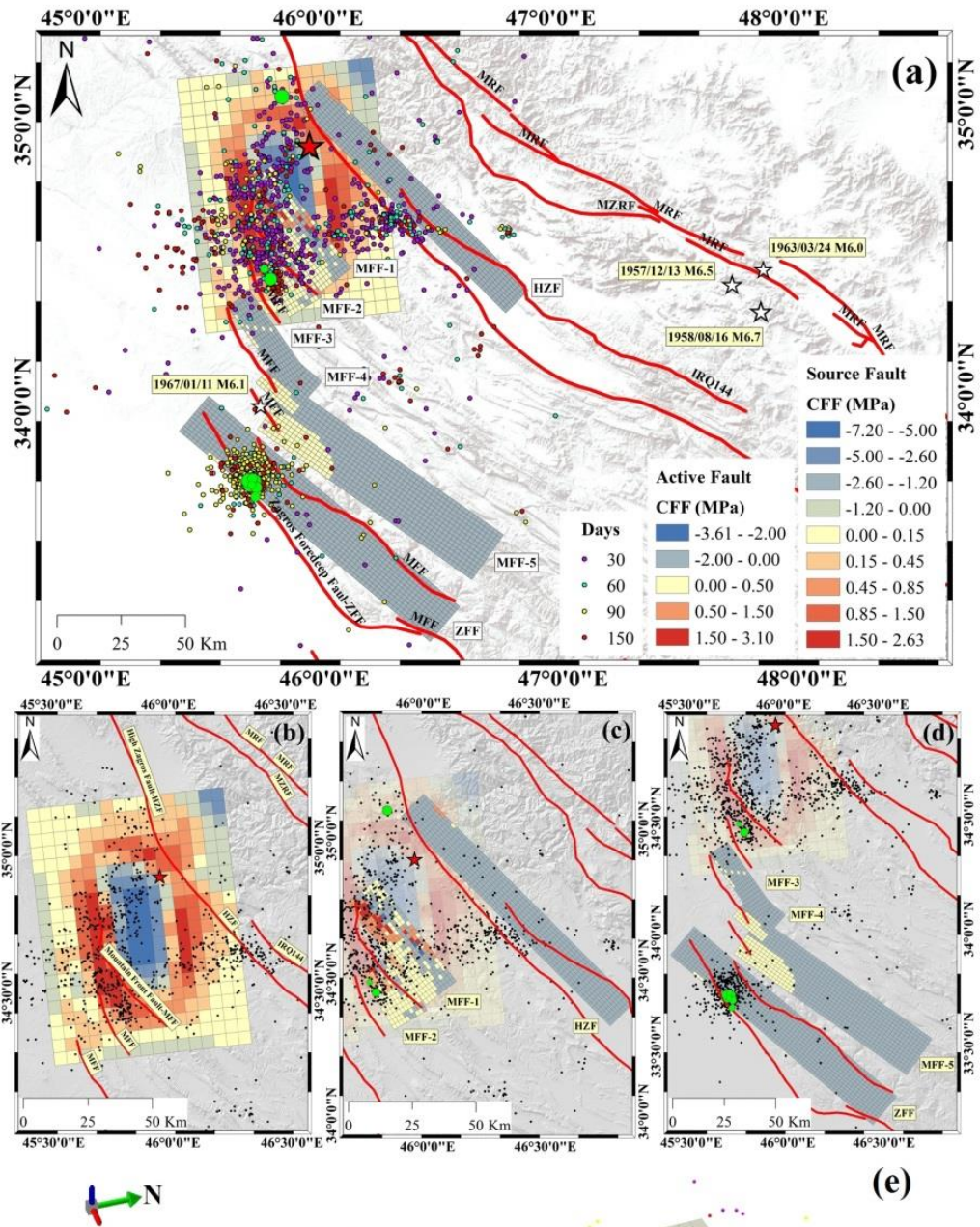


Figure 6.10 (a) Coulomb stress change on the source fault plane of the Kermanshah Earthquake and the neighbouring active faults investigated in this study. White stars are

major historical earthquakes in this region. The small dots with different colours are aftershocks occurred within 150 days after main shock, same as the black dots in (b-d).

Enlarged maps for (b) source plane; (c) MFF-1, MFF-2, HZF; (d) MFF-3, MFF-4, MFF-5 and ZFF. (e) The 3D view for source fault and active fault planes. The red star in (a-d) shows the main shock, corresponding to the black sphere in (e). Green circles in (a-e) show the location of major aftershocks ($\geq M_w 5.0$). Red lines are active faults.

Before the 2017 $M_w 7.3$ Kermanshah Earthquake, only four major earthquakes with over a magnitude of 6.0 occurred on MFF and MRF over the last 50 years; none of which is larger than $M_w 7.0$ (as shown in Figure 6.1 and Figure 6.10(a)). Our inverted source fault model shows the 2017 Kermanshah Earthquake ruptured on one of the segments of the Mountain Front Fault (MFF) rather than HZF around the epicentre. However, the proximity among other segments of MFF, HZF and the source fault of this event brought out the question of whether this earthquake could promote or trigger any other earthquake activities on these two major fault systems. Coulomb stress change analysis (Figure 6.10(c)), the rupture of the 2017 Kermanshah Earthquake brought 0.5-3.1MPa and 0.5-1.96MPa to MFF-1 and MFF-2, closer to failure respectively. This suggests that the risk of earthquakes on both MFF-1 and MFF-2 is increasing. However, there is more negative stress change imparted to HZF. After collecting major aftershocks ($M_w \geq 5.0$) within 200 km around the epicentre between 12 November 2017 and 11 April 2018 from the IRSC, we found two events occurred on the fault plane of MFF-2; one with $M_w 5.0$ on 6 January 2018 and the other with $M_w 5.3$ on 1 April 2018 (shown with green in Figure 6.10(a, c)). Both aftershocks occurred on the segments of MFF-2 that exhibited positive stress changes, which is consistent the Coulomb stress analysis undertaken in this study. Thus, it appears that the risk of seismic hazard on MFF-1 keeps increasing, while it is likely that the major aftershocks on MFF-2 reduced the chance of fault failure.

Moreover, we found a series of events with a magnitude over $M_w 5.0$ occurred on the ZFF on 11 January 2018, with a peak magnitude of 5.6, shown by the green circles in Figure 6.10(a, d). These major events were followed by a cluster of small events ($2.5 \leq M_w < 5.0$) that occurred over the same region. Owing to the nearly parallel location between MFF and ZFF, we also explored the Coulomb stress change on these faults using the estimated geometry (Hessami et al., 2003) to evaluate their risk of failure. Figure 6.10(d) shows only a few segments with small stress increase ($\leq 0.5\text{MPa}$) on MFF-3,

MFF-4, MFF-5 and ZFF. Also, the negative stress change dominates the fault planes of MFF-3, MFF-4, MFF-5 and ZFF, suggesting that the 2017 Kermanshah Earthquake is likely to inhibit the failure of these four active faults. Fewer aftershocks were observed between the source fault of the 2017 Kermanshah Earthquake and ZFF, where MFF-3, MFF-4 and MFF-5 are located (Figure 6.10(a, e)); Hence it is likely these major events and the following small quakes are not related to the aftershocks triggered by the 2017 Kermanshah Earthquake. Even though aftershocks following the main shock could occur within the distance one or two times of rupture length from source fault, these major events occurred on ZFF should be classified as new events on various sources, unrelated to the aftershocks.

6.6 Conclusion

This case study used ALOS-2 ScanSAR and Sentinel-1A/B TOPSAR ascending and descending data to map the co-seismic deformation of the 2017 M_w 7.3 Kermanshah Earthquake. The low-vegetation coverage and desert-like condition enabled DInSAR measurements maintain a high level of coherence over most parts of the region. Many linear surface features were detected from both ascending and descending wrapped interferograms. The maximum LOS deformation measured from DInSAR was up to 90cm. Using the DInSAR measurements, source parameters and slip distribution of the 2017 Kermanshah Earthquake were determined by a joint inversion. The results indicate a blind reverse fault striking 353.5° NNW-SSE and dipping 16.3° NE with a large right-lateral component. The peak slip was up to 3.87m at a depth of 13km. The results of joint inversion are consistent with seismological solutions and published result from the Geospatial Information Authority of Japan (GSI) using ALOS-2 data (Kobayashi et al., 2017). The calculation of Coulomb stress change on the source fault and neighbouring active faults evidences high loaded stress change on the source plane, consistent with aftershock distribution. Most importantly, we found that the stress increase on two segments of the Zagros Mountain Front Fault (MFF), MFF-1 and MFF-2, are relatively high and cover a large area on the fault plane. This may promote or even trigger earthquake activities over both segments of fault. However, the following major aftershocks with a magnitude over 5.0 occurred on MFF-2, suggesting that the risk of seismic hazard on this fault has decreased, but MFF-1 might still be brought closer to failure owing to stress increase. Stress decrease dominated on ZFF, indicating that most recent major events with over M_w 5.0 on this fault are not related to aftershocks following

the 2017 Kermanshah Earthquake. Comparison between DInSAR measurements and high spatial resolution optical images from SuperView-1, suggest that most linear surface ruptures are likely landslides, ground cracks or rockfalls that occurred around the epicentre area.

Chapter 7 Conclusions and Future Work

The main objective of this dissertation was defined in Chapter 1 as: to investigate the source models and slip distributions of major earthquakes using geodetic modelling with the co-seismic DInSAR and GPS measurements, and to assess the risk of potential seismic hazards based on the Coulomb stress change analysis. In order to achieve this objective, three most recent earthquakes have been studied using InSAR and GPS data to understand stress interaction between faults. A concise overview of the seismic cycle and the Coulomb stress change was presented in Chapter 1, followed by the key contributions in this dissertation. The basic principle of SAR and InSAR, and the detailed DInSAR processing flow were reviewed and summarised in Chapter 2. The limitations of DInSAR technique was also briefly presented at the end of Chapter 2. The detailed basic expressions of geodetic modelling and Coulomb stress change were reviewed in Chapter 3. Three case studies of major earthquakes were presented in the following Chapters 4-6. The first case study is the 25 April 2015 M_w 7.8 Nepal Earthquake and its significant aftershock (M_w 7.2) in Chapter 4. The main shock (M_w 7.8) on 25 April 2015 was investigated by using co-seismic DInSAR and GPS measurements, while the source model of the major aftershock (M_w 7.2) on 12 May 2015 was determined using only DInSAR data. After determining the source models and slip distributions for the main shock and its major aftershocks, the triggering relationship was further explored through the Coulomb stress transfer between faults. The second case study is the 2016 Amatrice (Central Italy) Earthquake which was explored with ALOS-2 StripMap and Sentinel-1A/B SAR images as well as co-seismic GPS measurements (Chapter 5). The stress change on the source fault of this event and the fault plane of the following two major shocks are estimated to evaluate the triggering relationship between these events. Another most recent larger earthquake, the 12 November 2017 M_w 7.3 Kermanshah (Iran-Iraq border) Earthquake, was investigated using ALOS-2 ScanSAR and Sentinel-1A/B TOPSAR DInSAR measurements in Chapter 6. High spatial resolution optical images from SuperView-1 satellite and DInSAR measurements were used to explore the linear surface features over the epicentre area. The triggering relationship between major shock and aftershocks was discussed, followed the risk of seismic hazards on the neighbouring active faults assessed through the Coulomb stress change analysis.

In the following sections, I will summarise the main results and contributions of the three case studies of most recent earthquakes. And the recommendations for future work are presented at the end of this chapter.

7.1 Conclusions

In this dissertation, three most recent earthquakes have been studied by using geodetic measurements to understand their sources and influences to the regional faults. The main results and contributions of each case study are listed as follows:

1. The 25 April 2015 M_w 7.8 Nepal Earthquake and its significant aftershock (M_w 7.2). The source parameters and slip distributions of both events were inverted from geodetic data. The best-fit source models revealed that the fault geometries of main shock and this major aftershock are similar, showing two thrust faults both striking NW-SE with a small NE dip. Both events reach the peak slip at a similar depth of about 10.0km, with 5.12m for the main shock and 4.87m for the aftershock. The result of Coulomb stress change analysis showed that the source fault of main shock brought the fault of the M_w 7.2 event 0.5-1.46MPa closer to failure, evidencing the triggering relationship between the main shock and this aftershock. Our results also support the static stress change analysis from Feng's study which only used ALSO-2 ScanSAR images and GPS data (Feng et al., 2015).
2. The 24 August 2016 Amatrice (Central Italy) Earthquake. The co-seismic LOS deformation mapped by ALOS-2 StripMap and Sentinel-1A/B SAR image pairs is characteristic with two deformation lobes along NNW-SSE direction. A normal single fault with a small left-lateral component, striking $\sim 163^\circ$ NNW-SSE and dipping $\sim 46^\circ$ SW was inverted for this event. The distributed slip model clearly shows two separate slip asperities on the north and south of the fault plane. The calculation of the Coulomb stress change on the fault planes of the following two events (26 and 30 October 2016) revealed that the Amatrice Earthquake may probably promote or triggered these two events. Our results clarified the triggering relationship between these earthquakes based on the source model of our study and the fault models of the following two events retrieved from the Xu's study (Xu et al., 2017).
3. The 12 November 2017 M_w 7.3 Kermanshah (Iran-Iraq border) Earthquake. Five interferograms generated from ALOS-2 ScanSAR and Sentinel-1A/B TOPS SAR

data covering the epicentre area were used to explore the source model and co-seismic slip distribution. The optimised source model from the joint inversion shows a blind reverse fault with a relatively large right-lateral component, striking 353.5° NNW-SSE and dipping 16.3° NE. The maximum slip of $\sim 3.8\text{m}$ is located at depths of 12-14km. A combination of DInSAR wrapped interferograms and high spatial resolution optical images from SuperView-1 satellite to investigate the linear surface features revealed that most linear surface features probably could be secondary co-seismic hazards (e.g. landslides, surface cracks or rockfalls) rather than the possible fault ruptures on the surface. The calculation of Coulomb stress change on the source fault and the neighbouring active faults shows that: 1) the stress changes are in a good agreement with aftershock distribution; 2) Most importantly, we found that the high stress increase loaded into MFF-2 (one segment of the Zagros Mountain Front Fault) during the main shock could have been decreased by the following major aftershocks ($M_w \geq 5.0$) occurred in January and April 2018. However, the MFF-1 still might be brought closer to failure owing to stress increase, suggesting the risk of potential seismic hazards on this segment keeps increasing.

7.2 Recommendations for Future Work

For earthquake source modelling, more complete and accurate information of surface deformation is expected, which means more constraints in the inversion. SAR pixel offset tracking (SPOT) (Michel et al., 1999) and Multiple Aperture InSAR (MAI) (Bechor and Zebker, 2006) were proposed to measure the deformation along the azimuth and range direction. A combination of SAR-based techniques (conventional InSAR, SAR pixel offset tracking and Multiple Aperture InSAR) and GPS measurement can be used to map the co-seismic deformation in multiple directions. Multiple input dataset with various characteristics can provide more constrains for earthquake source modelling. In addition, SPOT and MAI can be applied to detect the large secondary co-seismic hazards caused by the shaking of main shock over the epicentre area.

Since the aftershock sequence generally lasts for a long period after the main shock, using the time-series InSAR technique to explore the post-seismic displacements allow us to understand the afterslip distribution (Wang et al., 2012, Diao et al., 2013). Most importantly, based on the temporal and spatial evolution of afterslip on the faults, further

assessment on seismic hazards through the Coulomb stress change can be conducted over the rupture area.

An earthquake occurs suddenly and causes destructive damage over a large area. The rapid hazard assessment plays an essential role in emergency response for rescue actions. One solution is to build up a semi-automatic or fully automatic system from SAR data processing to geodetic modelling with all available geodetic measurements for realising near real-time disaster response. After reading the SAR images and other available datasets (e.g. GPS and seismic data), a preliminary report about the surface deformation, earthquake source model and overall hazard assessment can be obtained from this system. Several factors need to be considered for this system: the ability to digest multiple datasets, the robust and highly efficient processing package and easy-to-understand output of the assessment report. This system can provide the important information for the rapid natural hazard response.

Reference

- ADHIKARI, L., GAUTAM, U., KOIRALA, B., BHATTARAI, M., KANDEL, T., GUPTA, R., TIMSINA, C., MAHARJAN, N., MAHARJAN, K. & DAHAL, T. 2015. The aftershock sequence of the 2015 April 25 Gorkha–Nepal earthquake. *Geophysical Supplements to the Monthly Notices of the Royal Astronomical Society*, 203 (3), 2119-2124.
- AKI, K. & RICHARDS, P. G. 1980. *Quantative seismology: Theory and methods*, New York, 801.
- ALBANO, M., BARBA, S., SAROLI, M., MORO, M., MALVAROSA, F., COSTANTINI, M., BIGNAMI, C. & STRAMONDO, S. 2015. Gravity-driven postseismic deformation following the Mw 6.3 2009 L'Aquila (Italy) earthquake. *Scientific reports*, 5, 16558.
- AMBRASEYS, N., MOINFAR, A. & PERONACI, P. 1973. the Seismicity of Iran the Farsinaj (Kermanshah) earthquake of 13 Decemher 1957. *Annals of Geophysics*, 26 (4), 679-692.
- ARNADÓTTIR, T. & SEGALL, P. 1994. The 1989 Loma Prieta earthquake imaged from inversion of geodetic data. *Journal of Geophysical Research: Solid Earth*, 99 (B11), 21835-21855.
- ASANO, K. & IWATA, T. 2016. Source rupture processes of the foreshock and mainshock in the 2016 Kumamoto earthquake sequence estimated from the kinematic waveform inversion of strong motion data. *Earth, Planets and Space*, 68 (1), 147.
- ASTER, R. C., BORCHERS, B. & THURBER, C. H. 2011. *Parameter estimation and inverse problems*, Academic Press, 90.
- ATZORI, S. & ANTONIOLI, A. 2011. Optimal fault resolution in geodetic inversion of coseismic data. *Geophysical Journal International*, 185 (1), 529-538.
- ATZORI, S., HUNSTAD, I., CHINI, M., SALVI, S., TOLOMEI, C., BIGNAMI, C., STRAMONDO, S., TRASATTI, E., ANTONIOLI, A. & BOSCHI, E. 2009. Finite fault inversion of DInSAR coseismic displacement of the 2009 L'Aquila earthquake (central Italy). *Geophysical Research Letters*, 36 (15), L15305.
- ATZORI, S. & SALVI, S. 2014. SAR data analysis in Solid Earth Geophysics: from science to risk management. *Land Applications of Radar Remote Sensing*. InTech, pp. 2–43.
- ATZORI, S., TOLOMEI, C., ANTONIOLI, A., MERRYMAN BONCORI, J., BANNISTER, S., TRASATTI, E., PASQUALI, P. & SALVI, S. 2012. The 2010–2011 Canterbury, New Zealand, seismic sequence: multiple source analysis from InSAR data and modeling. *Journal of Geophysical Research: Solid Earth*, 117 (B8), B08305.
- BAMLER, R. & HARTL, P. 1998. Synthetic aperture radar interferometry. *Inverse problems*, 14 (4), R1-R54.
- BARBOT, S., FIALKO, Y. & BOCK, Y. 2009. Postseismic deformation due to the Mw 6.0 2004 Parkfield earthquake: Stress - driven creep on a fault with spatially variable rate - and - state friction parameters. *Journal of Geophysical Research: Solid Earth*, 114 (B7), B07405.
- BEAVAN, J., MOTAGH, M., FIELDING, E. J., DONNELLY, N. & COLLETT, D. 2012. Fault slip models of the 2010–2011 Canterbury, New Zealand, earthquakes from geodetic data and observations of postseismic ground deformation. *New Zealand Journal of Geology and Geophysics*, 55 (3), 207-221.

- BECHOR, N. B. & ZEBKER, H. A. 2006. Measuring two - dimensional movements using a single InSAR pair. *Geophysical research letters*, 33 (16), L16311.
- BEELER, N., SIMPSON, R., HICKMAN, S. & LOCKNER, D. 2000. Pore fluid pressure, apparent friction, and Coulomb failure. *Journal of Geophysical Research: Solid Earth*, 105 (B11), 25533-25542.
- BERBERIAN, M., QORASHI, M., JACKSON, J., PRIESTLEY, K. & WALLACE, T. 1992. The Rudbar-Tarom earthquake of 20 June 1990 in NW Persia: preliminary field and seismological observations, and its tectonic significance. *Bulletin of the Seismological Society of America*, 82 (4), 1726-1755.
- BIGGS, J., WRIGHT, T., LU, Z. & PARSONS, B. 2007. Multi-interferogram method for measuring interseismic deformation: Denali Fault, Alaska. *Geophysical Journal International*, 170 (3), 1165-1179.
- BILHAM, R., LARSON, K. & FREYMUELLER, J. 1997. GPS measurements of present-day convergence across the Nepal Himalaya. *Nature*, 386 (6620), 61-64.
- BILHAM, R., OZENER, H., MENCIN, D., DOGRU, A., ERGINTAV, S., CAKIR, Z., AYTUN, A., AKTUG, B., YILMAZ, O. & JOHNSON, W. 2016. Surface creep on the North Anatolian fault at Ismetpasa, Turkey, 1944–2016. *Journal of Geophysical Research: Solid Earth*, 121 (10), 7409-7431.
- BILICH, A., CASSIDY, J. F. & LARSON, K. M. 2008. GPS seismology: Application to the 2002 M w 7.9 Denali fault earthquake. *Bulletin of the Seismological Society of America*, 98 (2), 593-606.
- CASAGLI, N., CIGNA, F., BIANCHINI, S., HÖLBLING, D., FÜREDER, P., RIGHINI, G., DEL CONTE, S., FRIEDL, B., SCHNEIDERBAUER, S. & IASIO, C. 2016. Landslide mapping and monitoring by using radar and optical remote sensing: examples from the EC-FP7 project SAFER. *Remote sensing applications: society and environment*, 4, 92-108.
- CAVALIÉ, O., LASSERRE, C., DOIN, M.-P., PELTZER, G., SUN, J., XU, X. & SHEN, Z.-K. 2008. Measurement of interseismic strain across the Haiyuan fault (Gansu, China), by InSAR. *Earth and Planetary Science Letters*, 275 (3-4), 246-257.
- CHELONI, D., DE NOVELLIS, V., ALBANO, M., ANTONIOLI, A., ANZIDEI, M., ATZORI, S., AVALLONE, A., BIGNAMI, C., BONANO, M. & CALCATERRA, S. 2017. Geodetic model of the 2016 Central Italy earthquake sequence inferred from InSAR and GPS data. *Geophysical Research Letters*, 44, 6778–6787.
- CHELONI, D., SERPELLONI, E., DEVOTI, R., D'AGOSTINO, N., PIETRANTONIO, G., RIGUZZI, F., ANZIDEI, M., AVALLONE, A., CAVALIERE, A. & CECERE, G. 2016. GPS observations of coseismic deformation following the 2016, August 24, Mw 6 Amatrice earthquake (central Italy): data, analysis and preliminary fault model. *Annals of Geophysics*, 59 (5), 1-8.
- CHEN, C. W. & ZEBKER, H. A. 2000. Network approaches to two-dimensional phase unwrapping: intractability and two new algorithms. *JOSA A*, 17 (3), 401-414.
- CHEN, K. H., NADEAU, R. M. & RAU, R.-J. 2008. Characteristic repeating earthquakes in an arc-continent collision boundary zone: The Chihshang fault of eastern Taiwan. *Earth and Planetary Science Letters*, 276 (3-4), 262-272.
- CHILÈS, J. & DELFINER, P. 1999. *Geostatistics-Modelling Spatial Uncertainty*. Wiley series in probability and mathematical statistics. Applied probability and statistics section: John Wiley & Sons, Inc., New York.
- COSTANTINI, M. 1998. A novel phase unwrapping method based on network programming. *IEEE Transactions on Geoscience and Remote Sensing*, 36 (3), 813-821.

- COSTANTINI, M. & ROSEN, P. A. A generalized phase unwrapping approach for sparse data. *Geoscience and Remote Sensing Symposium, 1999. IGARSS'99 Proceedings. IEEE 1999 International*, 1999. IEEE, 1, 267-269.
- DE ZAN, F. & GUARNIERI, A. M. 2006. TOPSAR: Terrain observation by progressive scans. *IEEE Transactions on Geoscience and Remote Sensing*, 44 (9), 2352-2360.
- DELOUIS, B., GIARDINI, D., LUNDGREN, P. & SALICHON, J. 2002. Joint inversion of InSAR, GPS, teleseismic, and strong-motion data for the spatial and temporal distribution of earthquake slip: Application to the 1999 Izmit mainshock. *Bulletin of the Seismological Society of America*, 92 (1), 278-299.
- DIAO, F., XIONG, X., WANG, R., ZHENG, Y., WALTER, T. R., WENG, H. & LI, J. 2013. Overlapping post-seismic deformation processes: Afterslip and viscoelastic relaxation following the 2011 M w 9.0 Tohoku (Japan) earthquake. *Geophysical Journal International*, 196 (1), 218-229.
- DZIEWONSKI, A., CHOU, T. A. & WOODHOUSE, J. 1981. Determination of earthquake source parameters from waveform data for studies of global and regional seismicity. *Journal of Geophysical Research: Solid Earth*, 86 (B4), 2825-2852.
- EKSTRÖM, G., NETTLES, M. & DZIEWOŃSKI, A. 2012. The global CMT project 2004–2010: Centroid-moment tensors for 13,017 earthquakes. *Physics of the Earth and Planetary Interiors*, 200, 1-9.
- ELLIOTT, J., NISSEN, E., ENGLAND, P., JACKSON, J. A., LAMB, S., LI, Z., OEHLERS, M. & PARSONS, B. 2012. Slip in the 2010–2011 canterbury earthquakes, New Zealand. *Journal of Geophysical Research: Solid Earth*, 117 (B3), B03401.
- EM-DAT (2018). *The international disaster database* [Online]. Available: <http://www.emdat.be/database> [Accessed 15 June 2018].
- EMERGEO WORKING GROUP 2016. The 24 August 2016 Amatrice Earthquake: Coseismic Effects. doi: <https://doi.org/10.5281/zenodo.61568>.
- FAN, W. & SHEARER, P. M. 2015. Detailed rupture imaging of the 25 April 2015 Nepal earthquake using teleseismic P waves. *Geophysical Research Letters*, 42 (14), 5744-5752.
- FARR, T. G., ROSEN, P. A., CARO, E., CRIPPEN, R., DUREN, R., HENSLEY, S., KOBRICK, M., PALLER, M., RODRIGUEZ, E. & ROTH, L. 2007. The shuttle radar topography mission. *Reviews of geophysics*, 45 (2), 37–55.
- FARZANEGAN, E., SHAHVAR, M. P., ESHAGHI, A., MIRSANJARI, M., ABDOLLAHI, H. & ALAVIJEH, H. M. 2017. REPORT OF THE NOVEMBER 12, 2017 SARPOL-E ZAHAB, KERMANSHAH PROVINCE EARTHQUAKE. URL: <http://ismn.bhrc.ac.ir/en/News/ID/8272/REPORT-OF-THE-NOVEMBER-12-2017-SARPOL-E-ZAHAB-KERMANSHAH-PROVINCE-EARTHQUAKE>.
- FENG, G., LI, Z., SHAN, X., ZHANG, L., ZHANG, G. & ZHU, J. 2015. Geodetic model of the 2015 April 25 Mw 7.8 Gorkha Nepal Earthquake and Mw 7.3 aftershock estimated from InSAR and GPS data. *Geophysical Journal International*, 203 (2), 896-900.
- FENG, W., LINDSEY, E., BARBOT, S., SAMSONOV, S., DAI, K., LI, P., LI, Z., ALMEIDA, R., CHEN, J. & XU, X. 2017. Source characteristics of the 2015 MW 7.8 Gorkha (Nepal) earthquake and its MW 7.2 aftershock from space geodesy. *Tectonophysics*, 712, 747-758.

- FERRETI, A., MONTI GUANRIERI, C., PRATI, C., ROCCA, F. & MASSONNET, D. 2007. *InSAR Principles–Guidelines for SAR Interferometry Processing and Interpretation*, ESA Publications, TM-19, 246.
- FIALKO, Y. 2004. Evidence of fluid - filled upper crust from observations of postseismic deformation due to the 1992 Mw7. 3 Landers earthquake. *Journal of Geophysical Research: Solid Earth*, 109 (B8), B08401.
- FIALKO, Y. 2006. Interseismic strain accumulation and the earthquake potential on the southern San Andreas fault system. *Nature*, 441 (7096), 968-971.
- FIALKO, Y., SIMONS, M. & AGNEW, D. 2001. The complete (3 - D) surface displacement field in the epicentral area of the 1999 Mw7. 1 Hector Mine earthquake, California, from space geodetic observations. *Geophysical Research Letters*, 28 (16), 3063-3066.
- FIELDING, E. J., TALEBIAN, M., ROSEN, P. A., NAZARI, H., JACKSON, J. A., GHORASHI, M. & WALKER, R. 2005. Surface ruptures and building damage of the 2003 Bam, Iran, earthquake mapped by satellite synthetic aperture radar interferometric correlation. *Journal of Geophysical Research: Solid Earth*, 110 (B3), B03302.
- FLYNN, T. J. 1997. Two-dimensional phase unwrapping with minimum weighted discontinuity. *JOSA A*, 14 (10), 2692-2701.
- FUNNING, G. J., PARSONS, B., WRIGHT, T. J., JACKSON, J. A. & FIELDING, E. J. 2005. Surface displacements and source parameters of the 2003 Bam (Iran) earthquake from Envisat advanced synthetic aperture radar imagery. *Journal of Geophysical Research: Solid Earth*, 110 (B9), B09406.
- GARTHWAITE, M. C., WANG, H. & WRIGHT, T. J. 2013. Broadscale interseismic deformation and fault slip rates in the central Tibetan Plateau observed using InSAR. *Journal of Geophysical Research: Solid Earth*, 118 (9), 5071-5083.
- GATELLI, F., GUAMIERI, A. M., PARIZZI, F., PASQUALI, P., PRATI, C. & ROCCA, F. 1994. The wavenumber shift in SAR interferometry. *IEEE Transactions on Geoscience and Remote Sensing*, 32 (4), 855-865.
- GE, L., ZHANG, K., NG, A., DONG, Y., CHANG, H.-C. & RIZOS, C. 2008. Preliminary results of satellite radar differential interferometry for the co-seismic deformation of the 12 May 2008 Ms8. 0 Wenchuan earthquake. *Geographic Information Sciences*, 14 (1), 12-19.
- GHIGLIA, D. C. & PRITT, M. D. 1998. *Two-dimensional phase unwrapping: theory, algorithms, and software*, Wiley New York, 4, 512.
- GHIGLIA, D. C. & ROMERO, L. A. 1996. Minimum Lp-norm two-dimensional phase unwrapping. *JOSA A*, 13 (10), 1999-2013.
- GOLDSTEIN, R. 1995. Atmospheric limitations to repeat - track radar interferometry. *Geophysical research letters*, 22 (18), 2517-2520.
- GOLDSTEIN, R. M. & WERNER, C. L. 1998. Radar interferogram filtering for geophysical applications. *Geophysical Research Letters*, 25 (21), 4035-4038.
- GOLDSTEIN, R. M., ZEBKER, H. A. & WERNER, C. L. 1988. Satellite radar interferometry: Two-dimensional phase unwrapping. *Radio science*, 23 (4), 713-720.
- GONZÁLEZ, P. J., BAGNARDI, M., HOOPER, A. J., LARSEN, Y., MARINKOVIC, P., SAMSONOV, S. V. & WRIGHT, T. J. 2015. The 2014–2015 eruption of Fogo volcano: Geodetic modeling of Sentinel - 1 TOPS interferometry. *Geophysical research letters*, 42 (21), 9239-9246.

- GORUM, T., FAN, X., VAN WESTEN, C. J., HUANG, R. Q., XU, Q., TANG, C. & WANG, G. 2011. Distribution pattern of earthquake-induced landslides triggered by the 12 May 2008 Wenchuan earthquake. *Geomorphology*, 133 (3-4), 152-167.
- GUARNIERI, A. M. & PRATI, C. 1996. ScanSAR focusing and interferometry. *IEEE Transactions on Geoscience and Remote Sensing*, 34 (4), 1029-1038.
- HAINZL, S., STEACY, S. & MARSAN, D. 2010. Seismicity models based on Coulomb stress calculations. *Community online resource for statistical seismicity analysis*, <http://dx.doi.org/10.5078/corssa-32035809>.
- HANSEN, R. F. 2001. *Radar interferometry: data interpretation and error analysis*, Springer Science & Business Media, 2, 308.
- HARRIS, R. A. 1998. Introduction to special section: Stress triggers, stress shadows, and implications for seismic hazard. *Journal of Geophysical Research: Solid Earth*, 103 (B10), 24347-24358.
- HARRIS, R. A. 2017. Large earthquakes and creeping faults. *Reviews of Geophysics*, 55 (1), 169-198.
- HARRIS, R. A. & SEGALL, P. 1987. Detection of a locked zone at depth on the Parkfield, California, segment of the San Andreas fault. *Journal of Geophysical Research: Solid Earth*, 92 (B8), 7945-7962.
- HESSAMI, K., JAMALI, F. & TABASSI, H. 2003. Major active faults of Iran. *International Institute of Earthquake Engineering and Seismology, Tehran, Iran*.
- HUANG, M. H., FIELDING, E. J., LIANG, C., MILILLO, P., BEKAERT, D., DREGER, D. & SALZER, J. 2017a. Coseismic deformation and triggered landslides of the 2016 Mw 6.2 Amatrice earthquake in Italy. *Geophysical Research Letters*, 44, 1266–1274.
- HUANG, Y., YANG, S., QIAO, X., LIN, M., ZHAO, B. & TAN, K. 2017b. Measuring ground deformations caused by 2015 Mw7. 8 Nepal earthquake using high-rate GPS data. *Geodesy and Geodynamics*, 8 (4), 285-291.
- HUDNUT, K., SHEN, Z., MURRAY, M., MCCLUSKY, S., KING, R., HERRING, T., HAGER, B., FENG, Y., FANG, P. & DONNELLAN, A. 1996. Co-seismic displacements of the 1994 Northridge, California, earthquake. *Bulletin of the Seismological Society of America*, 86 (1B), S19-S36.
- IINUMA, T., OHZONO, M., OHTA, Y. & MIURA, S. 2011. Coseismic slip distribution of the 2011 off the Pacific coast of Tohoku Earthquake (M 9.0) estimated based on GPS data—Was the asperity in Miyagi-oki ruptured? *Earth, planets and space*, 63 (7), 643–648.
- INGV WORKING GROUP "GPS GEODESY (GPS DATA AND DATA ANALYSIS CENTER)" 2016. Preliminary co-seismic displacements for the August 24, 2016 ML6, Amatrice (central Italy) earthquake from the analysis of continuous GPS stations. <http://doi.org/10.5281/zenodo.61355>.
- JOLIVET, R., LASSERRE, C., DOIN, M. P., GUILLASO, S., PELTZER, G., DAILU, R., SUN, J., SHEN, Z. K. & XU, X. 2012. Shallow creep on the Haiyuan fault (Gansu, China) revealed by SAR interferometry. *Journal of Geophysical Research: Solid Earth*, 117 (B6), B06401.
- JOLIVET, R., SIMONS, M., AGRAM, P., DUPUTEL, Z. & SHEN, Z. K. 2015. Aseismic slip and seismogenic coupling along the central San Andreas Fault. *Geophysical Research Letters*, 42 (2), 297-306.
- JONSSON, S. 2002. *Modeling volcano and earthquake deformation from satellite radar interferometric observations*. Phd thesis, Stanford University.
- JÓNSSON, S., ZEBKER, H., SEGALL, P. & AMELUNG, F. 2002. Fault slip distribution of the 1999 Mw 7.1 Hector Mine, California, earthquake, estimated from satellite

- radar and GPS measurements. *Bulletin of the Seismological Society of America*, 92 (4), 1377-1389.
- KANEKO, Y., FIALKO, Y., SANDWELL, D., TONG, X. & FURUYA, M. 2013. Interseismic deformation and creep along the central section of the North Anatolian fault (Turkey): InSAR observations and implications for rate - and - state friction properties. *Journal of Geophysical Research: Solid Earth*, 118 (1), 316-331.
- KING, G. C., STEIN, R. S. & LIN, J. 1994. Static stress changes and the triggering of earthquakes. *Bulletin of the Seismological Society of America*, 84 (3), 935-953.
- KOBAYASHI, T., MORISHITA, Y., YARAI, H. & FUJIWARA, S. 2017. InSAR-derived Crustal Deformation and Reverse Fault Motion of the 2017 Iran-Iraq Earthquake in the Northwestern Part of the Zagros Orogenic Belt. *Bull. Geospatial Info: Sunnyvale, CA, USA*.
- KREEMER, C., BLEWITT, G. & KLEIN, E. C. 2014. A geodetic plate motion and Global Strain Rate Model. *Geochemistry, Geophysics, Geosystems*, 15 (10), 3849-3889.
- LAVÉ, J. & AVOUAC, J.-P. 2000. Active folding of fluvial terraces across the Siwaliks Hills, Himalayas of central Nepal. *Journal of Geophysical Research: Solid Earth*, 105 (B3), 5735-5770.
- LAVECCHIA, G., CASTALDO, R., NARDIS, R., DE NOVELLIS, V., FERRARINI, F., PEPE, S., BROZZETTI, F., SOLARO, G., CIRILLO, D. & BONANO, M. 2016. Ground deformation and source geometry of the 24 August 2016 Amatrice earthquake (Central Italy) investigated through analytical and numerical modeling of DInSAR measurements and structural - geological data. *Geophysical Research Letters*, 43, 12,389 - 12,398.
- LI, Y.-J., CHEN, L.-W., LU, Y.-Z. & ZHAN, Z.-M. 2013. Numerical simulation on influences of Wenchuan earthquake on the stability of faults in the neighborhood. *Earth Science/Diqiu Kexue*, 38 (2), 398-410.
- LIU, C., ZHENG, Y., XIE, Z. & XIONG, X. 2017. Rupture features of the 2016 Mw 6.2 Norcia earthquake and its possible relationship with strong seismic hazards. *Geophysical Research Letters*, 44 (3), 1320-1328.
- LOHMAN, R. B. 2004. *The inversion of geodetic data for earthquake parameters*. Phd thesis, California Institute of Technology.
- MADANIPOUR, S., EHLERS, T. A., YASSAGHI, A., REZAEIAN, M., ENKELMANN, E. & BAHROUDI, A. 2013. Synchronous deformation on orogenic plateau margins: Insights from the Arabia-Eurasia collision. *Tectonophysics*, 608, 440-451.
- MARQUARDT, D. W. 1963. An algorithm for least-squares estimation of nonlinear parameters. *Journal of the society for Industrial and Applied Mathematics*, 11 (2), 431-441.
- MASSONNET, D., FEIGL, K., ROSSI, M. & ADRAGNA, F. 1994. Radar interferometric mapping of deformation in the year after the Landers earthquake. *Nature*, 369 (6477), 227-230.
- MASSONNET, D. & FEIGL, K. L. 1995a. Discrimination of geophysical phenomena in satellite radar interferograms. *Geophysical research letters*, 22 (12), 1537-1540.
- MASSONNET, D. & FEIGL, K. L. 1995b. Satellite radar interferometric map of the coseismic deformation field of the M= 6.1 Eureka Valley, California earthquake of May 17, 1993. *Geophysical Research Letters*, 22 (12), 1541-1544.
- MASSONNET, D. & FEIGL, K. L. 1998. Radar interferometry and its application to changes in the Earth's surface. *Reviews of geophysics*, 36 (4), 441-500.

- MASSONNET, D., FEIGL, K. L., VADON, H. & ROSSI, M. 1996. Coseismic deformation field of the M= 6.7 Northridge, California earthquake of January 17, 1994 recorded by two radar satellites using interferometry. *Geophysical Research Letters*, 23 (9), 969-972.
- MASSONNET, D., ROSSI, M., CARMONA, C., ADRAGNA, F., PELTZER, G., FEIGL, K. & RABAUTE, T. 1993. The displacement field of the Landers earthquake mapped by radar interferometry. *Nature*, 364 (6433), 138-142.
- MCCLOSKEY, J., NALBANT, S. S. & STEACY, S. 2005. Indonesian earthquake: Earthquake risk from co-seismic stress. *Nature*, 434 (7031), 291.
- MCQUARRIE, N. 2004. Crustal scale geometry of the Zagros fold–thrust belt, Iran. *Journal of Structural Geology*, 26 (3), 519-535.
- MENKE, W. 2018. *Geophysical data analysis: Discrete inverse theory*, Academic press.
- MICHEL, R., AVOUAC, J. P. & TABOURY, J. 1999. Measuring near field coseismic displacements from SAR images: Application to the Landers earthquake. *Geophysical Research Letters*, 26 (19), 3017-3020.
- MOUGINOT, J., SCHEUCHL, B. & RIGNOT, E. 2012. Mapping of ice motion in Antarctica using synthetic-aperture radar data. *Remote Sensing*, 4 (9), 2753-2767.
- MOUTHEREAU, F., LACOMBE, O. & VERGÉS, J. 2012. Building the Zagros collisional orogen: timing, strain distribution and the dynamics of Arabia/Eurasia plate convergence. *Tectonophysics*, 532, 27-60.
- MURRAY, M. H., MARSHALL, G. A., LISOWSKI, M. & STEIN, R. S. 1996. The 1992 M= 7 Cape Mendocino, California, earthquake: Coseismic deformation at the south end of the Cascadia megathrust. *Journal of Geophysical Research: Solid Earth*, 101 (B8), 17707-17725.
- NG, A. H.-M., GE, L., ZHANG, K., CHANG, H.-C., LI, X., RIZOS, C. & OMURA, M. 2011. Deformation mapping in three dimensions for underground mining using InSAR–Southern highland coalfield in New South Wales, Australia. *International Journal of Remote Sensing*, 32 (22), 7227-7256.
- NG, A. H.-M., GE, L., ZHANG, K. & LI, X. 2012. Estimating horizontal and vertical movements due to underground mining using ALOS PALSAR. *Engineering Geology*, 143, 18-27.
- OKADA, Y. 1985. Surface deformation due to shear and tensile faults in a half-space. *Bulletin of the seismological society of America*, 75 (4), 1135-1154.
- OKADA, Y. 1992. Internal deformation due to shear and tensile faults in a half-space. *Bulletin of the Seismological Society of America*, 82 (2), 1018-1040.
- PATRI, C. & ROCCA, F. Range resolution enhancement with multiple SAR surveys combination. Geoscience and Remote Sensing Symposium, 1992. IGARSS'92. International, 1992. IEEE, 2, 1576-1578.
- PICCARDI, L., BLUMETTI, A., FERRARIO, F., BONADEO, L., BRUNAMONTE, F., SANI, F., TONDI, E., WEDMORE, L. & GREGORY, L. 2016. The August 24, 2016, Amatrice earthquake (Mw 6.0): Field evidence of on-fault effects- Preliminary report. http://www.isprambiente.gov.it/files/notizie-ispra/notizie-2016/sisma-italia-centrale/REPORT_Amatrice_en_2016_09_16.compressed.pdf.
- PIZZI, A. & GALADINI, F. 2009. Pre-existing cross-structures and active fault segmentation in the northern-central Apennines (Italy). *Tectonophysics*, 476 (1), 304-319.
- POLLITZ, F. F., BANERJEE, P., BÜRGMANN, R., HASHIMOTO, M. & CHOOSAKUL, N. 2006. Stress changes along the Sunda trench following the 26 December 2004 Sumatra - Andaman and 28 March 2005 Nias earthquakes. *Geophysical research letters*, 33 (6), L06309.

- PRITCHARD, M., SIMONS, M., ROSEN, P., HENSLEY, S. & WEBB, F. 2002. Co-seismic slip from the 1995 July 30 M_w= 8.1 Antofagasta, Chile, earthquake as constrained by InSAR and GPS observations. *Geophysical Journal International*, 150 (2), 362-376.
- PRITT, M. D. 1996. Phase unwrapping by means of multigrid techniques for interferometric SAR. *IEEE Transactions on Geoscience and Remote Sensing*, 34 (3), 728-738.
- REILINGER, R., MCCLUSKY, S., ORAL, M., KING, R., TOKSOZ, M., BARKA, A., KINIK, I., LENK, O. & SANLI, I. 1997. Global Positioning System measurements of present - day crustal movements in the Arabia - Africa - Eurasia plate collision zone. *Journal of Geophysical Research: Solid Earth*, 102 (B5), 9983-9999.
- RIGNOT, E. & MOUGINOT, J. 2012. Ice flow in Greenland for the international polar year 2008–2009. *Geophysical Research Letters*, 39 (11), L11501.
- ROCCA, F., PRATI, C., PASQUALI, P. & GUARNIERI, A. M. 1994. ERS-1 SAR Interferometry techniques and applications. *ESA, Noordwijk, The Netherlands, Contract Rep.*, (3-7439), 92.
- RODRIGUEZ, E. & MARTIN, J. Theory and design of interferometric synthetic aperture radars. *IEE Proceedings F (Radar and Signal Processing)*, 1992. IET, 139 (2), 147-159.
- ROSEN, P. A., HENSLEY, S., JOUGHIN, I. R., LI, F. K., MADSEN, S. N., RODRIGUEZ, E. & GOLDSTEIN, R. M. 2000. Synthetic aperture radar interferometry. *Proceedings of the IEEE*, 88 (3), 333-382.
- RUIZ, S., METOIS, M., FUENZALIDA, A., RUIZ, J., LEYTON, F., GRANDIN, R., VIGNY, C., MADARIAGA, R. & CAMPOS, J. 2014. Intense foreshocks and a slow slip event preceded the 2014 Iquique Mw 8.1 earthquake. *Science*, 345 (6201), 1165-1169.
- RYDER, I., PARSONS, B., WRIGHT, T. J. & FUNNING, G. J. 2007. Post-seismic motion following the 1997 Manyi (Tibet) earthquake: InSAR observations and modelling. *Geophysical Journal International*, 169 (3), 1009-1027.
- SEGALL, P. & DAVIS, J. L. 1997. GPS applications for geodynamics and earthquake studies. *Annual Review of Earth and Planetary Sciences*, 25 (1), 301-336.
- SHAHRYAR SOLAYMANI AZAD, N. S., M. MORADI, A. AJHDARI, T. YOUSSEFI, M. MASHAL, M. ROUSTAIE 2017. Preliminary report on geological features of the Ezgaleh-Kermanshah earthquake. <http://gsi.ir/en/ReportsData/MoreInfo/All/0/1918/Preliminary.report.on.geological.features.of.the.Ezgaleh.Kermanshah.earthquake.html>.
- SHAN, B., ZHENG, Y., LIU, C., XIE, Z. & KONG, J. 2017. Coseismic Coulomb failure stress changes caused by the 2017 M7. 0 Jiuzhaigou earthquake, and its relationship with the 2008 Wenchuan earthquake. *Science China Earth Sciences*, 60 (12), 2181-2189.
- SHEARER, P. M. 2009. *Introduction to seismology*, Cambridge University Press.
- SHEN, Z.-K., JACKSON, D. D., FENG, Y., CLINE, M., KIM, M., FANG, P. & BOCK, Y. 1994. Postseismic deformation following the Landers earthquake, California, 28 June 1992. *Bulletin of the Seismological Society of America*, 84 (3), 780-791.
- SHEN, Z.-K., SUN, J., ZHANG, P., WAN, Y., WANG, M., BÜRGMANN, R., ZENG, Y., GAN, W., LIAO, H. & WANG, Q. 2009. Slip maxima at fault junctions and rupturing of barriers during the 2008 Wenchuan earthquake. *Nature Geoscience*, 2 (10), 718-724.

- SHI, C., LOU, Y.-D., ZHANG, H.-P., ZHAO, Q., GENG, J., WANG, R., FANG, R. & LIU, J. 2010. Seismic deformation of the Mw 8.0 Wenchuan earthquake from high-rate GPS observations. *Advances in Space Research*, 46 (2), 228-235.
- SIMONS, M., FIALKO, Y. & RIVERA, L. 2002. Coseismic deformation from the 1999 Mw 7.1 Hector Mine, California, earthquake as inferred from InSAR and GPS observations. *Bulletin of the Seismological Society of America*, 92 (4), 1390-1402.
- SKEMPTON, A. 1954. The Pore Pressure Coefficients A and B. *Geotechniques* 4 (4): 143-147.
- STEIN, R. S. 1999. The role of stress transfer in earthquake occurrence. *Nature*, 402 (6762), 605-609.
- STEIN, R. S., BARKA, A. A. & DIETERICH, J. H. 1997. Progressive failure on the North Anatolian fault since 1939 by earthquake stress triggering. *Geophysical Journal International*, 128 (3), 594-604.
- STEKETEE, J. 1958. On Volterra's dislocations in a semi-infinite elastic medium. *Canadian Journal of Physics*, 36 (2), 192-205.
- STEVENS, V. & AVOUAC, J. 2015. Interseismic coupling on the main Himalayan thrust. *Geophysical Research Letters*, 42 (14), 5828-5837.
- STYRON, R., TAYLOR, M. & OKORONKWO, K. 2010. Database of active structures from the Indo - Asian collision. *Eos, Transactions American Geophysical Union*, 91 (20), 181-182.
- SUÁREZ, G., ESPINOSA - ARANDA, J., CUÉLLAR, A., IBARROLA, G., GARCÍA, A., ZAVALA, M., MALDONADO, S. & ISLAS, R. 2018. A dedicated seismic early warning network: The Mexican Seismic Alert System (SASMEX). *Seismological Research Letters*, 89 (2A), 382-391.
- SUDHAUS, H. 2010. *Improving earthquake source studies using InSAR*. Diss., Eidgenössische Technische Hochschule ETH Zürich, Nr. 18966, 2010.
- SUDHAUS, H. & SIGURJÓN, J. 2009. Improved source modelling through combined use of InSAR and GPS under consideration of correlated data errors: application to the June 2000 Kleifarvatn earthquake, Iceland. *Geophysical Journal International*, 176 (2), 389-404.
- SZELIGA, W., HOUGH, S., MARTIN, S. & BILHAM, R. 2010. Intensity, magnitude, location, and attenuation in India for felt earthquakes since 1762. *Bulletin of the Seismological Society of America*, 100 (2), 570-584.
- TARANTOLA, A. 2005. *Inverse problem theory and methods for model parameter estimation*, SIAM, 89.
- THOMAS, M. Y., AVOUAC, J. P., CHAMPENOIS, J., LEE, J. C. & KUO, L. C. 2014. Spatiotemporal evolution of seismic and aseismic slip on the Longitudinal Valley Fault, Taiwan. *Journal of Geophysical Research: Solid Earth*, 119 (6), 5114-5139.
- TINTI, E., SCOGNAMIGLIO, L., MICHELINI, A. & COCCO, M. 2016. Slip heterogeneity and directivity of the ML 6.0, 2016, Amatrice earthquake estimated with rapid finite - fault inversion. *Geophysical Research Letters*, 43 (20), 10,745-10,752.
- TONG, X., SANDWELL, D. & SMITH - KONTER, B. 2013. High - resolution interseismic velocity data along the San Andreas fault from GPS and InSAR. *Journal of Geophysical Research: Solid Earth*, 118 (1), 369-389.
- TONG, X., SANDWELL, D. T. & FIALKO, Y. 2010. Coseismic slip model of the 2008 Wenchuan earthquake derived from joint inversion of interferometric synthetic aperture radar, GPS, and field data. *Journal of Geophysical Research: Solid Earth*, 115 (B4), B04314.

- TORRES, R., SNOEIJ, P., GEUDTNER, D., BIBBY, D., DAVIDSON, M., ATTEMA, E., POTIN, P., ROMMEN, B., FLOURY, N. & BROWN, M. 2012. GMES Sentinel-1 mission. *Remote Sensing of Environment*, 120, 9-24.
- VERGÉS, J., SAURA, E., CASCIELLO, E., FERNÁNDEZ, M., VILLASEÑOR, A., JIMÉNEZ-MUNT, I. & GARCÍA-CASTELLANOS, D. 2011. Crustal-scale cross-sections across the NW Zagros belt: implications for the Arabian margin reconstruction. *Geological Magazine*, 148 (5-6), 739-761.
- WANG, H., WRIGHT, T. & BIGGS, J. 2009. Interseismic slip rate of the northwestern Xianshuihe fault from InSAR data. *Geophysical Research Letters*, 36 (3), L03302.
- WANG, H., XU, C. & GE, L. 2007. Coseismic deformation and slip distribution of the 1997 Mw7. 5 Manyi, Tibet, earthquake from InSAR measurements. *Journal of Geodynamics*, 44 (3), 200-212.
- WANG, K. & FIALKO, Y. 2015. Slip model of the 2015 Mw 7.8 Gorkha (Nepal) earthquake from inversions of ALOS - 2 and GPS data. *Geophysical Research Letters*, 42 (18), 7452-7458.
- WANG, K., HU, Y. & HE, J. 2012. Deformation cycles of subduction earthquakes in a viscoelastic Earth. *Nature*, 484 (7394), 327-332.
- WEBSTER, R. & OLIVER, M. A. 2007. *Geostatistics for environmental scientists*, John Wiley & Sons.
- WEI, S., CHEN, M., WANG, X., GRAVES, R., LINDSEY, E., WANG, T., KARAKAŞ, Ç. & HELMBERGER, D. 2018. The 2015 Gorkha (Nepal) earthquake sequence: I. Source modeling and deterministic 3D ground shaking. *Tectonophysics*, 722, 447-461.
- WRIGHT, T., PARSONS, B., JACKSON, J., HAYNES, M., FIELDING, E., ENGLAND, P. & CLARKE, P. 1999. Source parameters of the 1 October 1995 Dinar (Turkey) earthquake from SAR interferometry and seismic bodywave modelling. *Earth and Planetary Science Letters*, 172 (1-2), 23-37.
- WRIGHT, T. J., LU, Z. & WICKS, C. 2003. Source model for the Mw 6.7, 23 October 2002, Nenana Mountain Earthquake (Alaska) from InSAR. *Geophysical Research Letters*, 30 (18), 1974.
- WRIGHT, T. J., LU, Z. & WICKS, C. 2004a. Constraining the slip distribution and fault geometry of the Mw 7.9, 3 November 2002, Denali fault earthquake with interferometric synthetic aperture radar and global positioning system data. *Bulletin of the Seismological Society of America*, 94 (6B), S175-S189.
- WRIGHT, T. J., PARSONS, B. E. & LU, Z. 2004b. Toward mapping surface deformation in three dimensions using InSAR. *Geophysical Research Letters*, 31 (1), 1-5.
- XU, G., XU, C., WEN, Y. & JIANG, G. 2017. Source Parameters of the 2016–2017 Central Italy Earthquake Sequence from the Sentinel-1, ALOS-2 and GPS Data. *Remote Sensing*, 9 (11), 1182.
- ZARE, M., KAMRANZAD, F., PARCHARIDIS, I. & TSIRONI, V. 2017. Preliminary report of Mw7.3 Sarpol-e Zahab, Iran earthquake on November 12, 2017. https://www.emsc-csem.org/Files/news/Earthquakes_reports/Preliminary_report_M7.3_20171112_v3.pdf.
- ZEBKER, H. A., ROSEN, P. A., GOLDSTEIN, R. M., GABRIEL, A. & WERNER, C. L. 1994. On the derivation of coseismic displacement fields using differential radar interferometry: The Landers earthquake. *Journal of Geophysical Research: Solid Earth*, 99 (B10), 19617-19634.
- ZEBKER, H. A. & VILLASENOR, J. 1992. Decorrelation in interferometric radar echoes. *IEEE Transactions on Geoscience and Remote Sensing*, 30 (5), 950-959.

- ZHAO, D., QU, C., SHAN, X., GONG, W., ZHANG, Y. & ZHANG, G. 2018. InSAR and GPS derived coseismic deformation and fault model of the 2017 Ms7.0 Jiuzhaigou earthquake in the Northeast Bayanhar block. *Tectonophysics*, 726, 86-99.
- ZIV, A. & RUBIN, A. M. 2000. Static stress transfer and earthquake triggering: No lower threshold in sight? *Journal of Geophysical Research: Solid Earth*, 105 (B6), 13631-13642.